A study of particle generation during laser ablation with applications

by

Chunyi Liu

B.S. National Taiwan University 1996
M.S. National Taiwan University 1998

A dissertation (or thesis) submitted in partial satisfaction of the

requirements for the degree of

Doctor of Philosophy
in
Engineering-Mechanical Enginnering

in the

GRADUATE DIVISION

of the

UNIVERSITY OF CALIFORNIA, BERKELEY

Committee in charge:

Professor Ralph Greif, Chair
Professor Costas P. Grigoropoulos
Professor Per F. Peterson

Fall 2005

Abstract

A Study of Particle Generation during Laser Ablation with Applications

by

Chunyi Liu

Doctor of Philosophy in Engineering

University of California at Berkeley

Professor Ralph Greif, Chair

A study has been made of the generation of particles during laser ablation and has included size distribution measurements and observation of the formation processes. The particle size distribution with respect to different laser parameters was obtained in-line using a differential mobility analyzer (DMA) and a particle counter. The experimental results show that the particle size varies with laser energy, laser pulsewidth, ambient gas flowrate and sample properties. The results serve as a basis for controlling the size of nanoparticles generated by laser ablation.

Laser shadowgraph imaging was used to study mass ejection processes and mechanisms. At higher laser irradiance, some particles were ejected in the liquid and even in the solid phase. Time-resolved images show the propagation of the shockwaves: external shockwaves propagate outward and decelerate, and internal shockwaves reflect back and forth between the gas contact surface and the sample surface. The internal shockwave is proposed to cause the ejection of liquid particles when the internal shockwave strikes the liquid molten layer. A simulation based on

vapor plume expansion was carried out and provides satisfactory agreement with experimental results. Different material properties result in different particle ejection behavior: particle ejection for most materials including metals result in a conically shaped envelope for the ejected material while ejection for silicon resembles a liquid jet. The difference in density change when the materials melt was proposed to be an important factor in the different ejection behavior.

The characteristics of particles generated by laser ablation have a strong influence on the chemical analysis of the irradiated sample. Large particles are more difficult to completely vaporize and ionize, and induced preferential vaporization causes fractionation (i.e. a detected chemical composition that differs from the sample material). Large particles also result in spikes in measurements using inductively coupled plasma mass spectrometry (ICP-MS) which result in errors. Three different methods were employed to study the effects of particle size on chemical analysis: generating smaller particles utilizing a fs laser, filtering out larger particles with a cascade impactor and altering the size distribution by using a second pulse to fracture particles generated from the first pulse.

It was found that the chemical composition of the particles varies with particle size. The variation of the composition with respect to particle size was analyzed and it was proposed that it was related to the vapor formed particles condensing on larger ejected liquid droplets

_____

Chair, dissertation committee

to my best friend and dear wife Te-Ming (Angela)

who supports me all the way

and to my loving parents

who give me a wonderful life and education

Table of contents

Chapter Six

Chapter Seven

List of Figures

Chapter Two

Chapter Three

Chapter Four

Chapter Five

Chapter Six

Acknowledgements

Enough cannot be said about my gratitude and love to my dear wife, Te-ming. All efforts cannot be done without her full support, patience and forgiveness. It's the thirteen year since we met each other, and we have gone through college, military service and long distance separation in the US. The past years are one of my happiest days because her companionship supported me to finish my dissertation. I am also very indebted to my loving parents; they gave me a wonderful live and constantly support me with everything I need. My mother and father were always there for me whenever I seek console and guidance. I am proud to have them as my parents, and hope they also feel proud to have me as a son. I also would like to thank my dear younger sister, Chun-chi, who also graduate this year, her encourage gave me a lot of strength.

I would like to thank my research advisor Professor Ralph Greif of Mechanical Engineering Department at UC Berkeley. I am very lucky to have him as my advisor. He has assisted me in finding a position at Lawrence Berkeley National Laboratory and made the research possible. I greatly appreciated his detailed review and help of my research and his genuine advice to me both life and academics.

I also would like to thanks Dr. Richard E. Russo, who is the leader of the "Advanced laser Technology" lab. He provided me the opportunity to do my research in this very friendly group "*Team Destructo*" of the LBNL. I am greatly indebted to his tolerance of my research progress and his useful help in guiding my

research directions and mostly, tremendous patience in reviewing my raw manuscripts. His guide and advice helped me dearly.

I thank my colleagues at “Team Destructo” for their generous help through my study. Special thank goes to Dr. Xianglei Mao, he helped me set up the experiment and was the constant consulting database all the years. I thank Dr. Jhanis Gonzalez for his help and friendship, which is important to me. I also would like to thank Syber Wen, who is a fellow PhD student, who offers great help in theoretical predictions.

Finally, I would like to thank Professor Per F. Peterson and Professor Costas P. Grigoropoulos for reviewing my dissertation and providing valuable comments and suggestions.

CHAPTER ONE

INTRODUCTION

1.1 Laser ablation: Overview

Systematic study of laser-material interactions flourished soon after the introduction of the first ruby laser in 1960. Since the 1970s, solid state Nd:YAG (Neodymium-doped Yittrium Aluminum Garnet) lasers have been applied to laser-material interactions research for their stable and optically superior beam delivery. In the 1980s, ultrashort laser with pulse durations in picoseconds and even femtoseconds became available via the development of the pulse compression technology [1]. Because of the shorter pulse duration, the high power laser density is made possible. The result together with the other versatility of including tunable wavelength, solid state lasers resulted in the marvelous progress in research and applications of laser-material interactions. Since the late 1970s, the application of laser processing of semiconductors, microstructures and thin films began to attract enormous interest with advanced lasers. Laser-assisted techniques include laser annealing [2], laser cleaning of surfaces [3], lithography [4], etching [5] and drilling [6].

When a high-power pulsed laser beam irradiates a target material, mass removal and plasma formation occur. Laser ablation [7] represents this dramatic laser-material-interaction phenomenon. The amount of mass removed and the energy of the laser-induced plasma varies depending on the laser parameters (pulse duration,

energy, and wavelength), the solid target properties and the surrounding environment. When a laser pulse reaches the sample surface, some of the energy is reflected from the surface where the reflectivity depends on the material and laser wavelength. The part of energy absorbed by the sample is distributed from optical photons to the electrons and then transferred to the lattice. Extremely high-energy inputs may cause photochemical reactions, which release the atoms and molecules from the surface. The surface when heated by the laser energy can reach very high temperatures even close to critical point; therefore significant vaporization may happen. The rest of the energy diffuses into the material via heat transfer. Depending on the applied laser energy, the surface may melt into a liquid with a moving solid-liquid interface. Liquid may be removed from the molten pool as droplets that result in a higher ablation rate. For some materials thermal stress effects are important which may cause the solid target to fracture from the surface. The detailed description of material removal procedures will be discussed in the chapter on ablation mechanisms.

Laser ablation is a powerful technology for direct sample chemical analysis [8], thin film deposition [9], micromachining [10]. The applications of laser ablation are now discussed:

1.1.1 Micromachining

Laser micromachining has the advantage of direct-write capability which can save the expensive lithography steps which are required in traditional wet or dry etching methods. Almost all materials can be machined with a properly selected

wavelength and fluence. Laser micromachining can achieve three-dimensional fabrication of microstructures in contrast to other etching technologies. In recent years advanced lasers with ultrashort pulse duration (sub-picoseconds even femtosecond) have gained more interest in micromachining because the pulse duration is less than the typical thermal equilibrium characteristic time (a few picoseconds), so that smaller thermal diffusion depth, high-precision and sharp ablation with minimal damage can be achieved [11,12]. In addition, femtosecond laser beam does not interact with the laser-induced plasma because of its short pulse duration; thus, absorbed laser energy is fully deposited on the target and higher efficiency of material ablation can be obtained [13].

1.1.2 Direct chemical analysis

Traditional chemical sampling methods usually require tedious sample preparation processes, which generate toxic waste and are very time-consuming. Further difficulties may be present because some sample like uranium cannot be easily dissolved into chemical solution; thus creates challenging tasks for chemical detection for these samples. Laser ablation provides a promising technology for direct chemical analysis; its superiority includes minimal sample preparation, minimal sample removal, no toxic waste and that it can remove any kind of material. Laser ablation enables direct vaporization of solid samples for elemental analysis with inductively coupled plasma atomic emission spectroscopy or mass spectrometry. With the method of atomic emission spectroscopy, LIBS (laser-induced breakdown spectroscopy) uses single or multiple lasers to ablate and then

atomize material from a sample and create a plasma. The plasma can be analyzed by emission spectroscopy to identify elements within the sample [14-16]. Besides studying optical emission spectra, a very popular method in chemical analysis is laser ablation combined with ICP-MS (inductively-coupled plasma mass spectrometry). Laser removed material including atoms and larger particles are all transported into ICP-MS, they are ionized in the induced plasma and analyzed in the mass spectrometry. Not restricted to only atomic information like ICP-AES, better precision and accuracy can be achieved and the ratio of elements can be quantified. This novel technology is applied widely in numerous fields [17-19].

1.1.3 Thin film deposition

Pulsed-laser deposition (PLD) is the process where laser pulses ablate material from a target and deposit it onto a substrate. Because it is a clean and fast process and the film thickness can be precisely controlled, pulsed laser deposition of thin films have advantages over conventional methods such as chemical vapor deposition (CVD) or physical vapor deposition (PVD). Rapid nonequilibrium heating of the target results in evaporation of different elements and then deposition of multiple component films on the substrate. Stoichiometry of deposited films can be achieved by selecting appropriate wavelengths at shorter pulses [20].

1.1.4 Nano Material fabrication

Nanotechnology has the advantages of generating materials with new optical, electrical and mechanical properties. A recent application of laser ablation is the fabrication of nanometer-sized materials like nano particles or nano wires. The

nano materials can be fabricated using laser ablation to remove atoms from the sample and which are then condensed into particles, wires or tubes under specially designed processes [21,22].

Using lasers for material processing requires the fundamental knowledge of the interactions of the incident laser with material. This interaction is a very complicated process; the coupling of intense electromagnetic energy of a laser pulse with a target material can result in melting, vaporization, ejection of atoms, ions, and molecular species, as well as shock wave formation and plasma development [23]. For high irradiance laser ablation, the material may be heated rapidly with both optical and thermal properties changing dramatically. The expansion of the vapor into the ambient gas compresses the ambient gas resulting in formation of shockwave; the vapor can also interact with the latter part of the laser pulse and create a highly non-equilibrium plasma. These processes influence the laser energy that can be transmitted to the sample. Due to the complexity of the laser ablation phenomena, the study of laser ablation has been limited by incomplete knowledge of the mass removal mechanisms. Today, one of the most important issues in laser ablation application is the control of the mass removal as well as the size and shape of the material removed. A detailed understanding of the mechanisms and effects of the laser-generated material is crucial to the success of laser ablation technology.

1.2 Scope of the present research

Laser ablation is a developing technology that applies single or multiple laser pulses on sample surfaces to remove materials. The removed material then is transported or collected with applications including nano-material fabrication, chemical analysis, combined with the removal of material; micromachining can also be also achieved using this technology. The products of laser ablation involve nanometer-sized aerosols as well as larger micron sized particles. The mechanisms as well as the properties of these particles are not well known though many applications have been established using this novel method. For example, nano particles can be fabricated when laser ablated vapor condenses into small particles. However, how these particles are formed and the influences of laser parameters on the properties of the particles are still not well known. Another problem may arise in chemical analysis using laser ablation is “fractionation” may occur, which means that the detected chemical composition is different than the sample composition; this often occurred when doing chemical analysis using laser pulses.

This dissertation covers particle generation during laser ablation, which includes particle generation mechanisms, and also studies laser ablation applications especially in chemical detection. In Chapter 2, laser ablation mechanisms are introduced In Chapter 3, methods of particle size measurement are introduced and the size distribution of laser ablation particles is measured with respect to different laser parameters including wavelength, laser energy, pulse duration and the ambient gas. The knowledge of the laser parameters, which influence the generation of particles, provides information for controlling the size and properties

of the laser ablation particles. In Chapter 4, a series of shadowgraph images detail the removal of liquid droplets as well as solid particles. This chapter provided strong evidence of the reflected shockwave and its effects in generating large amounts of particles. In the past, the concept of a “recoil pressure” has been used to describe the reasons for the particles ejection but without a detailed understanding of the phenomena. Chapter 5 discusses the variation of the chemistry of particles with size for binary metal alloy (brass); the proposed model that vapor condensed particles deposited onto liquid ejected droplets can explain this result. In Chapter 6, the effects of particle size on laser ablation applications are addressed including the improvement in chemical detection and enhanced crater removal. Chapter 7 is the conclusion and includes future study recommendations.

1.3 References

1. D. Strickland and G. Mouro, "Compression of amplified chirped optical pulses," Opt. Commun **56**, 219 (1985)
2. Tsukamoto, H. and Suzuki, T. Solid-State Electronics 42, 547. 1998.
3. Zapka, W., Ziemlich, W., Leung , W. P., and Tam, A. C. Microel.Engin 20, 171. 1993.
4. K. Jain, "**Excimer laser lithography**," 1990).
5. G. T. A. Kovacs, N. I. Maluf, and K. E. Petersen, 1998), pp. 1536.
6. J. F. Ready, ***Industrial Applications of Lasers*** , (**Academic Press**, **New York**, 1978).
7. ***Laser Ablation and Desorption***, J.C.Miller and R.F.Haglund, eds., (**Academic**, **New York**, 1998).
8. Russo, R. E., Mao, X. L., and Borisov, O. V. Trends in Analytical Chemistry 17, 461. 1998.
9. Sankur, H. and Cheung, J. T. Appl.Phys.A 47, 271. 1988.
10. J. J. Ritsko, in ***Laser Micro-Fabrication: Thin Film Processes and Lithography***, D.J.Ehrlich and J.Y.Tsao, eds., (**Academic**, **San Diego**, 1989).
11. Lenzner, M., Krausz, F., Kruger, J., and Kautek, W. Applied Surface Science 11, 154-155. 2000.
12. Rudolph, P., Bonse, J., Kruger, J., and Kautek, W. Applied Physics A 69, S763. 1999.

13. Le Drogoff, B, Margot, J., Chaker, M., Sabsabi, M., Barthelemy, O, Johnston, T. W., Laville, S., Vidal, F, and von Kaenel, Y. Spectrochim.Acta Part B 56, 987. 2001.

14. Barbini, R., Colao, F., R.Fantoni, Palucci, A., and Capitelli, F. Appl.Phys.A 69, S175. 1999.

15. Fichet, P., Mauchien, P., Wagner, J. F., and Moulin, C. Anal.Chim.Acta 429, 269. 2001.

16. Yoon, Y., Kim, T., Yang, M., Lee, K., and Lee, G. Microchem.J 68, 251. 2001.

17. J. Gonzalez, X. L. Mao, J. Roy, S. S. Mao, and R. E. Russo, "Comparison of 193, 213 and 266 nm laser ablation ICP-MS," Journal of Analytical Atomic Spectrometry **17**, 1108-1113 (2002)

18. B. Hattendorf, C. Latkoczy, and D. Gunther, "Laser ablation ICP-MS," Anal. Chem. **August**, 341A-347A (2003)

19. R. Wolf, C. Thomas, and A. Bohlke, "Analytical determination of metals in industrial poolymers by laser ablation ICP-MS," Appl. Surf. Sci. **127-129**, 299-303 (1998)

20. Kwok, H. S., Mattocks, P., Shi, L., Wang, X. W., Witanachchi, S., Ying, Q. Y., Zheng, J. P., and Shaw, D. T. Appl.Phys.Lett. 52, 1825. 1988.

21. Y. Zhang, W. Z. Chen, and W. G. Zhang, "Studies on nano-cobalt/ethanol sol prepared by pulsed laser ablation," Chemical Journal of Chinese Universities-Chinese **24**, 337-339 (2003)

22. W. S. Shi, Y. F. Zheng, H. Y. Peng, N. Wang, C. S. Lee, and S. T. Lee, "Laser ablation synthesis and optical characterization of silicon carbide nanowires," Journal of the American Ceramic Society **83**, 3228-3230 (2000)

23. Russo, R. E., Mao, X. L., and Mao, S. S. Analytical Chemistry 74, 70A. 2002.

CHAPTER TWO

PARTICLE GENERATION MECHANISMS

2.1 Laser ablation and particles

Collected particles generated by laser ablation show that the size of particles varies from nanometers to several microns and the shape of the particles changes from spherical single particles to being totally irregular when they form agglomerates (Figure 2.1). Several mechanisms may be present permitting multiple size distributions to result from just one laser pulse. Nevertheless repetitive pulses further change the particle surface topography and increase the probability that larger particles are produced. The major mechanisms of particle generation are discussed in this chapter and their dependence on different laser parameters is addressed. This chapter is separated into two parts: laser ablation and the imaging of particles, and particle generation mechanisms induced by laser ablation.

When a laser pulse reaches a sample surface, some of the energy is reflected by the surface. It is noted that the reflectivity depends on the material and laser wavelength. The energy absorbed by the sample is transferred from optical photons to electrons and then to the lattice, which then diffuses the energy into the material. Extremely high energy pulses may cause photochemical reactions which remove atoms and molecules from the surface. The heated surface can reach temperatures close to the critical temperature and cause rapid vaporization process.

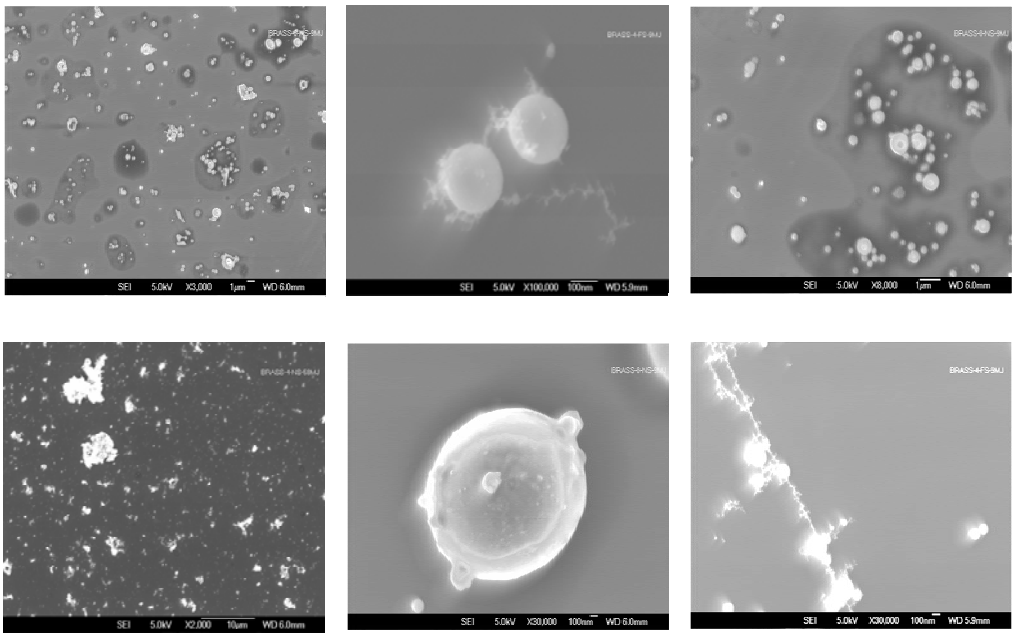

Figure 2.1 Selected particles observed in SEM images from laser ablation of brass

2.1.1 Onset of Laser ablation

A laser beam incident on a target creates a heated region that causes vaporization resulting in a plasma that consists of ionized vaporized atoms and electrons. It is possible that the plasma cloud absorbs some of the incident laser energy and thereby only allows a fraction of the laser energy to reach the surface (plasma shielding). The plasma expands and is heated by photon absorption. Later the vapor cools and aerosol particles begin to form. The characteristics of the aerosol particles (number concentration, shape, size distribution, etc) result from the effects of different processes. A series of events during laser ablation has been described by Lushnikov [2]; namely incident beam, plasma eruption, expansion of plasma cloud, nucleation, condensational growth, expansion of the cloud, coagulation and aggregation.

2.1.2 Plasma formation

The laser-irradiated region on the target surface is heated to high temperatures. It is found that a large portion of the absorbed laser energy is used to evaporate the atoms of the target material thereby reducing the energy transport into the interior of the target material. The front of the vapor formed plasma contacts the ambient gas and forms a shockwave (which travels faster than the speed of sound). The vapor plasma is in a strong nonequilibrium state with an ion density reaching $10^{16} - 10^{18}\ ions/cm^3$ (typical laser fluence ~ $1\,J/cm^2$). The characteristic time for the cloud formation is about 10^{-7} sec. The temperature inside the plasma can reach several tens of thousands K when all of the atoms and molecules are ionized.

2.1.3 Vaporization

The mass evaporizated from the target forms a vapor plume and moves away from the surface with a high temperature and pressure. The surface temperature primarily determines the vaporization rate. The evaporization rate from a liquid surface is given by: [3]

$$j_{ev} = n_l \left(\frac{k_B T_l}{2\,\pi\, m_a} \right)^{1/2} \exp\left(-\frac{h_{lv}}{k_B T_l} \right) - \theta_s n_v \left(\frac{k_B T_v}{2\,\pi\, m_a} \right)^{1/2} \tag{2.1}$$

where n is the number of atoms per unit volume, the subscripts l and v represent liquid and vapor, respectively, h_{lv} and T_v are the latent heat of vaporization and

temperature of the vapor, m_a is the atomic mass and k_B is the Boltzmann constant. The first term in equation (2.1) represents the evaporization rate from a liquid surface temperature T_l and the second term represents the condensation rate of molecules back to the liquid surface. The sticking coefficient θ_s is the probability that a vapor atom returning to the liquid surface is adsorbed.

2.1.4 Melting

The energy not used to vaporize the material heats the material, increases the internal energy and raises the temperature. The energy propagates via heat conduction inside the material. The temperature distribution is governed by the heat conduction equation:

$$\rho C_P \frac{\partial T}{\partial t} = \nabla \cdot \left(K \nabla T\right) + (1-R) I_0 \, \alpha \, e^{-\alpha z} \tag{2.2}$$

where ρ, C_p, K, T represent density, specific heat, thermal conductivity and temperature. The second term on the right hand side of equation 2.2 represents the source term which is the laser energy absorbed by the material at a depth z from the surface, where R is the surface reflectivity, I_0 is the laser irradiance and α is the absorption coefficient (the imaginary part of the complex refractive index, assumed to be constant). A detailed description of the thermal transport is given in [3].

For large absorbed laser energy, the solid material melts and the energy balance equations are: [3]:

$$T_s(z = z_{\text{int}}) = T_l(z = z_{\text{int}}) = T_m \tag{2.3}$$

$$K_s \frac{\partial T_s}{\partial z} - K_l \frac{\partial T_l}{\partial z} = h_{sl} V_{\text{int}} \tag{2.4}$$

where h_{sl} is the latent heat for melting, and V_{int} is the velocity of the interface normal for the surface. The moving interface is assumed to be isothermal at the melting temperature T_m . The velocity and location of the solid-liquid interface can be obtained which yields the thickness of the melt layer.

2.2 Particles generated from ablation (traditional concept)

The laser pulse energy reaching the target is used in vaporizing the material; some of the energy is also transported by heat conduction inside the sample. The solid- liquid interface propagates into the sample and produces the melt region. The particles produced by vaporization may account for a small portion of the total mass removal; thus other mechanisms are responsible for most of the material removed. The products of laser ablation contain atoms, vapor, liquid droplets and even solid particles. Particle ejection mechanisms are discussed in the following section.

2.2.1 Nucleation and condensation

As the vapor plume propagates outward and starts to cool, the cooler front

of the plume cloud allows aerosol particles to form. The characteristic times for particle formation are typically on the order of nanoseconds (10^{-9} sec), which is much shorter than the duration time of the cloud. The much shorter time scale for the particle formation ensures that the vapor will be transformed into particles. Condensation of the vaporized atoms is the mechanism for the generation of nano-sized particles. The ambient pressure, gas properties and temperature are critical factors in condensation processes. Most numerical studies that have been made of this process calculate the shock location and the gas properties. Condensation processes were predicted when the plasma temperature decreased to a sufficiently low value related to the vapor number density. Experimental results usually found the size of the particles to be between several to several tens of nanometers. The molecules collide with each other and form larger aerosols; however the probability of forming particles as large as microns is very low since extremely high collision frequencies and atom number densities would be required. The larger particles are generated by other mechanisms, which are described below.

2.2.2 Solid exfoliation

Exfoliation is the removal of fractured material in the solid state caused by photomechanical effects due to strong laser-induced thermal expansion and stress. This kind of removal is particularly important for brittle, refractory materials such as single crystal materials including silicon, graphite or glass type materials. The magnitude of the laser-induced stresses becomes significant under conditions of

stress confinement, when the laser pulse duration is shorter then the time needed for mechanical equilibration of the absorbing volume. The particles are usually cleaved along crystallographic planes. The particles are of large size and evidently irregular shape. The sample surface after an exfoliation process can also be easily identified by the shape of the crater.

2.2.3 Hydrodynamic sputtering

Unlike exfoliation; that is, particle ejection in the solid state, the most common ejection is that of particles in the liquid state. Their spherical shape that is caused by surface tension can identify particles ejected in the liquid state. However, even though it was easy to identify those particles that were ejected in the liquid state, there are several different mechanisms that could cause the liquid to leave the surface. Among them, hydrodynamic sputtering which is caused by cyclic heating and cooling of the surface is frequently observed in laser ablation [1,4]. The term hydrodynamic sputtering is typically used to refer to a range of processes in which large droplets are ejected as a result of a transient melting and motion of a liquid caused by steep thermal gradients and relaxation of the laser induced pressure. When the laser fluence is sufficient to melt the surface, cyclic heating and cooling of the surface leads to the growth of perturbations and produces finger-like or ridge-like surface structures. Kelly [1] proposed that liquid droplets could be ejected from a melted layer as the acceleration of a liquid asperity (protrusion on the surface which is related to thermal expansion) exceeds the force holding the liquid to the surface

(related to surface energy). The size of the ejected droplets can be obtained from the following equation: [1]

$$r_{\min} \approx \left\{ \left[\frac{6\gamma}{\rho_l} \frac{1}{\Delta L} \right] (\Delta t)^2 \right\}^{1/2} \tag{2.5}$$

$$\Delta L = 2r\alpha\Delta T + 2r(\rho_s - \rho_l)/3\rho_s \tag{2.6}$$

where $r_{\min}$ is the most probable droplet size that can be expelled, γ is the liquid surface tension, ρ_l and ρ_s are densities for the liquid and solid phase respectively, α is the linear thermal expansion coefficient, ΔT is the temperature difference between the surface and melting point, and Δt is the laser pulse duration minus the time at which the surface temperature reaches the melting point. The ejected droplet size resulting from "hydrodynamic sputtering" varies with the properties of the melting material ($\gamma, \rho_l, \rho_s, \alpha$), which vary with the temperature, and the chemical composition of the melting surface. Studies of surface morphology after laser irradiation on metals provide strong support for the large-droplet ejection from the hydrodynamic mechanism [1]. The calculated size of particles and the size of the asperities agreed with the results in SEM images in the range of 100-200 nm. However, larger micron-sized particles cannot be explained using the hydrodynamic sputtering model that suggests other mechanisms are responsible for the large particles.

2.2.4 Micron-sized particle ejection (Spallation)

Hydrodynamic sputtering which was discussed in the previous section cannot produce the micron-size particles that are observed. The spherical shape of the particles demonstrates its origin from the liquid state. These large particles account for most of the mass removal from laser ablation. The formation of the large particles is similar to that from exfoliation except they are formed from the liquid surface. The large particles are formed from the melt near the liquid-solid interface. In the regime of stress confinement the laser-induced stresses can exceed the dynamic tensile strength of the target material, causing disruption of a liquid-solid interface.

When the high-energy laser pulse arrives at the target surface, the vaporized material generated a vapor plume that propagated outward in the open gas ambient. The pressure and temperature of the plume are very large especially in the initial stage of the vapor plume formation. The high pressure may push the liquid melt out from the center of the laser-heated region and after the melt is cooled form a “volcano-shaped” crater. A raised rim is usually found around the crater that is strong evidence of the once melted surface. When the pressure is sufficiently large the resulting momentum surpasses the surface tension, which is holding the liquid to the surface, and droplets are ejected around the rim. These particles are reported to be caused by the back-coil or recoil pressure. The limit of the particle size is therefore the thickness of the melt layer and particles as large as several microns were reported. Figure 2.2 shows several images of particles ejecting from a silicon target that were obtained in the present research.

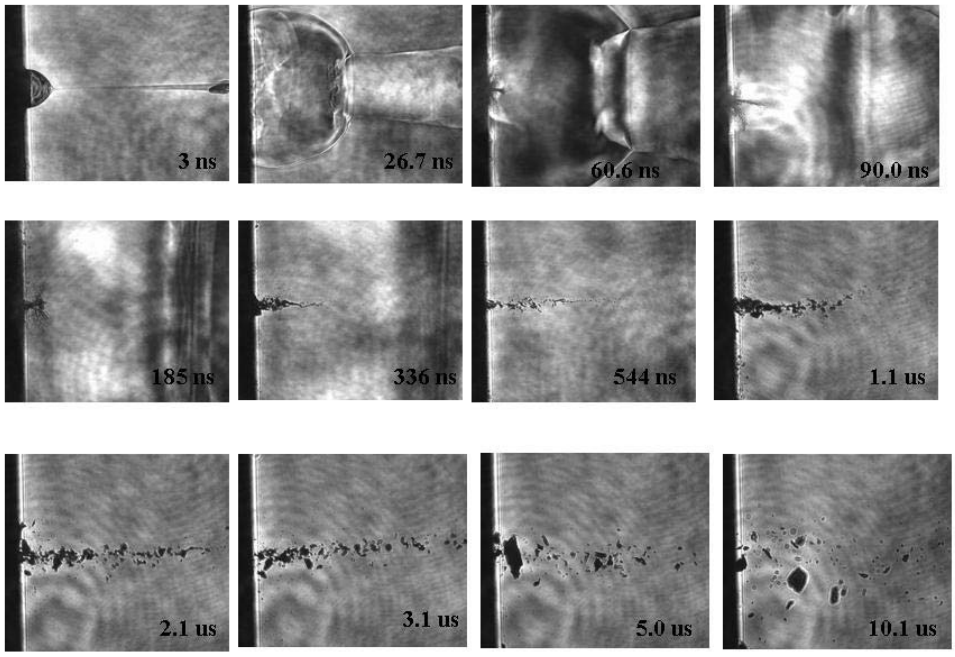

Figure 2.2 Images of silicon particle ejection at different delay time

2.2.5 Phase explosion

Another mechanism that causes a large amount of mass removal is considered to be phase explosion or explosive boiling. Although explosive boiling or phase explosion has been discussed as a primary mechanism of short-pulse laser ablation in a number of works, the detailed process for this kind of particle generation is yet to be studied. When a very high-energy fluence laser pulse is applied on the target surface, a dramatic change of crater shape and volume is reported. The ablation rate measured from the crater depth changes abruptly when the energy power density is larger than a critical value. This mechanism has been analyzed based on classical thermodynamics. When the surface region is heated beyond the limit of its thermodynamic stability during short-pulse laser irradiation, the surface is presumed

to undergo a rapid transition from a superheated liquid to a mixture of vapor and liquid droplets. Experimental results of the existence of well-defined threshold fluence for the onset of the droplet ejection, as well as a steep increase of the ablation rate at the threshold, have been reported and interpreted as evidence of the transition from normal vaporization to phase explosion. For example, Jong [6] reported the ablated crater depth of a silicon sample increased from 4 to 20 microns when the laser power density increased from 19 to 21 GW/cm^2. This kind of dramatic change in crater properties has been reported by many researchers on various materials including silicon, lead, copper, and glass and is the most efficient way to remove material during laser ablation.

2.2.6 Coagulation and agglomerates

Besides the main particle generation mechanisms discussed in sections 2.2.1 to 2.2.5, there are several minor mechanisms, which will not generate particles but may alter the particle size distribution or the total particle number concentrations. These processes can occur from several nanoseconds to several milliseconds after the laser pulse.

Two most important processes were coagulation and agglomeration, which would usually increase the final particle size. Particles after forming from laser ablation collide with each other in the gas ambient, and if the momentum is large enough or the participant particles are in liquid phase, particles coalesce to form new large particles. This process is called coagulation and usually happens in the later

time stage. Agglomerates are formed as early soon condensation starts, when the nano sizes aerosols are formed from vapor, they are strongly charged with electrons existing in the plasma. The charged particles then attach to each other by the electronic bond and the agglomerates are identifiable by their chain or web shape.

2.3 Summary

The generation of particles in laser ablation processes is highly dependent on the laser parameters and the material properties. The magnitude of the laser energy changes the mass removal mechanism from pure vaporization to liquid ejection and eventually even phase explosion when very high energy is involved. Ambient parameters including the gas properties and pressure affect the formation of particles condensed from the vapor phase. The mechanical properties of the material may influence whether large scale of exfoliation or spallation would occur even under the same laser conditions. The control of the particle generation is indeed a complex task and further study is required to understand the phenomenon.

One of the most important parameters in particle generation is the laser energy; some mechanisms like vaporization are dominant at low laser fluence but become less important as hydrodynamic effects or phase explosion prevail when laser fluence increases. Figure 2.2 is a series of shadowgraph images of laser ablation of silicon sample taken with high laser irradiance ($\sim 30\, GW/cm^2$), where several of the particle generation mechanisms can be discerned from the images. The starting of the plume can be observed as early as several nanoseconds after the laser pulse; the high

temperature and pressure plume pushes the ambient gas away and forms the shockwave. A contact surface exists between the vapor plume and the ambient gas. Though not very clear, the area of the vapor can be observed in Figure 2.2 by its darker color in the image following the shockwave. As the time advances, the vapor plume and the shock wave expand outward into the ambient gas. The speed of the shock wave is measured to follow the power law, which involves energy, density and time. Detailed discussions of the shockwave propagations are given in chapter 4. At ~ 50 nanoseconds after laser pulse, particles ejected from the surface can be observed. These particles ejected from the surface are caused by spallation. However at high laser fluence, very large particles (~10 microns) were observed which erupted perpendicular from the surface at about 1 microsecond after the laser pulse. These big particles were suspected to result from the phase explosion phenomenon [5,6] and their relative round shape confirmed that they were formed in the liquid phase. The process lasted until about 10 microseconds after the laser pulse. At later time (20 -30 microseconds after the laser pulse) very big particles estimated as large as 20-30 microns were generated; the irregular shape of the particles can be easily discerned which identified themselves as solid exfoliation products. Different mechanisms of particle generation can be observed during this ablation process. Chapter 4 is dedicated to the formation of liquid droplets during laser ablation.

References

1. R. Kelly and J. E. Rothenberg, "Laser Sputtering .3. the Mechanism of the Sputtering of Metals Low-Energy Densities," Nuclear Instruments & Methods in Physics Research Section B-Beam Interactions with Materials and Atoms **7-8**, 755-763 (1985)

2. A. A. Lushnikov, "Laser induced aerosols," J. Aerosol Sci. **27**, S377-S378 (1996)

3. A. M. Prokhorov, V. I. konov, I. Ursu, and I. N. Mihailescu, *Laser heating of metals*, (Adam Hilger, New York, 1990).

4. R. L. Webb, J. T. Dickinson, and G. J. Exarhos, "Characterization of particulates accompanying laser ablation of NaNO3," Appl. Spectrosc. **51**, 707-717 (1997)

5. J. H. Yoo, O. V. Borisov, X. L. Mao, and R. E. Russo, "Existence of phase explosion during laser ablation and its effects on inductively coupled plasma-mass spectroscopy," Analytical Chemistry **73**, 2288-2293 (2001)

6. J. H. Yoo, S. H. Jeong, R. Greif, and R. E. Russo, "Explosive change in crater properties during high power nanosecond laser ablation of silicon," Journal of Applied Physics **88**, 1638-1649 (2000)

Chapter Three

Particle size in laser ablation

3.1 Scope of this chapter

The methods of particle size measurement and the effects of laser parameters on particle size are presented in this chapter. To understand how the laser parameters affect the generation of aerosol particles during ablation processes, we do need to know the size distribution of these particles that aids in understanding the particle growth mechanisms. In addition, the potential to control the particle size in laser ablation can lead to tremendous improvement in applications ranging from nanostructure fabrication to chemical analysis. In section 3.2, different particle size measuring methods and the basic theory they are based upon are described. Two different particle size observations are discussed in sections 3.3 and 3.4. SEM images of the collected particles from ns and fs laser are presented in section 3.3 to represent the offline method. Particle size measurement using DMA (differential mobility analyzer) with different ablation parameters are presented in section 3.4.

3.2 Particle size measurement theory and method

In most applications involving laser ablation, the processes are operated in a gas environment. The solid particles or liquid droplets in gases are categorized as aerosols. Only those particle size measuring methods designed to work in the gas

phase can be used to measure the particle size in laser ablation processes. Usually, for large aerosol particles, light scattering and cascade impactor methods are used. For small aerosol particles, the diffusion battery is commonly used. For intermediate particles, the differential mobility analyzer (DMA) is often used. The condensation nuclei counter (CNC, or CPC) is often used for determining the number density of small particles; it can be used to obtain the real time particle size distribution. In this work, the methods of the Cascade Impactor, the Diffusing battery and the DMA were used. The advantages and disadvantages of the different methods will be discussed in the following paragraphs.

3.2.1 Particle diameter

Most of the time the aerosol particles are not spherical in shape; they can be cylindrical and ellipsoidal and in different orientations. Highly irregular particles are also commonly observed which pose a major difficulty in making particle measurements. For irregular shaped particles, it is convenient to retain the Stokes equation with d as an equivalent diameter, e.g. the diameter of the sphere having the same volume as the body. The Stokes law for the drag on a sphere of diameter d, is:

$$F = -\frac{3\pi \mu d U}{C} \qquad (3.1)$$

where C= Cunningham slip correction (To correct the slip effect for small particles), μ = gas viscosity, d = particle diameter, U = flow velocity

Two different but related effective diameters were introduced; the Stokes diameter and the aerodynamic diameter. The Stokes diameter of a particle is defined as the diameter of a sphere with the same density as the original particle while the aerodynamic diameter is the diameter of the particle with unit density. In applications, the aerodynamic diameter is more useful than the Stokes diameter because it does not require knowledge of the particle density, which may be difficult to determine. Thus, the aerodynamic diameter is generally used for most experimental methods.

3.2.2 Cascade impactor and diffusing battery

Cascade impactor

A cascade impactor is a device used to collect or filter out large particles from the aerosol flow. When the aerosol flow streams from a round nozzle and impinges on an impact plate, the flow streamlines and the particles within turn and move in the direction parallel to the plate. While the fine particles follow the streamline and are carried away with the flow, the heavy particles cannot follow the streamlines and impact the surface; and adhere to the impactor plate. A cascade impactor consists of a series of impactor plates; the smaller particles being carried away by the flow reaching the next impactor stage with a different geometry on which different sizes of particles are deposited.

The characteristic factor for the cascade impactor is the cutoff diameter of the particles D_{50}; this is the aerodynamic particle size at which the particles are filtered.

The cutoff diameter is a function of the flowrate and nozzle diameter and is calculated from the following formula:

$$D_{50} = \sqrt{\frac{9\pi\, Stk\, \mu W^3}{4\rho_p CQ}} \qquad (3.2)$$

where Stk = Stokes number = 0.23 for air, ρ_p =particle density, Q=volumetric flowrate, W=nozzle diameter

Different sizes of particles are collected on separate impactor stages. By weighing the mass of the particles on each plate, the mass distribution for each particle size range is obtained. Knowing the density of the particles, the mass distribution can be converted to volume distribution, dividing the nominal particle in each impactor stage; the number distribution can also be obtained. The collected particles can also be dissolved using acid for chemical analysis or observed with a microscope. The new application of the cascade impactor is electrically monitoring of each impactor stage since the particles possess charges; the electrical signal is then converted to the real time particle size distribution. Though simple to use, the main drawback of the cascade impactor is that it is not efficient for small sized particles. In many applications, an impactor is installed before the inlet of sensitive devices to filter out large particles that cause noise in detectors and/or damage the devices.

Diffusing Battery

A diffusion battery works in the opposite way that the cascade impactor does. A cascade impactor filters out larger particles while a diffusion battery filters out small aerosols in the flow. The motion of aerosol particles smaller than 200 nm in

diameter is strongly affected by diffusion (random collisions with gas molecules) which results in a random path. The diffusion coefficient of an aerosol particle is given by:

$$D = \frac{k\,T\,C}{6\,\pi\mu\,a_p} \tag{3.3}$$

where k = Boltzman constant, T = absolute temperature, a_p = particle radius, μ =viscosity

As particles pass through a fine-mesh screen, some particles will collide with the screen wires and stick to it. Smaller particles are more likely to collide with the screen because of their higher diffusion coefficient. Thus the penetration function (percentage of particles that pass through the mesh), P, of “small” particles is less than for “large” particles. The governing equation of this function is given as: [1]

$$P = \exp(-4.52n\,Pe^{-2/3}) \tag{3.4}$$

where, n = number of screens, Pe = Peclet number = $2\,aU_0 \big/ D$, a = screen wire radius, U_0 = Undisturbed flow velocity, D= Diffusion coefficient. With a sequence of mesh screens, we can filter out particles smaller than the desired select size.

3.2.3 Direct observation of particles

In applications like pulsed laser deposition (PLD) or laser sputtering, laser generated aerosol particles are collected on target plates. The actual cutoff size value of the cascade impactor is obtained from the particle sizes collected on the impactor stages. Using the microscope provides the information of shape and

structure of the aerosol particles. Scanning electron microscopy (SEM) and Transmission electron microscopy (TEM) are widely used. Using the microscope, particles are observed and recorded directly without distortion. The high resolution of the SEM or even the TEM can be on the order of several nanometers or smaller (aerosols of this size sometimes cannot be observed using other methods) which is very critical in nano technology applications. Using a microscope reveals the true shape of the particles and may indicate how the particles were formed. For example,we can determine the if the aerosols are chain like with particles agglomerated together.

For all other indirect particle measuring methods, the shape of the aerosols is assumed to be spheres; thus the size measurement would differ from the actual value.

Though using a microscope is the most direct way to observe particles, the process is cumbersome. A major drawback of using techniques like SEM is that it does notprovide real-time measurements. Particles need to be collected in one position and then examined in another place; particles may be lost or distorted during the transport and storage process and preparation of the sample species is important since unwanted dust or particles may cause errors. Nevertheless, after particles are recorded by microscope images, we are able to count them using customized software. This is particularly important for the study of nano particles, e.g. in the study of the condensation of aerosol particles from laser ablated vapor.

3.2.4 Light scattering

The method of light scattering is probably the most popular way to determine the size of particles but it is also quite complex. The effects of light scattering range widely from sky color, rainbow to haloes, and levitation by radiation pressure to biological particles. Sizing of particles is one specific application. The nondestructive and rapid response of the light scattering method makes it very useful.

Though the sizing method of light scattering is not discussed in this dissertation, detailed information on light scattering by small particles can be found in [2]. Pulses of light are scattered by particles into a set of directions and are detected and sorted electronically. The particle size distribution is determined utilizing a calibration curve relating signal magnitude to particle size. A nephelometer is a device which uses light scattering to detect particles. Aerosol particles flow through a chamber where a laser beam passes through. The intensity of the scattered light varies with angles. The light scattered by the particles is detected by photodiodes deployed at different angles so the variation of light intensity with angle is obtained. By applying Mie theory (or Rayleigh theory, depending on the size range of the particles) [2], the particle size distribution can be calculated. The challenge of this method is that the type of size distribution and the refractive index must be known in order to obtain accurate results. For many cases, the optical properties of the particles are not available and/or the particle size distributions are more complex than a single common log-normal distribution. Also the light scattering method also

is less sensitive to small particles and is best performed for particles of micron size or larger.

3.2.5 DMA

The differential mobility analyzer is based on the theory of electrical differential mobility. The purpose is to extract only a known size of submicron particles from the incoming poly-disperse aerosols. Before the particles enter the DMA, they are charged as they pass through an electrical charger. The charge distribution function can be obtained [3].

A simple schematic of a DMA is shown in Figure 3.1. The DMA contains two concentric metal cylinders. The poly-disperse aerosol (the aerosols to be extracted), and the sheath air flow (q_{sh}) are introduced at the top of the DMA and flow down the space between the cylinders without mixing with each other. The inner cylinder, the collector rod, is applied with a controlled negative charge while the outer cylinder is grounded so that an electric field is established between the two cylinders.

The electric field causes positively charged particles to be attracted through the sheath air to the negatively charged collector rod and deposited along it. The location of the deposited particles depends on the particle electrical mobility (Z_p), the flowrate and the geometry of the device. Particles with a high electric mobility are deposited along the upper portion of the rod and particles with low mobility collected on the lower portion. Only particles within a narrow range of electrical

mobility can exit with the now mono-disperse (particles of the same size) flow (q_m) through a small slit located at the bottom. These particles are transferred to a particle counter to determine the particle concentration. The remaining particles are removed from the DMA via the excess flow.

The electrical mobility Z_p is related to the size of the aerosol particles; the definition of Z_p is

$$Z_p = \frac{n_p\, e\, C}{3\pi\mu\, D_p} \tag{3.5}$$

where, n_p = number of elementary charges on the particle, e= elementary charge (1.6×10^{-19} *Coulomb*), D_p = Particle diameter

The electrical mobility can be determined without the knowledge of particle size. Knutson determines a relationship between the particle electrical mobility and the parameters of the device [4]:

$$Z_p^{\,*} = \frac{q_{sh}}{2\,\pi\, VL}\ln\left(\frac{r_2}{r_2}\right) \tag{3.6}$$

where, r_2, r_1= outer, inner radius of of annular space, V = average voltage on the inner collector rod, L = length between exit slit and polydisperse inlet

From equations (3.4) and (3.5), we can find the relation of the particle diameter to the DMA properties:

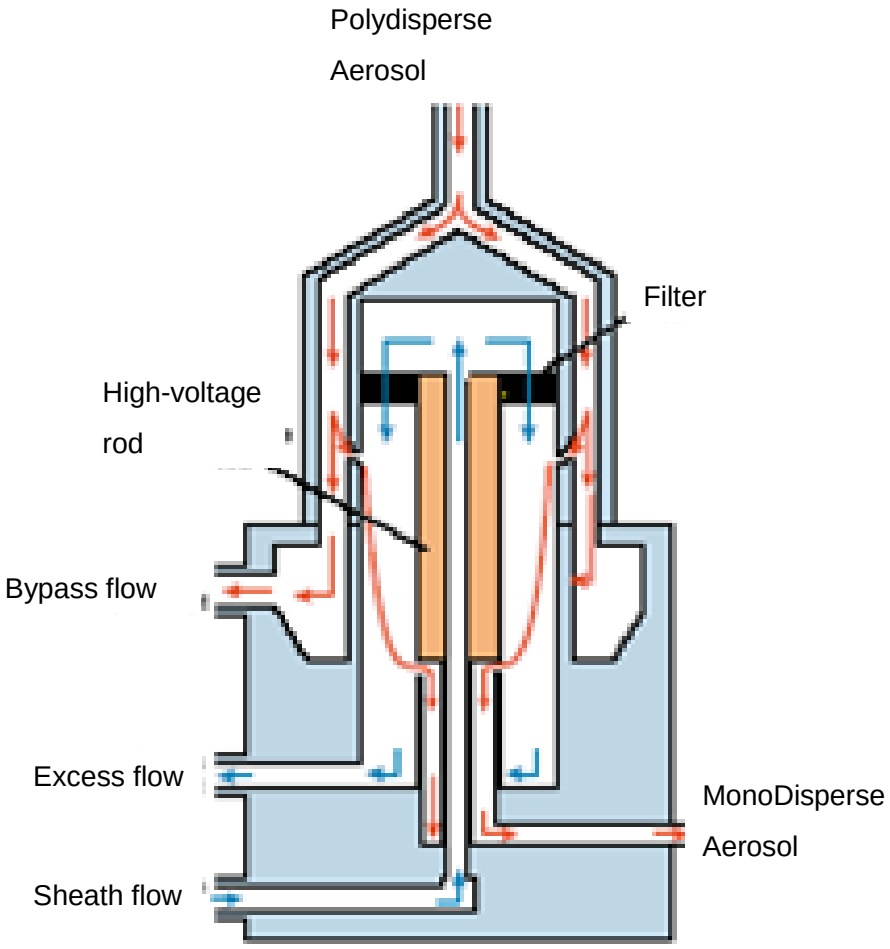

Figure 3.1 Sketch of a DMA

$$\frac{D_p}{C} = \frac{2n\, e\, \overline{V} L}{3\, \mu\, q_{sh}\, \ln\left(\frac{r_2}{r_2}\right)} \tag{3.7}$$

The equations do not account for diffusion broadening which is important for particles less than 50 nm [5].

Once the particles are classified by electrical mobility, the concentration is measured by a CPC or an electrometer. In this work, we used a scanning mobility

particle system (SMPS) which combines the DMA and CPC. By changing the voltage of the inner collector rod, the change of electric mobility allows different sizes of particles to leave the DMA exit and permits a real time particle size measurement to be obtained.

3.2.6 Other methods

All the methods mentioned above were tested or used in this dissertation including the light scattering method. The particle size range of each method is tabulated in Table 3.2. Results from the light scattering method are discussed in this dissertation since it did not yield satisfactory results probably due to the size of the particles being smaller than the detection limit for light scattering.

3.3 SEM images on particles: difference for fs and ns laser ablation

3.3.1 Experimental section

The experimental configuration is shown in Fig 3.2. The two lasers were a Nd: YAG laser with 6 ns pulse duration (New Wave Research, Minilase II) and a Ti: sapphire laser with 150 fs pulse duration (Spectra-Physics, TSA 25). To compare only the laser pulse duration influence on ablation behavior, the wavelength of both the femto and nanosecond lasers was adjusted to be 266 nm. For the nanosecond Nd: YAG laser, the fourth harmonic was achieved by quadrupling of the 1064 nm fundamental. For the Ti: sapphire femtosecond laser, it was the third harmonic of

the 800 nm fundamental. Both beam diameters before the focusing lens were 10 mm. Both lasers were operated at 10Hz repetition rate and at the same energy of 0.6 mJ and were focused on the sample surface, using the same lens, to a 100 um diameter spot size, which produce approximately $8\,J/cm^2$ fluence. The irradiance was the only difference; for the nanosecond laser, it was $1.3\times10^9 W/cm^2$ whereas for the femtosecond, it was $5\times10^{13} W/cm^2$.

Brass with a Zn/Cu ratio of 0.18 was used as the sample material for collection of ablation particles. However, a series of brass samples with a range of zinc to copper mass ratios (Zn/Cu) from 0.06 to 0.65 were used to study the matrix effects on ablation sampling. The study of particle chemistry using ICP-MS based on this experimental setup is discussed in Chapter 6.

The ablated mass was transported by argon gas out of the sample chamber with a 0.8 LPM (Liter per minute) flow rate. The particles were collected for SEM measurements. SEM measurements were used to study the actual particle shapes and sizes, the particles were collected on small clean silicon pieces. Particles were collected at the exit of the ablation chamber after a distance of 1 meter tubing. The particle collecting time for both nanosecond and femtosecond ablation was the same (2 minutes or 120 pulses).

The volume of the craters produced by the two different lasers was measured using a white-light interferometric microscope (Zygo, New View 200).

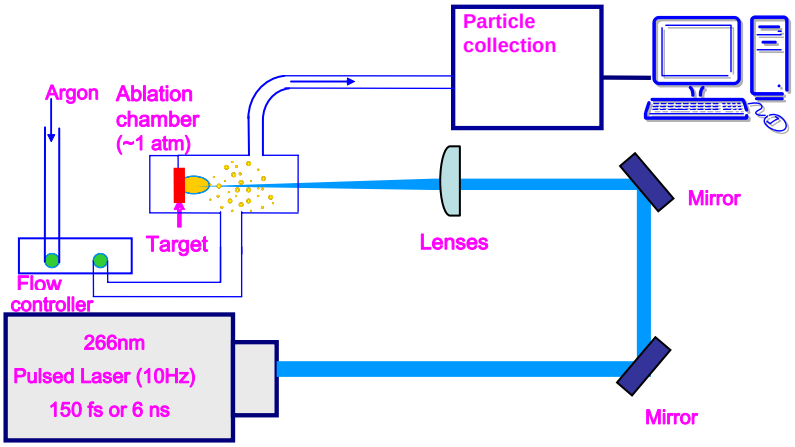

Figure 3.2 Experimental setup for laser ablation using fs or ns lasers

3.3.2 Results and discussion

SEM images (Fig 3.3) were obtained for particles collected at the exit of the ablation chamber tubing. The sample used was brass with 0.18 zinc/copper ratio. The sampling time was two minutes and particles were collected by passing the aerosol through an impactor with silicon as the impact surface. The number of particles collected from femtosecond laser ablation was greater than from nanosecond ablation, consistent with the larger ablation rate for femtosecond pulses (crater volume). The particle shapes and sizes were also different. Particles from nanosecond ablation were primary single and spherical, while those generated from femtosecond ablation were mostly agglomerates of small nano–sized particles. Agglomerates could be observed for both pulse-durations; large agglomerates of irregular shape with sizes of five to ten microns (Fig 3.3d) existed for femtosecond

laser ablation compared to smaller agglomerates for nanosecond ablation (Figure 3.3b). Further magnified SEM images of both samples (Figure 3.3d and f) demonstrate the detailed geometry of the collected particles. The majority of particles formed with nanosecond laser ablation were mostly single spherical (Fig 3.3c). Some of the particles were as large as several microns in diameter indicating that they have been ejected from the melted surface instead of being condensed from the ablated plasma vapor.

The sizes of particles from nanosecond ablation ranged widely from several tens to thousands of nanometers. The ‘large’ particles from femtosecond ablation shown in Fig 3.3f have a different structure. These ‘large’ particles were agglomerates of smaller particles. The primary particles were the size of 100-200 nanometers, which were connected to each other by chains having dimension of about several nanometers in diameter. There were no single large droplets like those observed with nanosecond ablation, suggesting that melting and ejection of molten mass is less prominent with femtosecond ablation. It is not clear if the agglomeration was formed in the plume or at the impactor surface or during transport. Chain-like agglomerates have been reported in laser ablation and should have been formed before they arrived on the impactor surface. However, the great number of the chain like agglomerates may collide amongst them and form the large agglomerates as they approached the surface and were being collected. In principle, large droplets should not be transported as efficiently as smaller ones. However, the

agglomerates may not behave as single entities. Particle agglomeration is related to size; smaller particles have a greater tendency to agglomerate than larger ones.

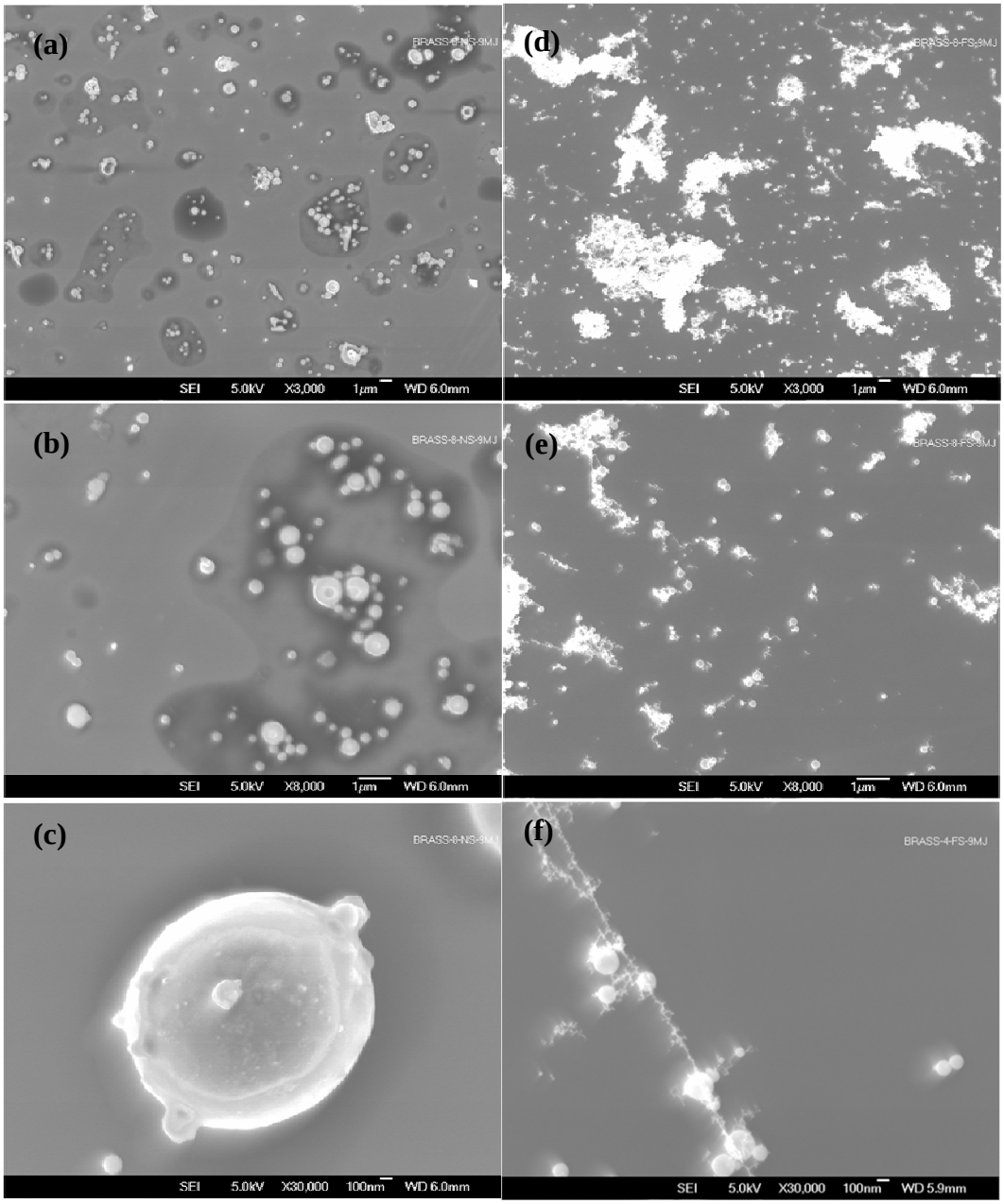

Figure 3.3 SEM images of the particles from laser ablation on brass alloy: (a) (b) (c) particles from ns laser ablation with different zoom ratio. (d) (e) (f) particles from fs laser ablation with different zoom ratio

Visual observation of the SEMs shows that nanosecond laser ablation produced more large spherical particles than the femtosecond case. However, calculated size distributions using computer software (Fig 3.4) of the SEM photos show similar behavior for both cases, and even predict a greater number of larger particles, because of the large agglomerates for femtosecond ablation. The irregular clusters are counted as single particles with an equivalent spherical diameter. This serves as an example that particle size measuring technologies must be carefully appraised, especially when single particle and agglomerates are similar in size.

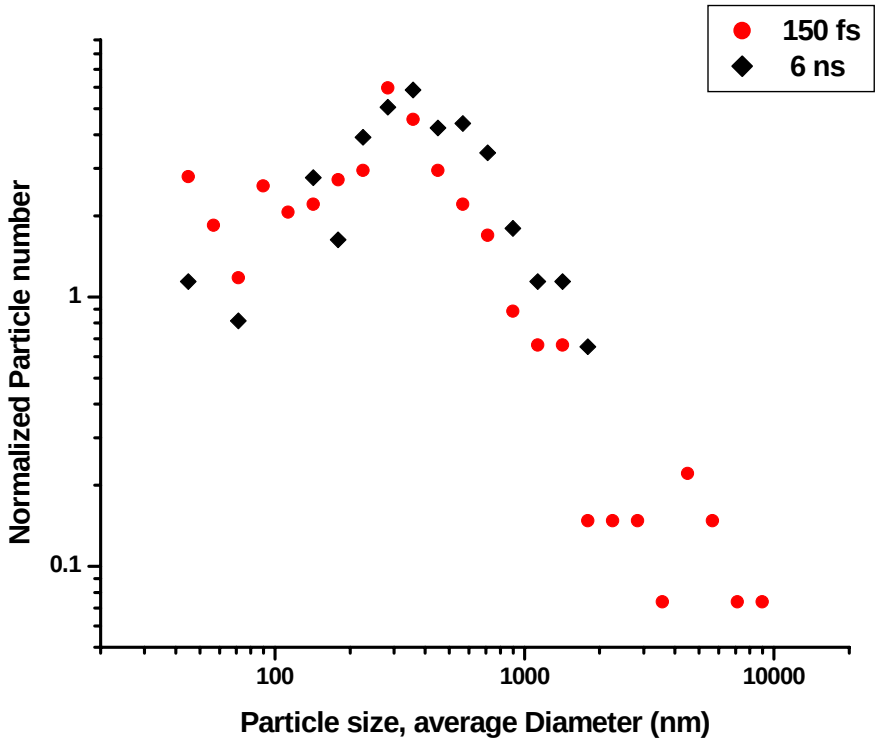

Figure 3.4 Particle size distribution measured from particles collected on surfaces using computer software

Laser induced plasmas were observed to be visibly different for each pulse duration. For equal fluence and spot size, the plasma from ns ablation was spherical by shaped while the fs plasma was long and narrow like a cylinder. Larger plasma for ns pulse could result in strong plasma reheating on the surface and more thermal interaction. The effects of short pulse-width could be found by comparing the craters. Fig 3.5 shows the crater volume for both fs and ns ablation under the same fluence. The long pulse-width ablation (ns) generated a significant raised rim around the crater, which is caused by resolidification of molten material. Evidence of the melting ejection during ns laser ablation is discussed in Chapter 4 through shadowgraph imaging. Splashing of the molten material was reduced using femtosecond pulses and no significant crater rim was observed. The crater volume (Figure 3.6) from femtosecond ablation was much larger and increased linearly with the number of pulses while the crater volume measured from the nanosecond was smaller and increased nonlinearly with the number of pulses.

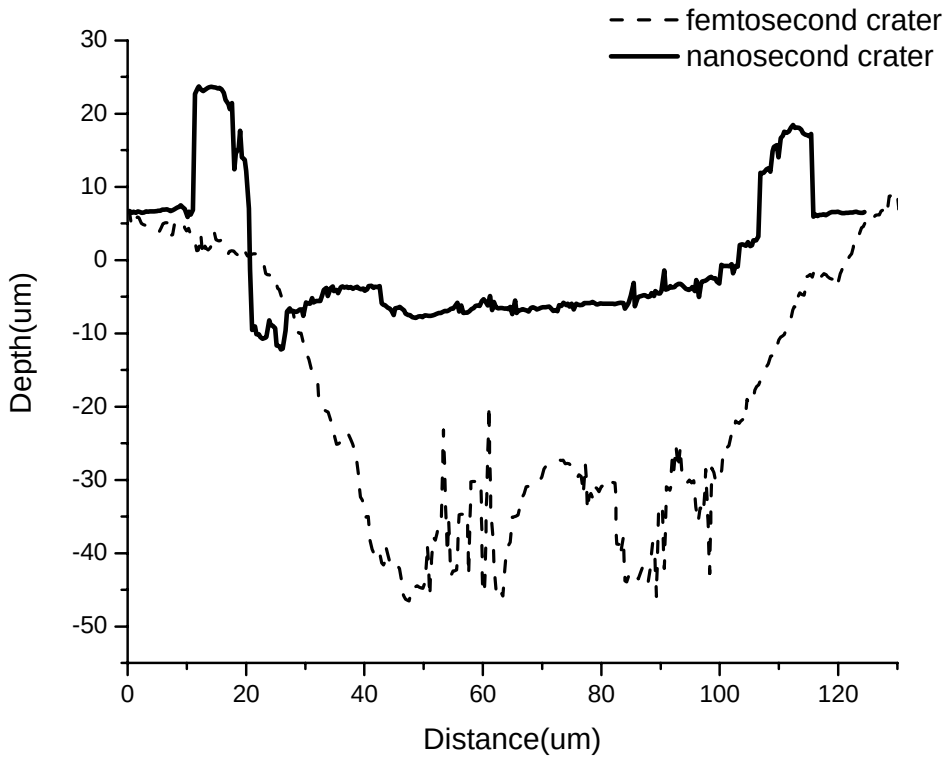

Figure 3.5 Crater shape of brass after fs and ns ablation

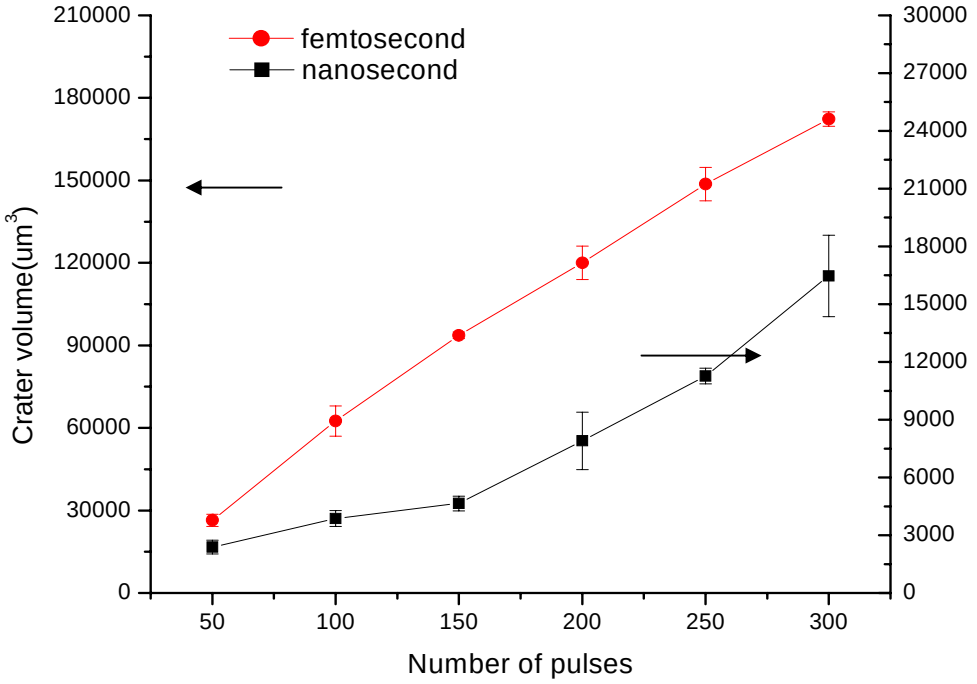

Figure 3.6 Crater volume of brass after fs and ns ablation

3.4 Variation of particle size distribution with laser parameters using a DMA

3.4.1 Introduction

The size distribution of particles generated in laser ablation is studied by using a DMA. Particles generated from ns and fs ablation have been collected and recorded by SEM images as described in previous section. The shape and the size of these particles can be directly observed using SEM images. The disadvantage of this type of measurement is that it's off line and particles need to be collected and moved to a microscope. Measuring the size using DMA offers the convenience of obtaining

the size distribution when laser ablation is performed. Therefore, it enables the systematic study of the effects of different laser parameters on particle size. However, one disadvantage of the DMA, as well as other on-line methods, is that they cannot discern the shape of the particles. Particle formed by the agglomerating of smaller aerosols could be of the same size as a single large particle. Deviations from the spherical shape would also result in an overestimation of the real physical size. Different laser parameters including pulse width, laser energy and gas flow rate were studied. Comparison of ns and fs laser ablation is discussed first and the results from the previous section are correlated with SEM images of the ablated particles to help understand the data measured by the DMA.

3.4.2 Experimental system

The experiment setup shown in Figure 3.7 includes two laser systems and the optical setup for the laser beams. Both lasers were operated at 266nm wavelength, including a Nd: YAG laser with 6 ns pulse duration (New Wave Research, Minilase II) and a Ti: sapphire laser with 150 fs pulse duration (Spectra-Physics, TSA 25). Different laser energy and operating conditions were applied to study the effects on particle size. Both laser beams were directed into the automatic X-Y-Z stage (NewWave Research, Merchantic) where the samples were placed. The ablation was performed at image focus position where the spot size was 60 microns for the nanosecond laser and 30 microns for the femtosecond laser. In the experiments comparing the two lasers, tests were carried out for different pulse

durations for the same laser energy and spot size. The ns spot size at imaging position was 60 microns; thus a pinhole was used to reduce it to the same diameter as fs spot size (30 microns).

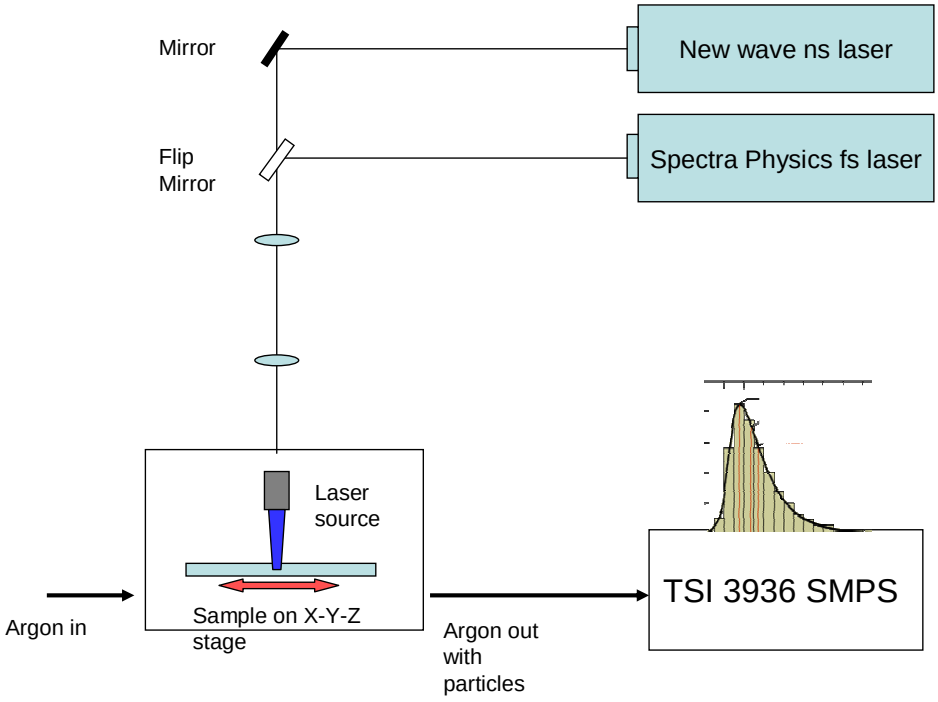

Figure 3.7 Experiment setup for particle measurement using SMPS

The laser ablation was processed in an argon environment under atmospheric pressure; the flow rate of the argon in the chamber was 1 L/min. The inert properties of argon prohibit reaction with the laser ablation products and preserve the properties of the particles. A SMPS (Scanning Mobility Particle system, TSI incorporated) 3936 series system was used for the particle size measurement. A flow switch was installed before the inlet to the SMPS to ensure the working flow rate for the SMPS (0.3 L/Min); the rest of the flow was discarded through a filter. Under normal working condition with air under atmospheric pressure, the system

can measure particle sizes from 10 nm to 850 nm using the differential mobility analyzer (DMA). Equation (3.7) shows that the particle size D selected by the DMA is proportional to the applied voltage V. However in argon, arcing discharges occurred at voltages lower than the designed value in air, and reduced the maximum measured particle size from 850 nm to ~400 nm. The particle measuring process requires a scanning time of at least 1 minute for each data acquisition. The size of laser-ablated particles may change with time as the crater is developed. To get a uniform particle generation during the measuring process, the samples were moving at a constant speed during laser ablation (10 $\mu m/\sec$ in most experiments) to eliminate the effects of changing crater shape on particle size. Different moving speeds of the samples were also applied to study this crater development effect. The effect of sample material on measured particle size is discussed in each independent section.

3.4.3 Pulse duration

Tests with different pulse duration were carried out using the same laser energy (0.12 mJ, which is the maximum energy that could be obtained from the fs UV laser) and spot size (30 microns) that corresponded to a fluence of 17 J/cm^2. The measured particle size distribution results from three materials are shown in Figure 3.8: for metals, like zinc and copper, the particle size was larger for femtosecond than for nanosecond laser ablation with a higher number density for the

femtosecond laser. For silicon the number density was also higher with the fs laser but the particle size was the same for fs and ns ablation.

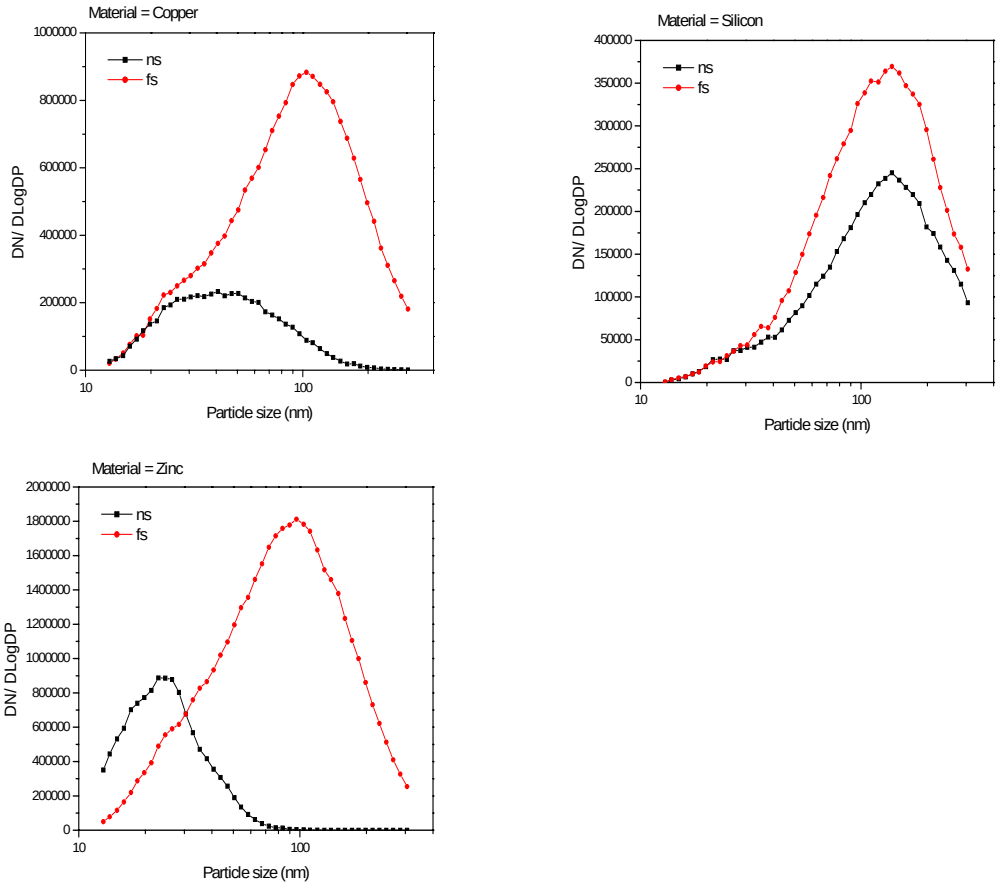

Figure 3.8 Particle size distributions for ns and fs pulses

The volume removed using the fs laser is larger than the ns laser in both metals (Figure 3.5 and 3.6) and in silicon [6,7], which is consistent with the higher particle number densities on the SEM images and the DMA measurements. For brass alloy (mostly copper), the ns laser generated spherical particles as large as micron-sized, while the fs laser generated large agglomerates. The big particles from the ns laser and the agglomerates from the fs laser are beyond the detection limit of the DMA

and were not measured. As discussed in the previous section, difference in ablation mechanisms for ns and fs laser existed. For metals, there was almost no raised rim around the crater for fs laser ablation while an obvious high raised rim existed for ns laser ablation. The ablation rate was constant with pulse number for fs ablation whereas it increased after several pulses for ns ablation (Figure 3.5). The increase of ablation rate for ns laser was attributed to the ejection of melt material after repetitive pulses, vaporization was dominant during fs laser ablation and yielded a constant ablation rate regardless of the crater development.

The maximum number density for ns ablation for zinc and copper occurred at ~ 30 and 50 nm, respectively. Since the particles generated by ejection from a melted region should be much larger; these particles in the size of several tens of nanometers should be formed by condensation. More material was vaporized by the fs laser pulse and then condensate to small liquid aerosols. The aerosols with high number density are more likely to collide with each other and form new particles or agglomerates as compared to aerosols formed in ns laser ablation. If the particles collided after they were solidified, they then form irregular shaped (web or chain-like) agglomerates. When the particles collided in the liquid state, they then tended to coalesce into a larger droplet. As the plasma and particles cooled, the material with the higher melting point resolidified faster than material with a lower melting point. Therefore, aerosols formed from low melting materials can remain in liquid form longer and have a higher probability to coalesce with each other. The melting

point of zinc (693 K) is much lower than copper (1356 K) and silicon (1685 K), coalescence could be frequent in zinc ablation.

Figure 3.9 shows the SEM images of collected zinc particles using both ns and fs laser pulses. More particles can be found in fs ablation than in ns ablation. Though the particles in fs ablation are as large as several hundreds nanometers, they were not formed by melt ejection from the surface. These particles several hundreds nanometers in size could be the coalesced product of smaller particles. The DMA measured the size for zinc which shows an increase from ~30 nm using ns pulse to ~100 nm using fs pulse and the number density almost doubled. These results could be explained by the much higher ablation rate using the fs pulse. Figure 3.6 shows that the volume removed using fs pulse was more than 15 times (more than 4 times for depth) than using ns pulse. Melt ejection is important in ns ablation, and the size of the melt ejection particles was large. The much higher ablation efficiency means much more vaporized material was generated using fs ablation.

Unlike zinc, the number density in silicon increased only 60%, and the size was similar comparing results of ns and fs ablation. Zeng [8] reported that ablation depth increased less than 100% using fs than ns ablation, which is much less than the case of metal. Degree of increased ablation efficiency of fs pulse over ns pulse depends on sample material and also influenced the increase of the measured particle size.

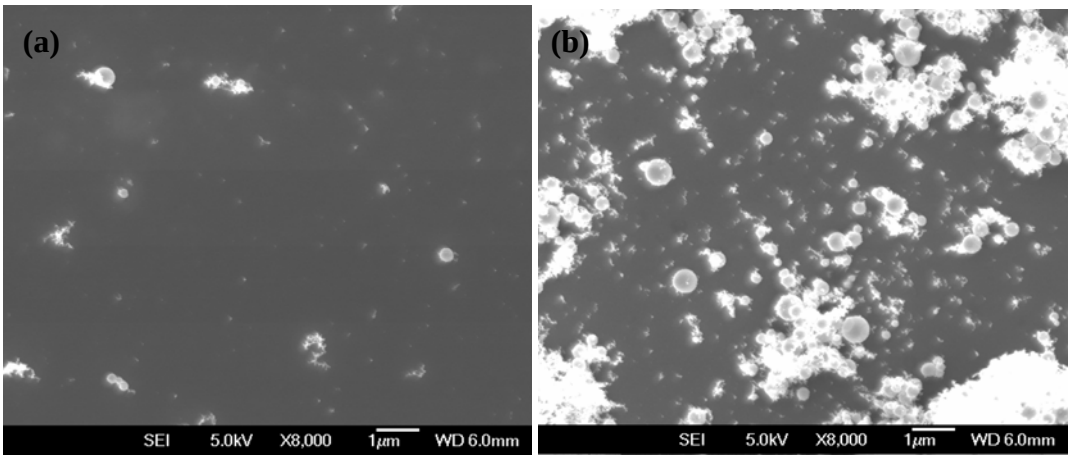

Figure 3.9 SEM images of laser ablation on zinc (a) nanosecond (b) femtosecond

3.4.4 Laser energy

The effect of ns laser fluence on particle size was studied using graphite, silicon, zinc, copper and brass samples. Figure 3.10 shows the measured particle size distribution at different laser fluence for zinc and graphite. The particle size distribution changes with the laser fluence. The number density increased monotonically with respect to the energy for all of the samples. The variation of particle diameter with laser energy was studied by utilizing the median diameter that was obtained from the data and is shown in Figure 3.11. The median diameter is defined as the particle diameter that divides the frequency distribution in half, 50% of the particles are larger and 50% of them are smaller. Figure 3.11 show that the metal particles were smaller than for graphite and silicon; the median metal particle size decreased with increasing laser energy, while the median particle diameter did notchange much for graphite and silicon. The median diameter decreased from 110 to 45 nm at $10\,J/cm^2$ for zinc, and from 100 to 70 nm at

$15\,J/cm^2$ for copper; for both metals the median diameter did notchange as laser fluence further increased above 10 and $15\,J/cm^2$, respectively. For silicon, the median diameter gradually decreased from 130 to 110 nm as laser fluence increased, while the size did not vary with energy for graphite.

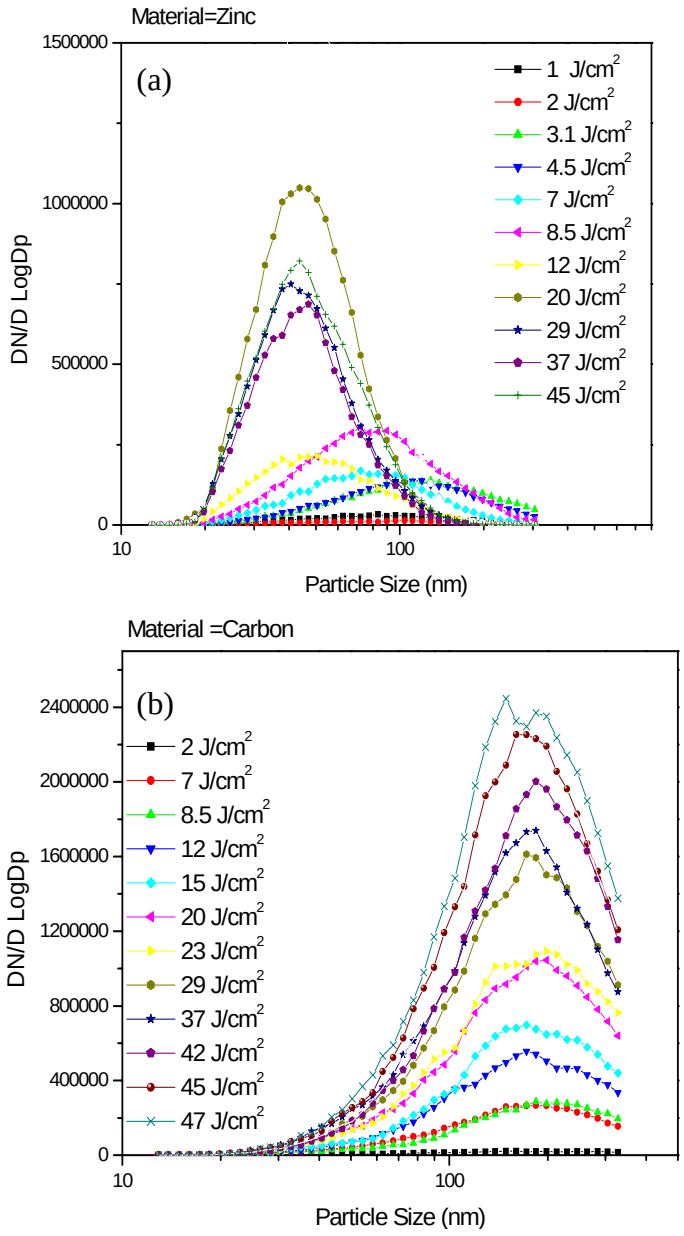

Figure 3.10 Particle size distribution of zinc measured by DMA (a) Zinc (b) graphite

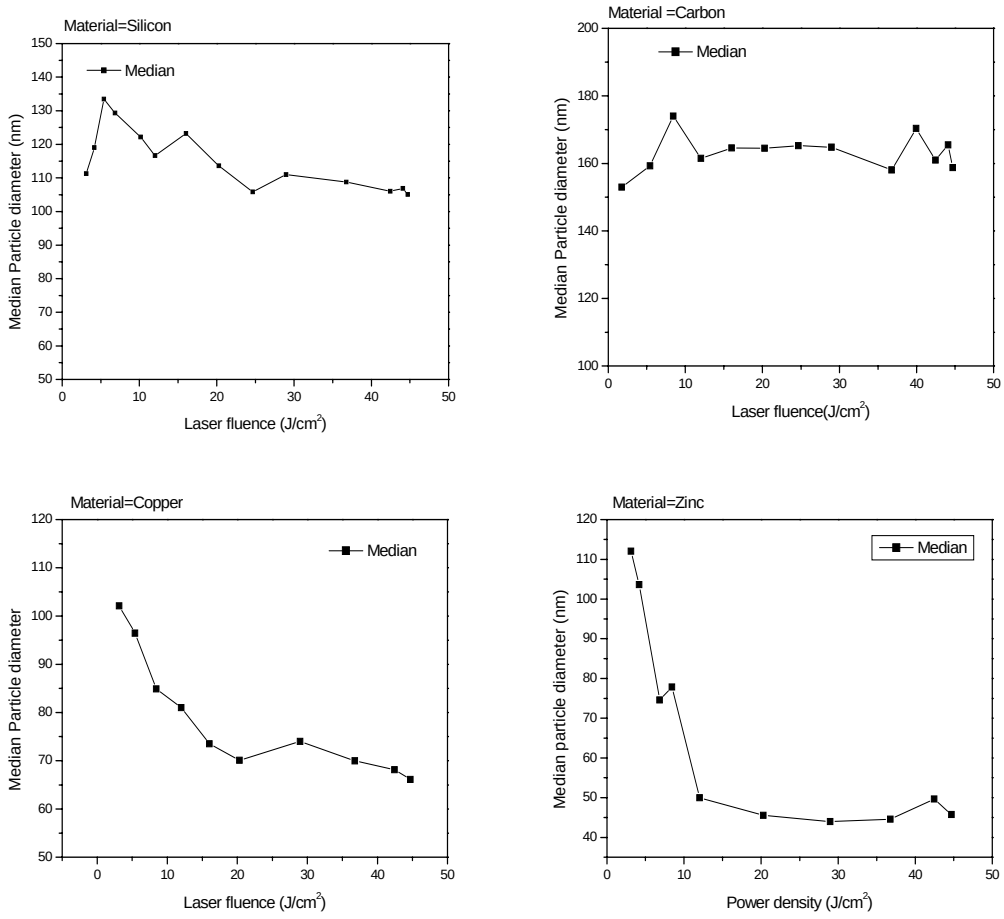

Figure 3.11 Measured median particle diameter with respect to laser fluence

It is not clear why the median particle size becomes smaller for metals as the laser fluence increases up to a certain value; note that the number concentration was increasing. The crater volume increased with the laser fluence and the SEM images (Figure 3.12) showed more particles at higher fluence. If the observed particles were formed by condensation, larger particles should be formed as more vaporized material was produced. Higher laser fluence caused higher plasma temperatures and slower cooling of the ambient gas which delays the onset time of condensation.

The vapor plume also expands faster at higher laser fluence. The number density of the atoms is therefore even lower at high laser fluence than at low laser fluence due to a much larger cooling vapor plume. These reasons contribute to more particles but of smaller size formed at higher laser fluence. The median diameter in zinc decreased dramatically from 110 to 40 nm, while the median diameter of copper and silicon only showed a small change and the median diameter of graphite is almost unchanged with varying laser fluence. The different trends could be related to the shape or configuration of the particles. As discussed previously, zinc vapor usually forms particles without voids and has the least tendency to form irregular shape agglomerates. This could result from its lower melting point so that liquid droplets collide and form new entities. For other materials, for example, carbon, the particles are mainly in agglomerate form; therefore increased laser fluence results in a larger number density but does not change the size distribution.

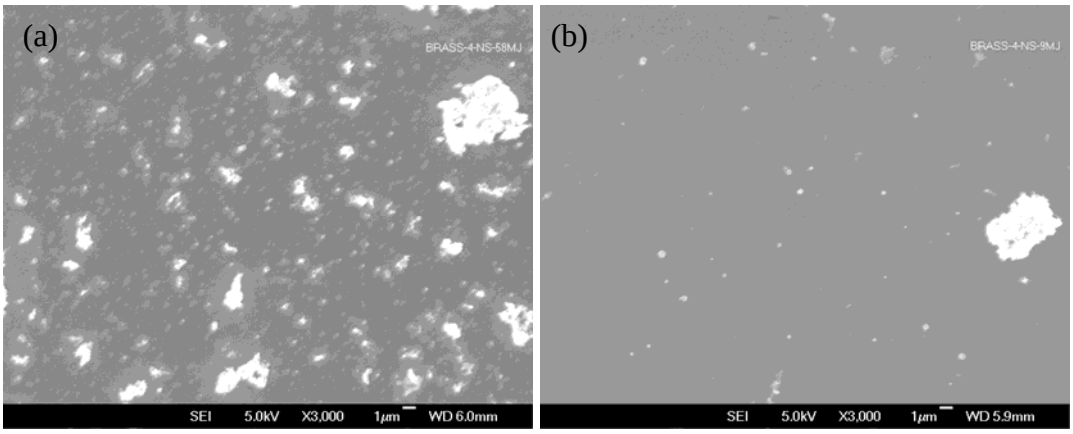

Figure 3.12 SEM images of laser ablation particles of brass alloy (a) 45 J/cm^2 (b) 8 J/cm^2

3.4.5 Flowrate

By comparing the size distribution of the particles with different argon flow rate, information of how the particles agglomerate or coagulate could be obtained. Three different flow rates were chosen to flow through the ablation chamber: 0.5, 0.75 and 1.5L/min. The laser fluence was fixed at $20\,J/cm^2$. A flow switch was installed to allow only 0.3 L/min flow into the SMPS. The number density for each flow rate was normalized by the portion of the total flow used in the measurement. The results of the three flow rate with different samples are demonstrated in Figure 3.13. The particle size distributions are almost the same for zinc for all flow rates; since the higher flow rate has higher transport efficiency the number density is therefore higher. For copper and silicon, the measured particles grew larger with a much lower number density at the slower flow rate. The median size of copper increased from 50 to 100 nm as flow rate decreased, while the median size of silicon was undetermined (more than 400 nm).

The distance from the ablation chamber to the inlet of SMPS was 1.5m, and the time the aerosols stayed in the tube was 5, 3.33 and 1.67 sec, respectively. It has been reported that zinc vapor condenses quickly into particles and does not form agglomerates [9,10]; it was assumed the particle size distribution of zinc was determined before the particles were transported into the SMPS and therefore did not change with the flow rate. For copper and silicon, the size distribution continued to change as the particles stayed in the tube. The temperature of the gas ambient and the particles was already at room temperature at this time; therefore particles should already be solidified and could not coagulate into single particles

but instead formed agglomerates from collisions with smaller particles. The measured size of the particles is therefore larger for slower flow rate. To avoid or reduce this kind of agglomerate formation, higher flow rate should be used when using the SMPS to measure particles.

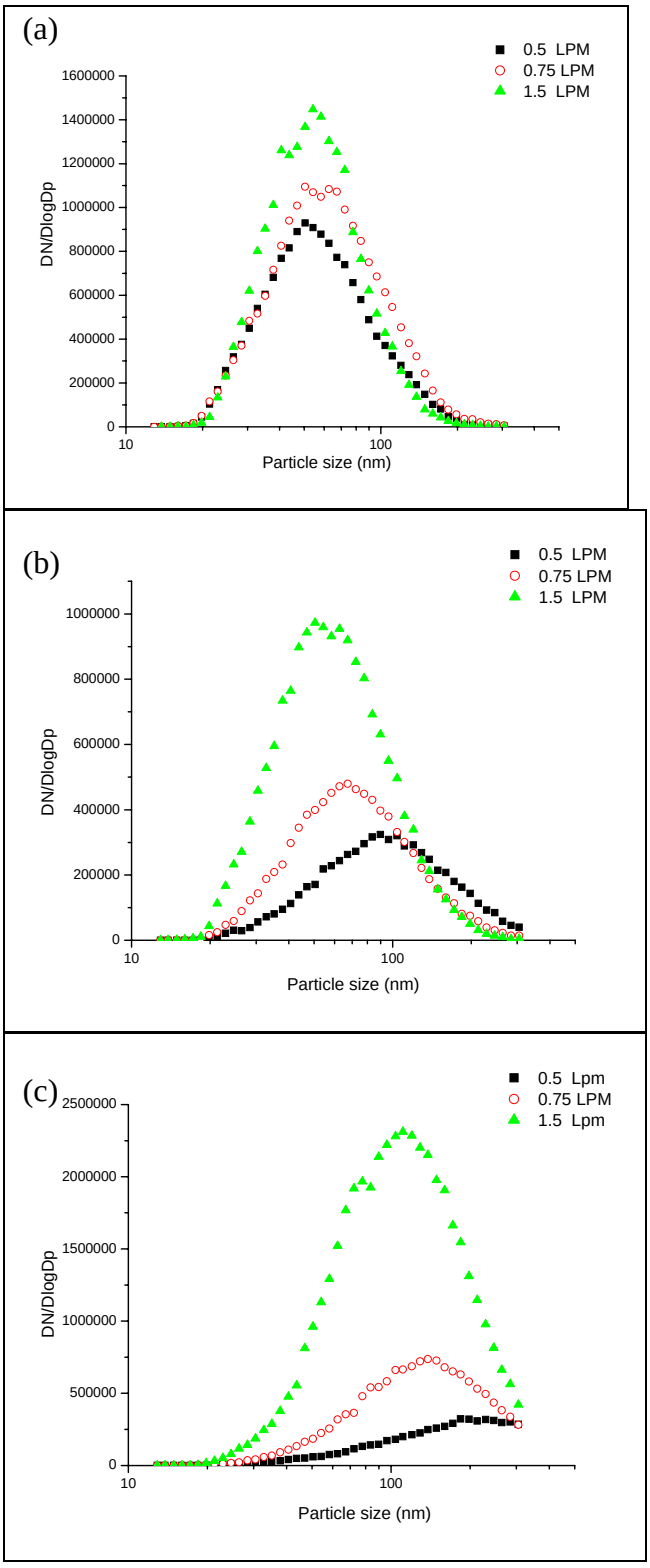

Figure 3.13 Particle size measurements at different flowrate for (a) zinc (b) copper (c) silicon

3.4.6 Laser scanning speed

As described previously, the lasers were operating in scanning mode to generate uniform particle size distribution during the SMPS sampling time. The sample on the X-Y-Z stage was moving with constant speed (10 microns per second) horizontally for all previous experiments. However, different scanning speeds could result in different crater development processes and temperature distribution in the samples. These effects were studied by varying the scanning speed from 0.1 to 200 μm/sec with different samples. Results obtained using the slower speed should approach the results using single hole ablation; that is, influence from crater development and more of the sample volume being affected from heating by the previous laser pulse (and for the faster scanning speed the effect resulting from the previous laser pulse is less).

The experiment was performed at a fixed laser fluence $20\,J/cm^2$ and a 10 Hz repetition rate with the results shown in Figure 3.14. A strong relationship between the scanning speed and the particle size distribution was observed. The median particle diameter increased with scanning speed at slower moving speeds (<3 micron/sec) and then dropped sharply when the scanning speed was in the range 5-10 micron/sec.

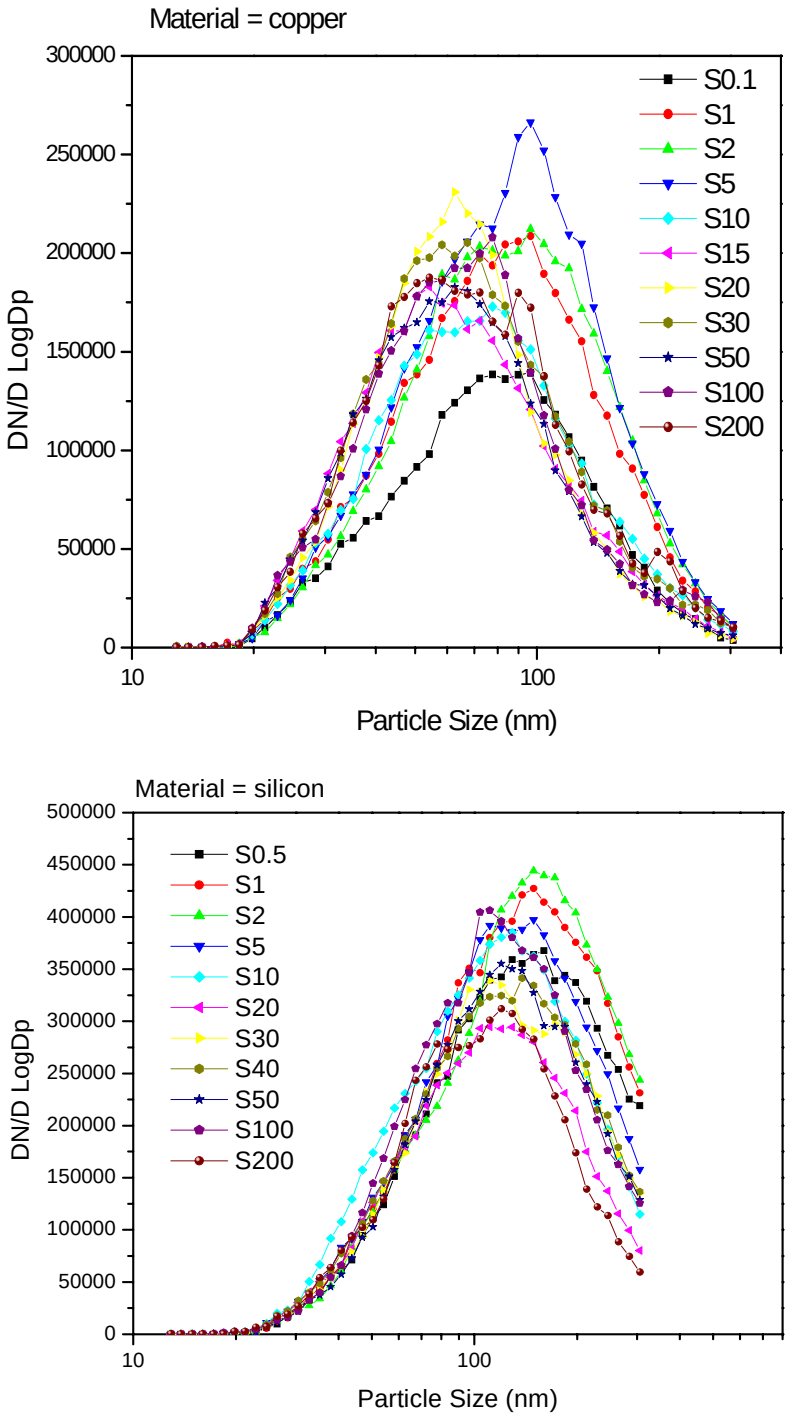

Figure 3.14 (a) Measured particle distribution for copper and silicon with different scanning rate

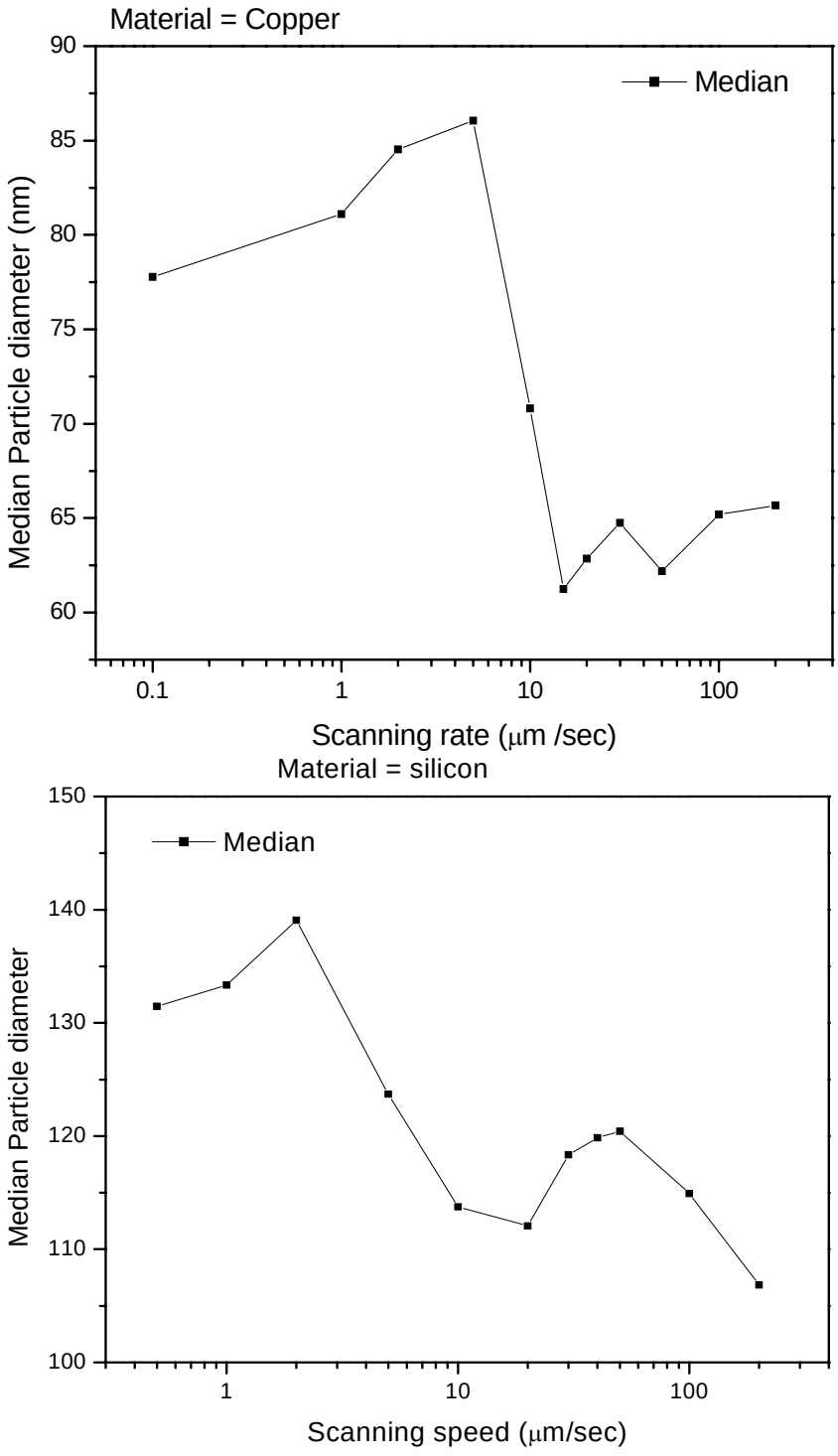

Figure 3.14 (b) Measured median diameters for copper and silicon with different scanning rate

Two competing mechanisms could be involved in the ablation; namely the crater development during the laser ablation and heating effects from preceding pulses. The nature of the Gaussian shape of the pulse results in a crater with a shape close to a inverted triangle. The amount of material removed is therefore smaller if the continuing pulse is irradiated on the already formed crater and smaller condensation particles are formed. Moving the laser spot to a fresh (flat) surface increases the amount of vaporized atoms and results in larger particles. On the other hand, multiple laser pulses can cause accumulated heat in the sample, which is not completed conducted away. The resulting higher temperature distribution in the sample enhances the evaporation rate and generates larger particles. When the scanning speed is fast, the heating effects dwindle and decrease the sample temperature and evaporation rate; therefore smaller particles are formed. The change of particle size with respect to scanning speed is therefore a combination of these two effects.

To separate the heating effect from the effect of the scanning speed on crater development, another experimental condition was used. Rather than the regular scanning method, which moved the silicon sample with constant speed, the sample was stationary for 10 repetitive pulses and then moved to another fresh surface. The experiment was accomplished using a built in motor stage, which could move the sample to a new position before next set of laser pulses irradiate the surface. The crater formed in 10 pulses was much less than that results from a stationary target and can be neglected. Three different distances between the spots were used: 50,

100 and 250 microns. The laser spot size was 60 micron, so part of the laser spot was overlapped for the 50-micron spacing, and was completely separated at the 250-micron spacing. Figure 3.15 shows that more particles were generated when the spacing is smaller and fewer particles when the spacing is larger. This observation proved that the heating effects could notbe neglected during repetitive (e.g. 10 repetitive pulses) laser ablation.

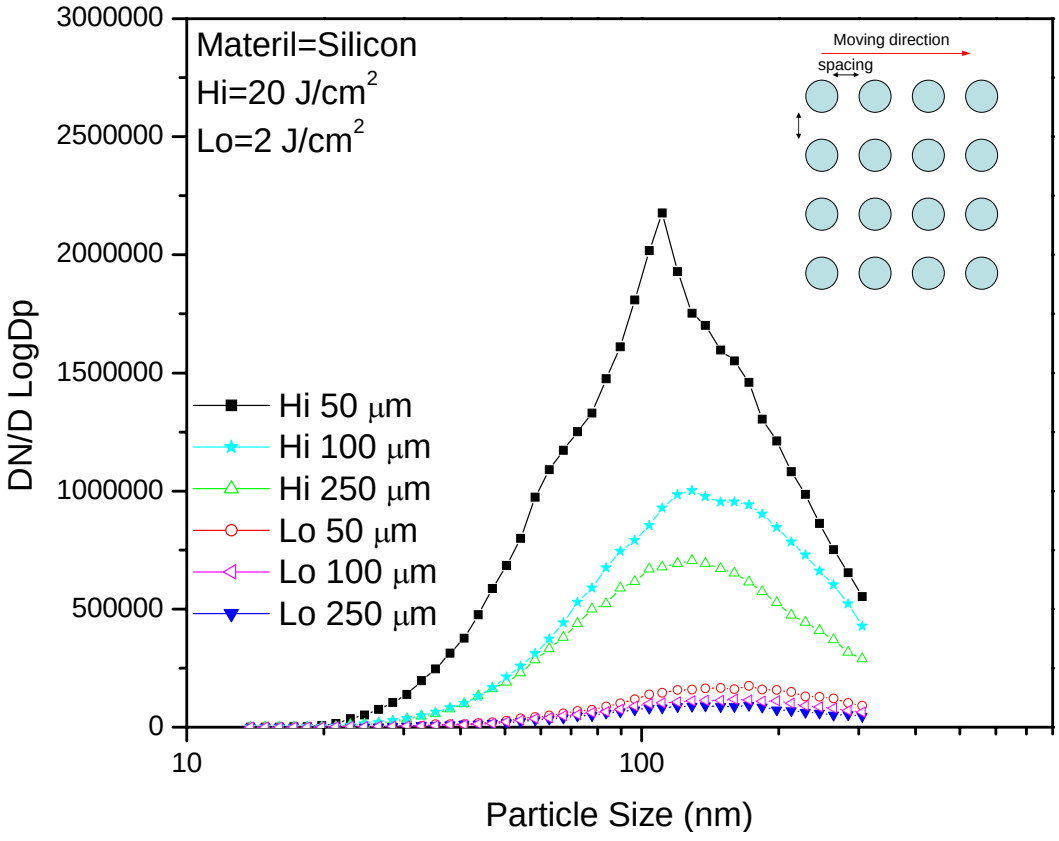

Figure 3.15 Measured particle number distribution with different distance between sets of ablation spots from ablation on silicon

3.4.7 Summary

Effects of selected laser parameters on particle size distribution that were generated during laser ablation were studied using a DMA. It was found that the laser parameters could significantly affect the results. Laser pulse duration and laser fluence both influence the condensation rate and number density; at the same time agglomeration and coagulation shift the measured particle to larger sizes. The particle formation process is also highly dependent on the sample properties. Experimental conditions like gas flow rate and scanning speed also affects the result and obtaining optimal experimental parameters to achieve a desired particle size can be a very daunting task.

References

1. Y. S. Cheng and H. C. Yeh, "Theory of A Screen-Type Diffusion Battery," Journal of Aerosol Science 11, 313-& (1980)

2. H. C. van de Hulst, *Light scattering by small particles*, (Dover Publications, New York, 1981).

3. A. Wiedensohler, "An Approximation of the Bipolar Charge-Distribution for Particles in the Sub-Micron Size Range," Journal of Aerosol Science 19, 387-389 (1988)

4. E. O. Knutson and K. T. Whitby, "Aerosol classification by electric mobility: apparatus theory and applications," J. Aerosol Sci 6, 443 (1975)

5. M. R. Stoltzenburg, "An ultrafine aerosol size distribution measuring system," Ph.D. Thesis (University of Minnisota, 1988).

6. C. Liu, X. L. Mao, S. S. Mao, X. Zeng, R. Greif, and R. E. Russo, "Nanosecond and ferntosecond laser ablation of brass: Particulate and ICPMS measurements," Analytical Chemistry 76, 379-383 (2004)

7. X. Zeng, X. L. Mao, R. Greif, and R. E. Russo, "Experimental investigation of ablation efficiency and plasma expansion during femtosecond and nanosecond laser ablation of silicon," Applied Physics A-Materials Science & Processing 80, 237-241 (2005)

8. X. Zeng, X. L. Mao, R. Greif, and R. E. Russo, "Experimental investigation of ablation efficiency and plasma expansion during femtosecond and nanosecond laser ablation of silicon," Applied Physics A-Materials Science & Processing 80, 237-241 (2005)

9. B. P. Michael, J. A. Nuth, L. U. Lilleleht, E. Bussoletti, L. Colangeli, and P. Palumbo, "A nucleation experiment in low gravity conditions: Monitoring and collection of Mg and Zn particles," Gravitational Effects in Materials and Fluid Sciences 24, 1273-1277 (1999)

10. B. P. Michael, J. A. Nuth, and L. U. Lilleleht, "Zinc crystal growth in microgravity," Astrophysical Journal 590, 579-585 (2003)

Chapter Four

Shadowgraph Images of Laser Ablation Particles: Proof of Internal Shockwave and its Relation to Particle Ejection

4.1 Experiment system and theoretical background

4.1.1 Experimental

The laser ablation system included two lasers: a Nd: Yag (266 nm wavelength with 4 ns pulse duration, New Wave Research, Tempest 10) laser and an imaging Ti: sapphire (800 nm wavelength with 150 fs pulse duration, Spectral-Physics). The shadowgraph imaging experimental system is shown in Figure 4.1; a CCD camera (Photometrics model CH 250/A) with resolution 1317×1035 pixels was used to record the shadowgraph image from the fs laser pulse, the probe laser beam was aligned parallel to the sample surface and perpendicular to the ablation beam. The two lasers were fired with a controlled time difference via a delay generator (Stanford DSG 535). Time triggering error existed during the experiment; the real time delay between the pulses was monitored using two photodiode detectors placed close to the sample, and the signals were read using an oscillator. The ns laser pulse was focused to ~ 50-micron spot on the sample surface using a lens. The sample was at atmospheric pressure air; different laser fluence was applied by controlling the laser energy output while four different samples were

used: silicon, copper, zinc and tungsten. Each shadowgraph image was taken with a fresh sample surface when ablation occurred.

The volumes and depths of the laser-ablated craters were measured using a white-light interferometric microscope (New View 200, Zygo). The crater volume was defined as the volume below a reference surface minus the volume above the reference surface, where the reference surface was the unablated fresh sample surface.

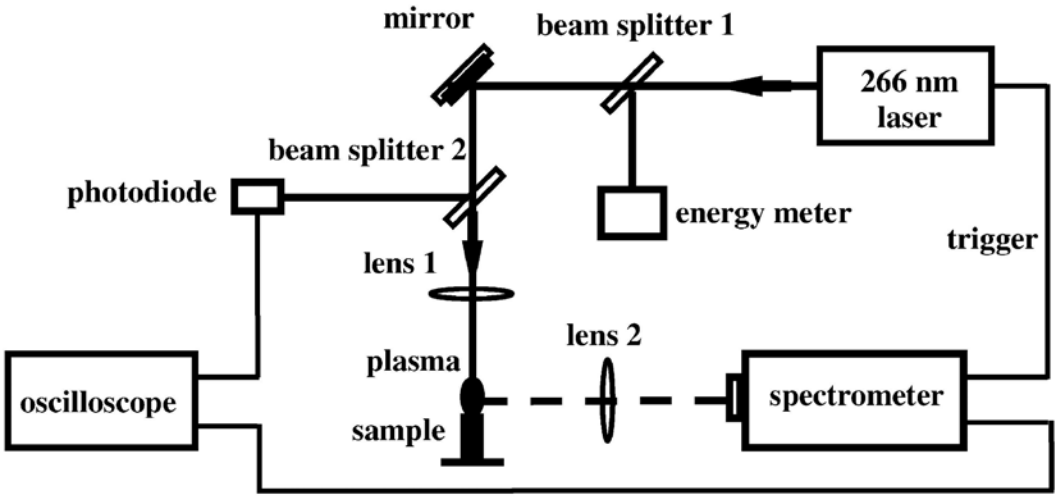

Figure 4.1 Experiment setup for shadowgraph imaging

4.1.2 Shockwave propagation

As discussed in the previous chapter, the shockwave is formed as the vapor plume expands and compresses the ambient air. The shockwave propagates and the time-resolved images demonstrated the propagation of the shockwaves generated during the laser ablation. Two frames of the time-resolved image at 20 and 100 ns are shown in Figure 4.2. Each image size is 550 microns in length corresponding to

1317 pixels. Thus by measuring the distance from the shockwave front to the sample surface for each delay time, the relation of shockwave distance with respect to time can be obtained as shown in Figure 4.3.

The speed of shockwave is mostly determined by the laser energy; higher laser energy induces a faster shockwave and the range of the shockwave image was limited by the CCD size. Many researchers have studied the distance-time relation of the shockwaves and it was proposed that the shockwave motion could be described by the Sedov theory using laser energy, gas density and propagation time [1]. From the Sedov theory, it is described that for a sudden point energy release source, the blast wave would travel in space (three-dimension, n=3) following a power law ($R \sim t^{0.4}$). Figure 4.3 shows the shockwave position from ablation of copper at different energies. The propagation of the shockwave mostly follows the $R \sim t^{0.4}$ relation except for the earlier time before 10-20 ns regardless of the energy. As seen in Figure 4.3, the propagate speed of the shockwave is much faster in the beginning and then slows down to the $R \sim t^{0.4}$ relation.

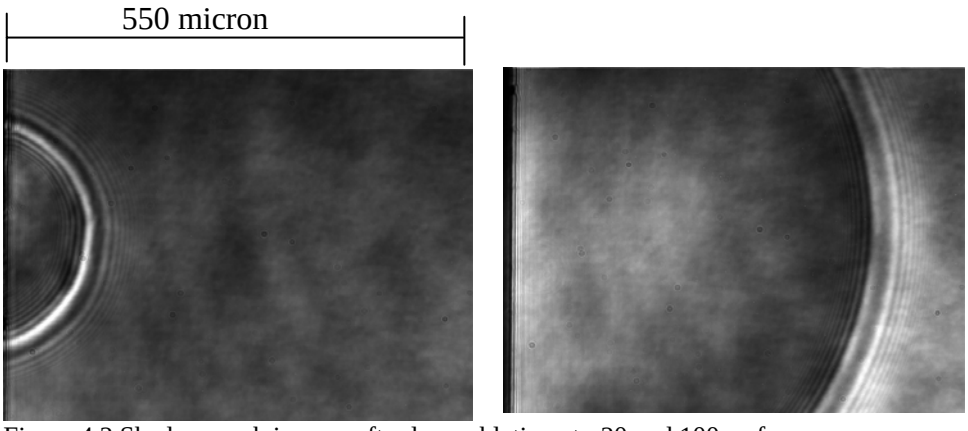

Figure 4.2 Shadowgraph images after laser ablation at ~20 and 100 ns for copper

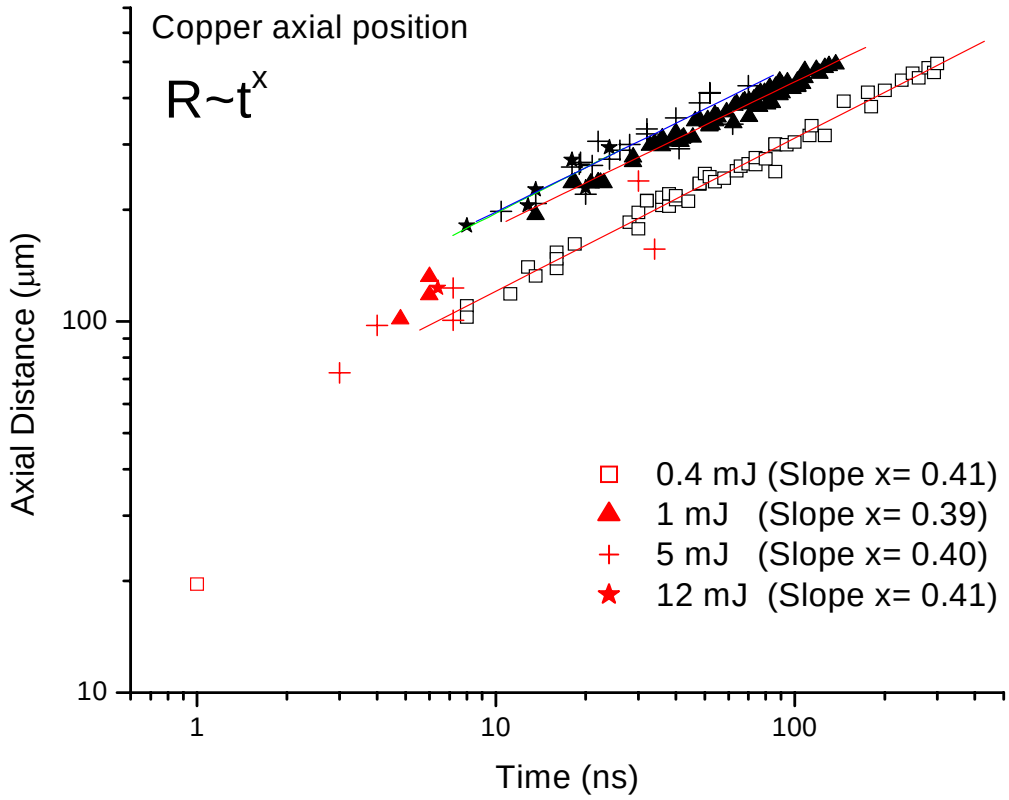

Figure 4.3 Shockwave front positions with respect to time for copper

Although the Sedov theory provides an explanation and good agreement with the experimental results, one fundamental difference does not match the early stage of the shockwave propagation. Sedov theory is based on the idealized assumption that energy is released at a point and then the shockwave propagates from the point. However, in the present application the shockwave is formed by the compression of the expanding vapor plume of finite volume on ambient air.

4.1.3 Theoretical background of shockwaves

To describe the vapor plume propagation right after the laser ablation and the shockwave formation and propagation, the Sedov theory is modified. Several studies have been made to determine the plasma expansion in ambient gas [2-4]. Recently, Arnold [2] used an analytical model considering the vapor plume based on a spherically symmetric expansion. His model involves the calculation of the shockwave positions. The expansion can be described by ordinary differential equations for the characteristic radial location (contact surface, which is the interface between the vapor plume and ambient gas, and the positions of the shockwaves) According to his model, in the initial stage, the expansion is similar to a free expansion into vacuum, with the radius of the vapor plume R~ t. Later the initial expansion slows because of the resistance of ambient gas and propagates according to the Sedov-theory R~ $t^{0.4}$. Later the vapor plume stops and ceases moving and even begins to contract. The governing equations are presented in Arnold's paper [2]. Several of the equations will be listed in the following paragraphs.

The model of Arnold [2] was based on gas dynamics and made several assumptions including neglecting Knudsen layer effects. The contact boundary is treated as impenetrable; thus mixing between the plume and the ambient gas is not considered. The spherically symmetric expansion was assumed and the model did not consider the initial stage before the plume expands to the laser spot size R_0. When the laser pulse terminates, the size of the vapor plume formed by the evaporated material is assumed to be of the size of the laser spot. The starting mass

density of the plume ρ_0 can be calculated as $\rho_0 = 3M/(2\pi R_0^3)$, where M is the evaporated target mass obtained from the experiment. Experimental values of mass M and laser energy E were used in the calculation [2].

The plume expands as a supersonic piston during the early stage; and can be approximated as a free expansion because the ambient gas is not yet affected by the shockwave. The external shockwave is formed as ambient air is compressed and heated; at the same time the air mass decelerates the expansion of the vapor plume. As the plume expands further, the pressure exerted by the compressed ambient gas increases and then the contact surface slows down while the external shockwave continues to propagate forward.

In the initial stage, the thermal energy E_t is much less than the kinetic energy E_k, and the energy conservation can be obtained from gas dynamic relations [5,6]:

$$E_k + E_t = E\frac{3}{4k+10} = M\dot{R}^2 + E\left(\frac{R_0}{R}\right)^{3(\gamma_p - 1)} \approx M\dot{R}^2 \tag{4.1}$$

and the initial plume expansion velocity is found:

$$\dot{R} \equiv v_f = \sqrt{\frac{4k+10}{3}\frac{E}{M}} \tag{4.2}$$

The plume density and pressure can be expressed as:

$$\rho_p = \frac{\Gamma(k+5/2)}{\pi^{3/2}\Gamma(k+1)}\frac{M}{R^3}\left(1-\left(\frac{r}{R}\right)^2\right)^k \tag{4.3}$$

$$p_p = (\gamma_p - 1)\frac{\Gamma(k+7/2)}{\pi^{3/2}\Gamma(k+7/2)}\frac{E}{{R_0}^3}\left(\frac{R_0}{R}\right)^{3\gamma_p}\left(1-\left(\frac{r}{R}\right)^2\right)^{k+1} \tag{4.4}$$

where k is the value of $\frac{1}{\gamma_p - 1}$, γ is the ratio of specific heat, and Γ is gamma function.

The easily observed shockwave as in Figure 4.2 is the external shockwave, whereas another shockwave called the internal shockwave is also present simultaneously. In the initial stage of the vapor plume expansion, the position of the shockwaves and contact surface are the same. The expansion is slower than in vacuum, the plume performs work on the ambient gas resulting in higher temperatures than in vacuum. Arnold et al noted that the heating starts near the contact surface, where the molecules of the vapor plume collide with the ambient gas molecules and some are reflected backward and form the internal shockwave. The internal shockwave first moves together with the expanding vapor plume and the external shockwave and then later starts to propagate inwards. This concept that the internal shockwave was formed by the backscattered material was first proposed by Anisimov [7]. The existence of ambient gas results in the formation of an internal shockwave together with the deceleration of the plume. As the plume gradually slows, the internal shockwave simultaneously travels back to the sample surface. The internal shockwave travels between the sample surface and the contact surface several times and eventually the properties of the plume become uniform. However, in Arnolds' simplified model, the internal shockwave is assumed to strike the sample surface only once and soon afterwards, starts to travel outwards

reflected. As will be discussed in the next section, this simplification should be modified to include the effects of the multiple internal shockwaves observed in the experiment. Figure 4.4 sketches the concept of the spherical plume structure, which evolves after laser ablation. Re, Ri, and Rc are the position of the external shockwave, internal shockwave and contact surface, respectively. The ambient air not affected by the shockwave is the region with subscript g. As the external shockwave propagates, the ambient gas compressed by the expanding plume forms the region SWe; the properties are denoted by subscript e. The plume material which is reflected from the contact surface forms SWi, and the properties in this region are denoted by subscript i. Finally, the central portion of the plume not affected by the internal shockwave travels, is unaffected by the ambient gas; this region is denoted with subscript p.

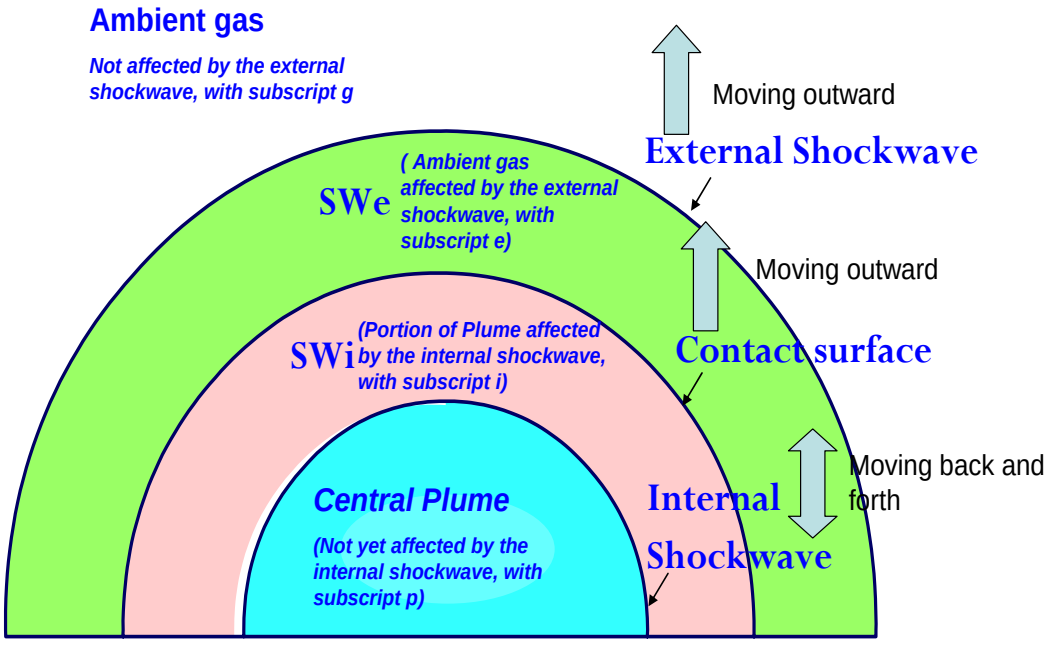

Figure 4.4 Structure of vapor plume and shockwaves

The mass conservation in the SWe region is written:

$$M_e = \frac{4\pi}{3}\left(R_e^{\,3} - R_c^{\,3}\right)\rho_e = \frac{4\pi}{3} R_e^{\,3}\rho_g \tag{4.5}$$

with the density ρ_e obtained from gas dynamic relations. The differential equation for the external shockwave position R_e is given by [2]:

$$\dot{R}_e = c_g\left(1 - \frac{\gamma_g + 1}{2}\left(\frac{R_C}{R_e}\right)^3\right)^{-1/2} \tag{4.6a}$$

where c_g is the sound speed, and the gas velocity at the shockwave front is

$$v_{\mathrm{Re}} = \dot{R}_e\left(\frac{R_c}{R_e}\right)^3 \tag{4.6b}$$

The central part of the plume is unaffected by the ambient gas. The mass contained within this part of the plume can be expressed as:

$$\begin{aligned} M_p &= \int_0^{R_i} \rho_p 4\pi r^2 dr = \int_0^{R_i} \frac{\Gamma(k+5/2)}{\pi^{3/2}\Gamma(k+1)}\frac{M}{R^3}\left(1-\left(\frac{r}{R}\right)^2\right)^k 4\pi r^2 dr \\ &= \frac{4\Gamma(k+5/2)}{\pi^{3/2}\Gamma(k+1)} M \int_0^{R_i} \frac{1}{R^3}\left(1-\left(\frac{r}{R}\right)^2\right)^k r^2 dr \end{aligned} \tag{4.7}$$

where Γ is gamma function, k is the value of $\dfrac{1}{\gamma_p - 1}$, γ is the ratio of specific heat, and the radius R appeared in equation (4.7) is the radius of the free expansion plume described in equations (4.1) to (4,4).

In the SWi region, the mass is given by:

$$\begin{aligned} M_i &= \frac{4\pi}{3}\left(R_c^{\,3} - R_i^{\,3}\right)\rho_i = \frac{4\pi}{3}\left(R_c^{\,3} - R_i^{\,3}\right)\frac{\gamma_p + 1}{\gamma_p - 1}\rho_p(R_i) \\ &= \frac{4}{3}\frac{\left(R_c^{\,3} - R_i^{\,3}\right)}{R^3}\frac{\gamma_p + 1}{\gamma_p - 1}\frac{\Gamma(k+5/2)}{\pi^{1/2}\Gamma(k+1)} M\left(1-\left(\frac{R_i}{R}\right)^2\right)^k \end{aligned} \tag{4.8}$$

From equations (4.7) and (4.8), the mass conservation in the plume is found from the relation $M_i + M_p = M$:

$$M = \frac{4\Gamma(k+5/2)}{\pi^{3/2}\Gamma(k+1)} M \int_0^{R_c} \frac{1}{R^3}\left(1-\left(\frac{r}{R}\right)^2\right)^k r^2 dr + \frac{4}{3}\frac{\left(R_c{}^3 - R_i{}^3\right)}{R^3}\frac{\gamma_p+1}{\gamma_p-1}\times$$
$$\frac{\Gamma(k+5/2)}{\pi^{1/2}\Gamma(k+1)} M\left(1-\left(\frac{R_i}{R}\right)^2\right)^k \qquad (4.9)$$

Finally, we need to invoke the overall energy conservation:

$$E_{pk} + E_{pt} + E_{ik} + E_{it} + E_{ek} + E_{et} = E \qquad (4.10)$$

where the subscript k represents the kinetic energy and t represents the thermal energy; and subscript p, i, e represent the energy contained in the region of central plasma, SWi and SWe, respectively.

Equation (4.10) is presented in Arnold et al [2]. Solving equations (4.5), (4.6), (4.9) and (4.10) simultaneously, Arnold et al obtain the position of the shockwaves and contact surface: R_e, R_i and R_c. The initial conditions are:

$$R_i(0) \approx R_c(0) \approx R_e(0) \approx R(0) \approx R_0$$
$$\dot{R}_c(0) \approx \dot{R}_e(0) = v_f = \sqrt{\frac{4k+10}{3}\frac{E}{M}} \qquad (4.11)$$

For the case of air, the value of k equals 3/2, γ=5/3.

Although the existence of internal shockwave is essential to the plume expansion model, the internal shockwave is seldom presented in the literature. The shadowgraph taken in this experiment provides clear evidence for the internal shockwaves, which will be discussed in more detail in 4.3. Theoretical predictions of the internal shockwave will also be discussed.

4.2 Results

4.2.1 Shadowgraph images of metal ablation

Two metal samples (copper, zinc) were ablated using different laser fluencies. Four different energies were used for copper (0.4, 1, 6 and 12 mJ) and two (0.4 and 1 mJ) for zinc. Figures 4.5 a, b, c show a series of time resolved laser ablation images of copper at different energies. At low laser energy, external shockwave propagation is visible (Figure 4.5 a) via a series of time-resolved shadowgraph images with no significant droplet ejection. As the laser energy increases, obvious particle ejection from the surface can be observed (Figure 4.5 b, c). The shape of the shockwave is almost hemispherical at low laser energy, but as energy increases, the incident laser interacts with the original shockwave structure and produces the central distortion of the wave (c.f. Figure 4.5b and d) on the hemispherical one. The structure is quite complex, and at very high laser energy, the laser ionizes air molecules on the path to the sample surface. This secondary structure has been studied elsewhere [8]; in this work, it is assumed that the secondary shockwave does not influence the particle ejection from the surface. The copper particles were cast out at an angle to the surface normal and formed a conical shape (cf. Figure 4.5 b, c and the sketch of this shape in Figure 4.5e). The extent of the particle ejection increases with the increasing laser energy, which corresponds to the larger crater volume. The particles observed in the shadowgraph images were estimated to be several hundred nanometers to several micrometers

large. In the case of 6 mJ laser energy, large particles with sizes larger than 10 micrometers can be seen at 2~3 microseconds after the laser pulse (Figure 4.5c).

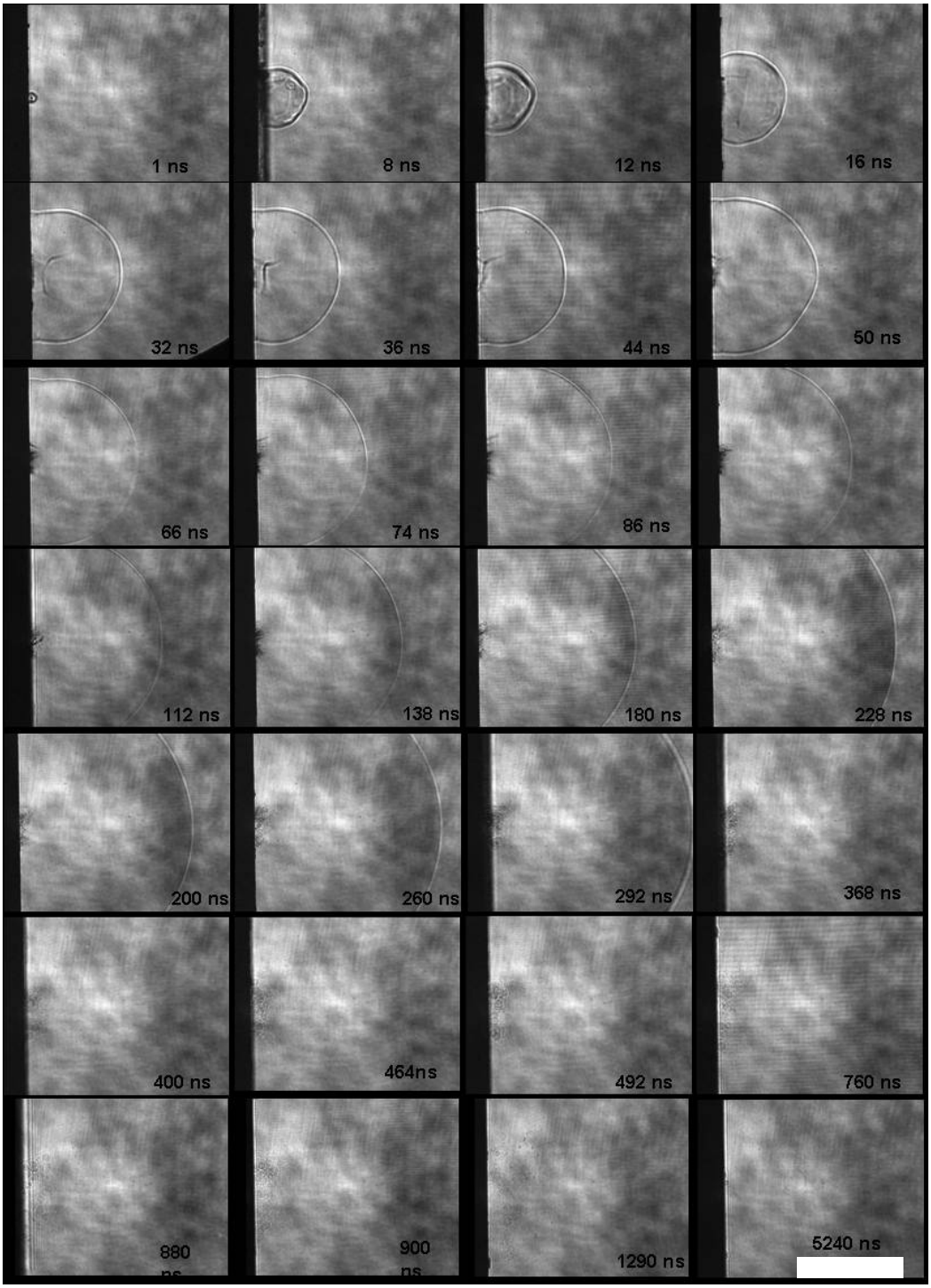

Figure 4.5 (a) Shadowgraph images from ablation on copper at 0.4 mJ

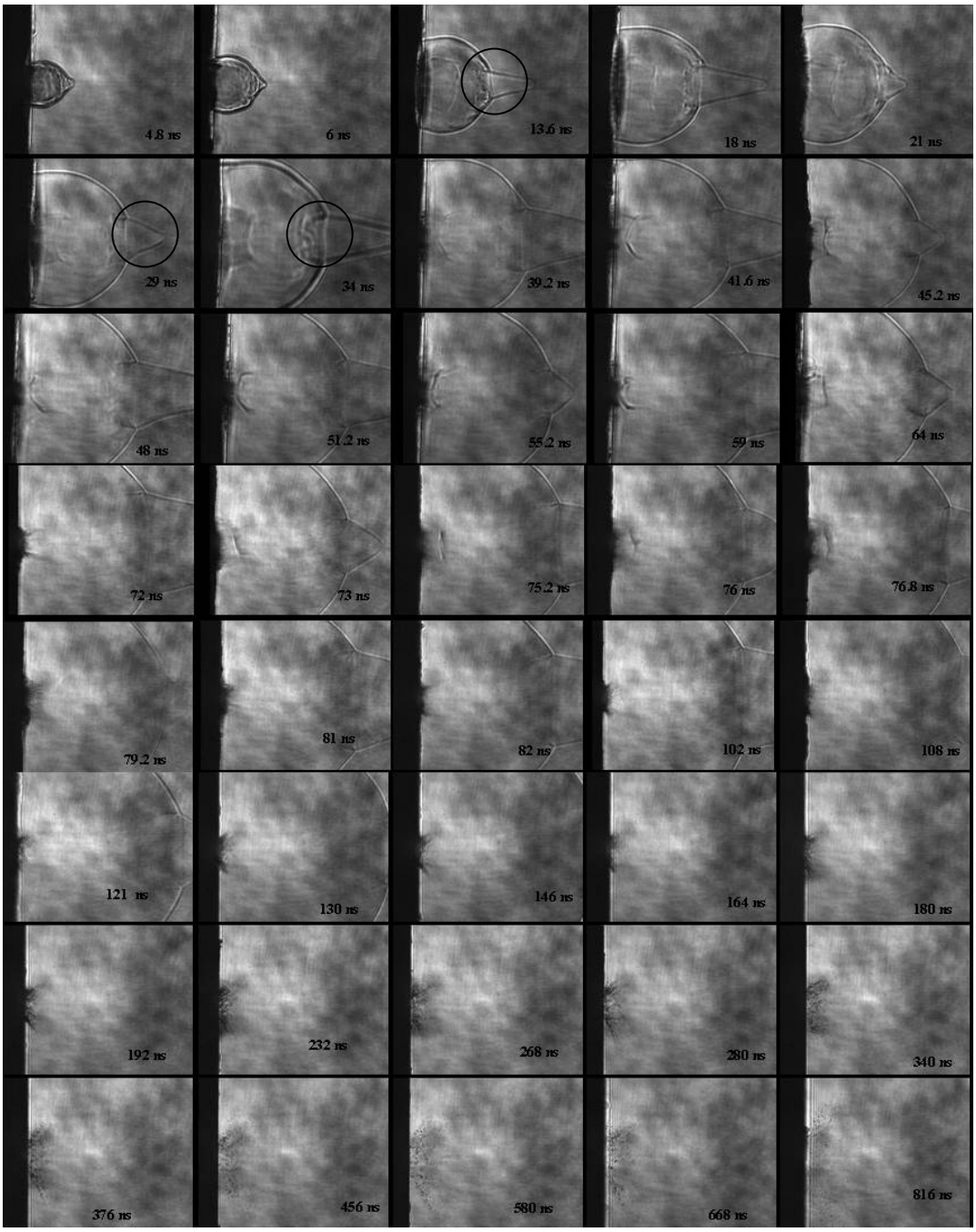

Figure 4.5 (b) Shadowgraph images from ablation on copper at 1 mJ

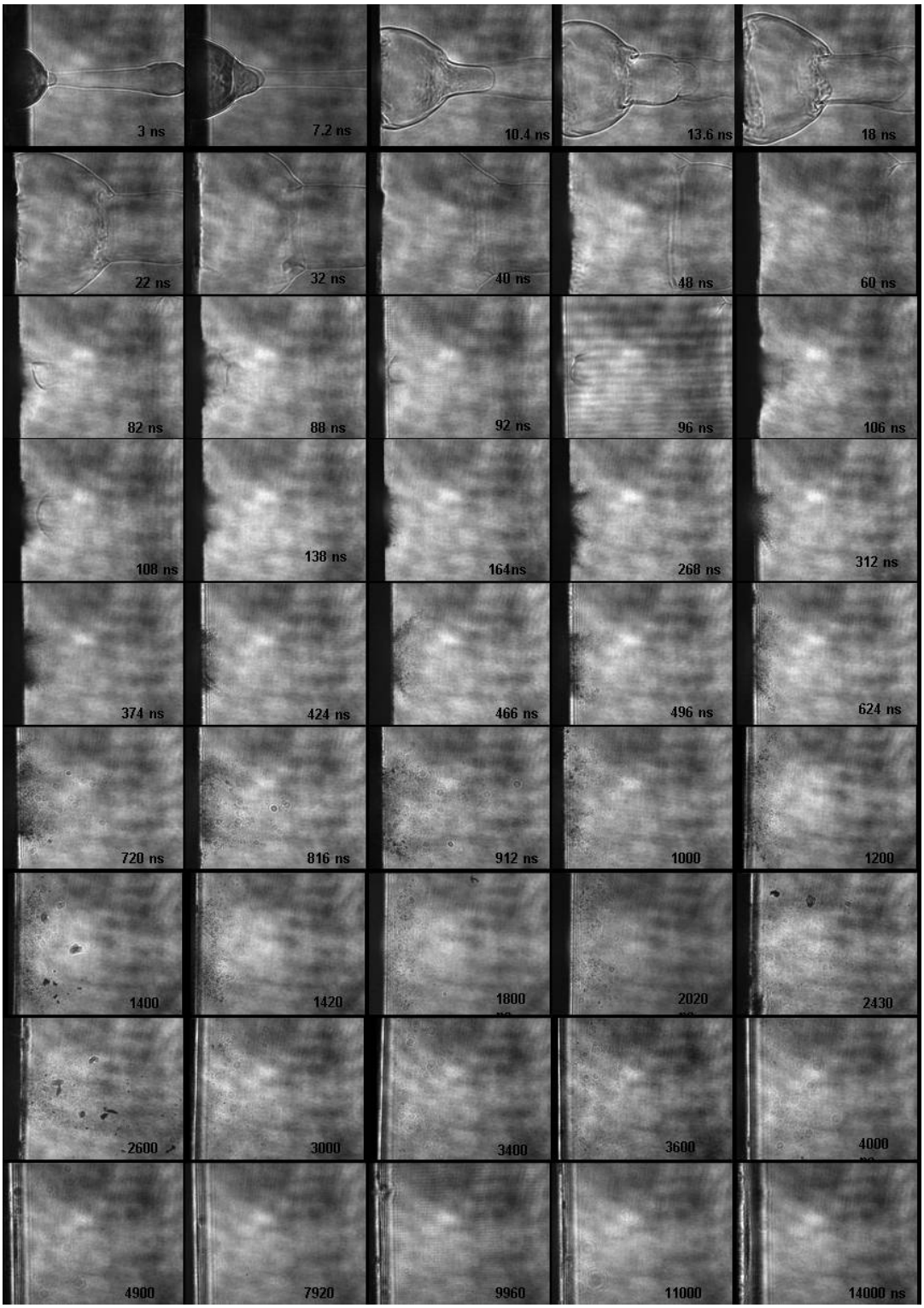

Figure 4.5 (c) Shadowgraph images from ablation on copper at 6 mJ

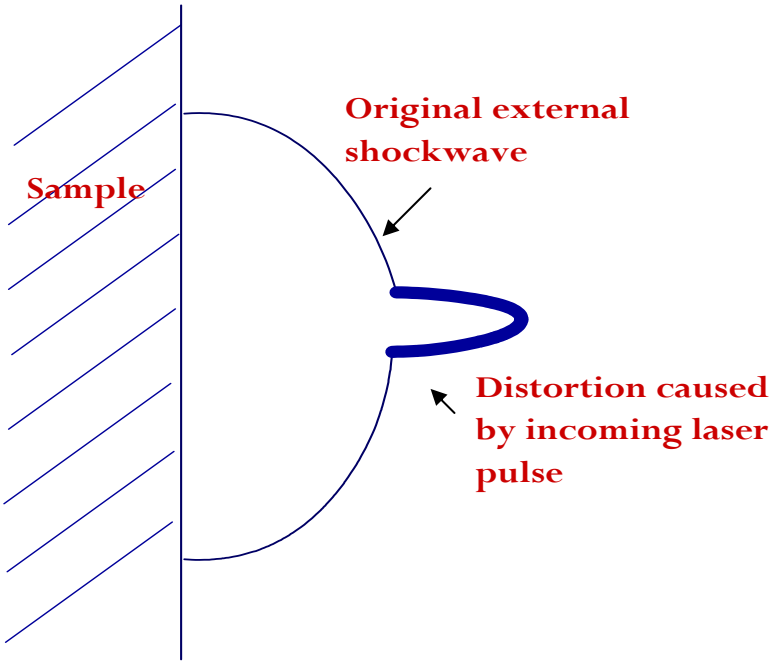

Figure 4.5 (d) Sketch showing shockwave distortion caused by incoming laser

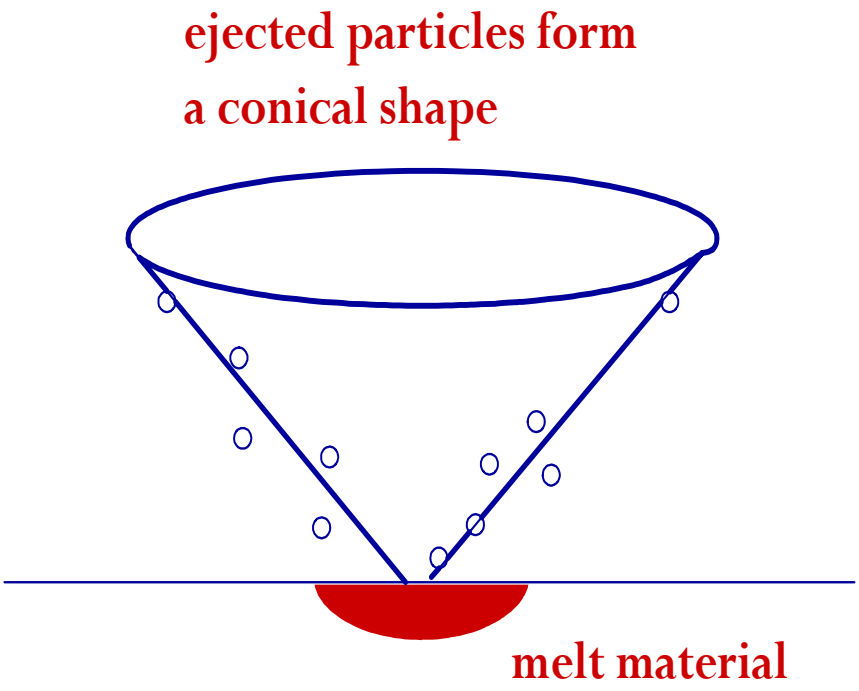

Figure 4.5 (e) Sketch showing ejected particles from melt forming a conical shape

4.2.2 Shadowgraph images of silicon ablation

The shadowgraph images after the incident laser pulse reached the silicon are demonstrated in Figure 4.6 a, b, c. Although the images were taken at different experiments at each delay time, the repeatability of each experiment was pretty good. The darker region in the shadowgraph image represents the vapor produced by the laser pulse. The vapor density decreased as it expanded and can be observed in the region of less dark color at a later delay time. For a energy (0.4 mJ) lower than a threshold laser energy, significant ablation in silicon is not observed (Figure 4.6 a). At higher laser energy (1 and 6mJ), obvious particle ejection from the surface is observed (Figure 4.6 b, c). Unlike other studies [9-11] and also in the previous section, where ablated particles were ejected at an angle to the surface normal, the ejection of silicon particles, except in the very early stage, were perpendicular to the surface. The stream of ejected particles resembles that of a liquid jet and we assume the particles were in the liquid phase. A proposed model discussing this behavior is present in 4.3.4. The particles from the stream last for ~2 microseconds after the duration of the laser. The ejection speed of these particles can be obtained by measuring the position of the front end of the jet. Figure 4.7 shows the axial distance versus time of the particles at different laser energies along with constant speed lines to fit the data. Higher laser energy results in particles with faster ejection speed. Similar to copper, 2 microseconds after the laser pulse, very large particles were observed for several microseconds. These large particles are irregular in shape and believed to be in the solid phase when they are ejected. The

ejection of particles can last for 50 microseconds after the laser pulse as energy increases.

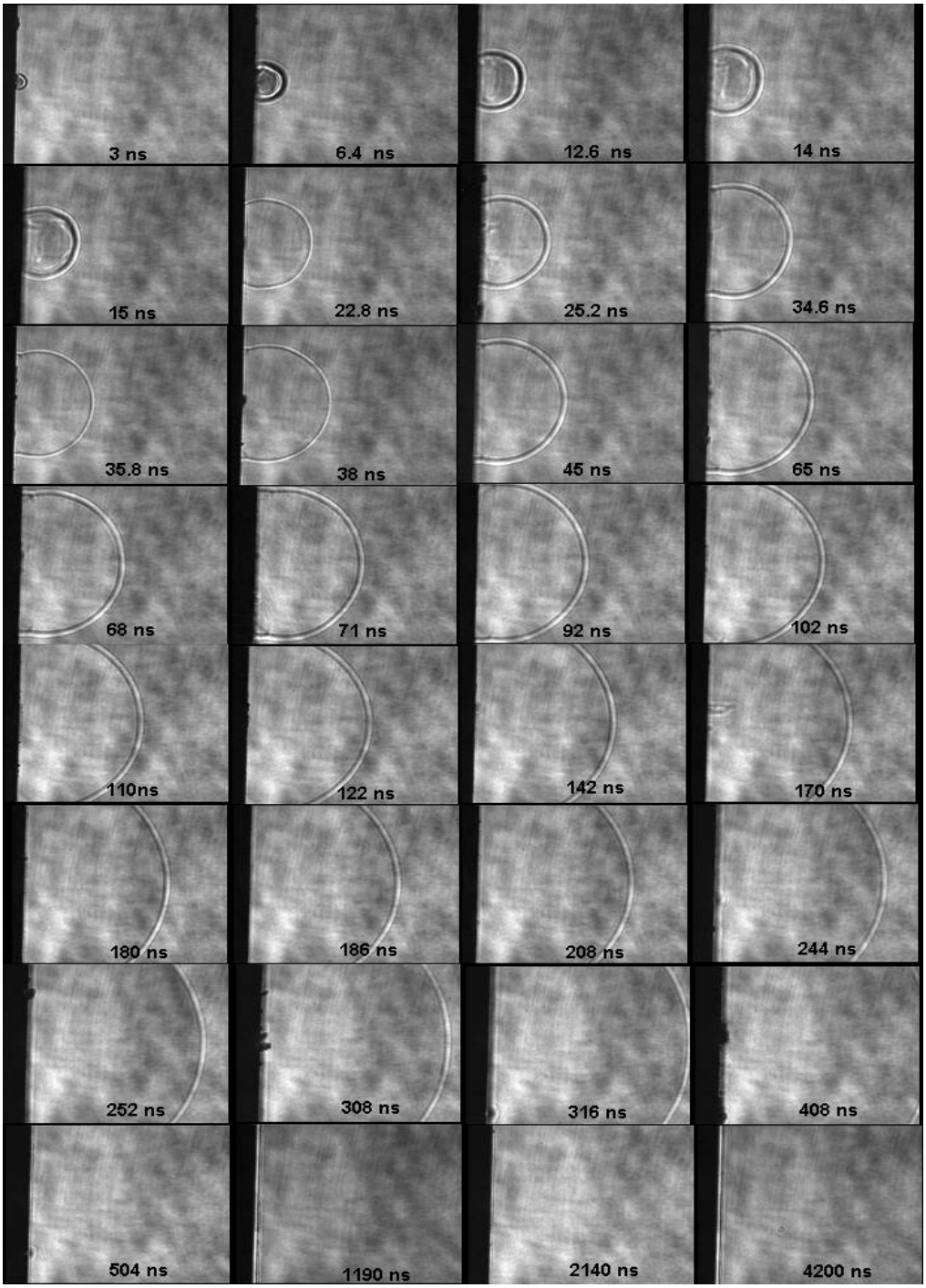

Figure 4.6 (a) Shadowgraph images from ablation on silicon at 0.4 mJ

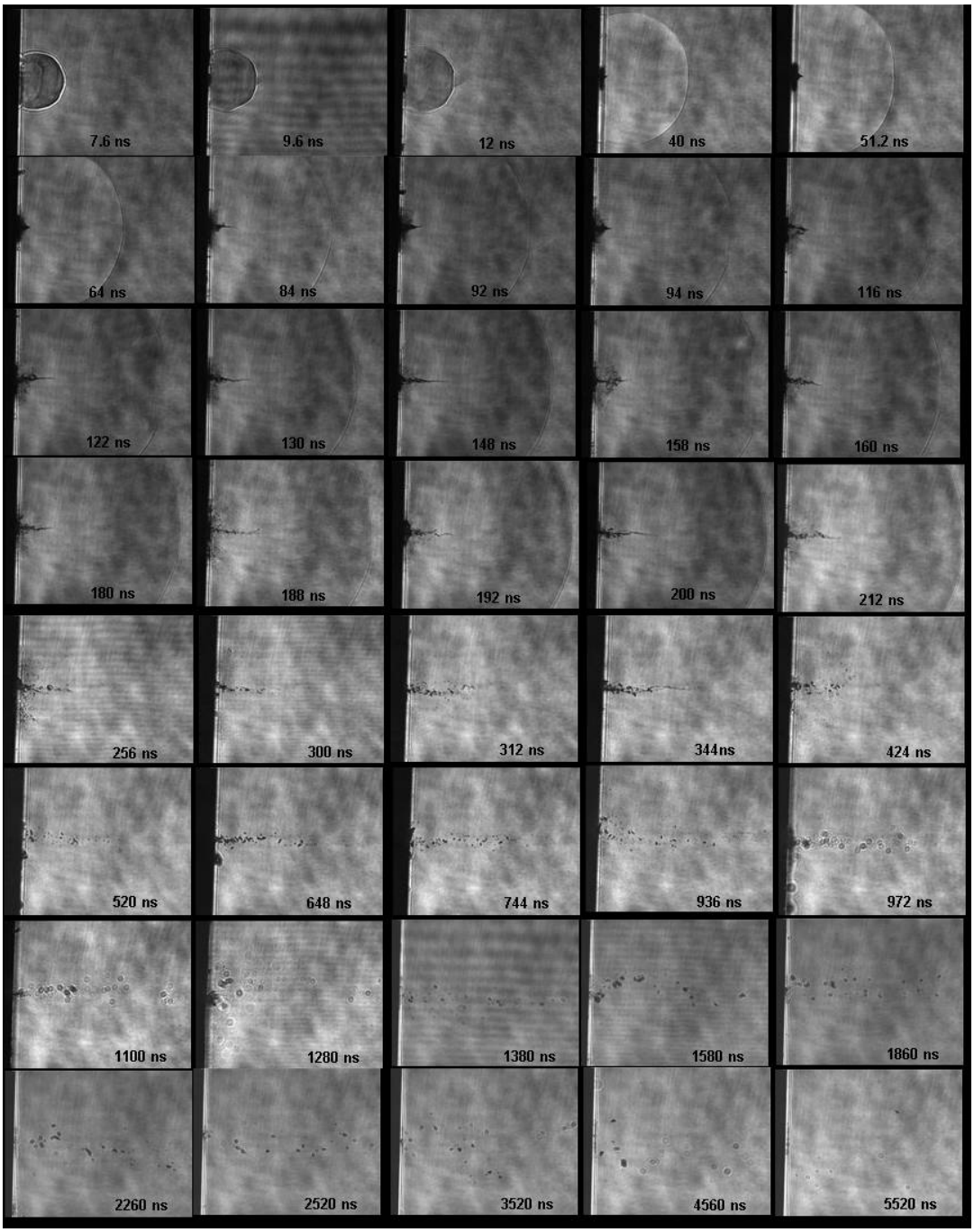

Figure 4.6 (b) Shadowgraph images from ablation on silicon at 1 mJ

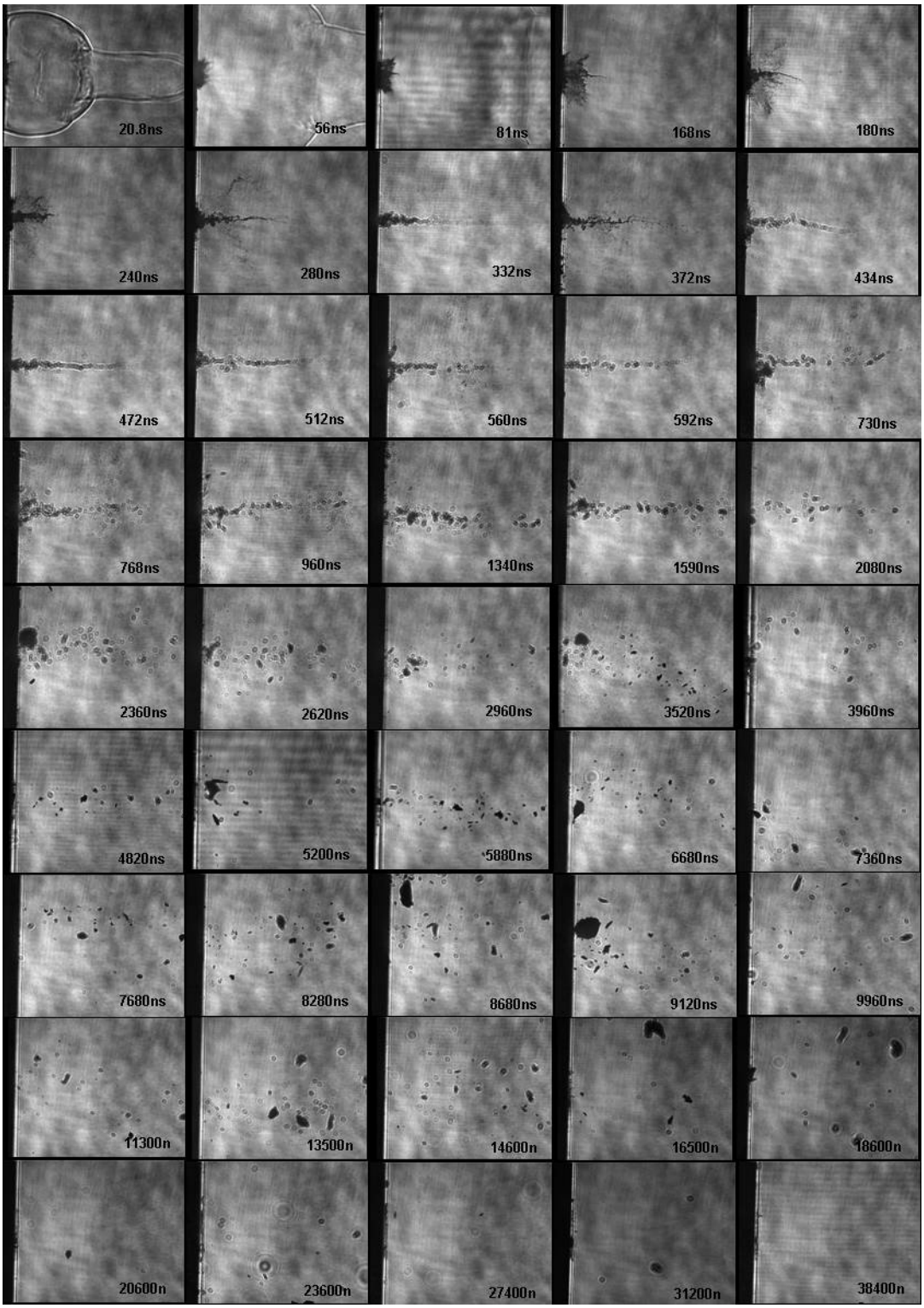

Figure 4.6 (c) Shadowgraph images from ablation on silicon at 6 mJ

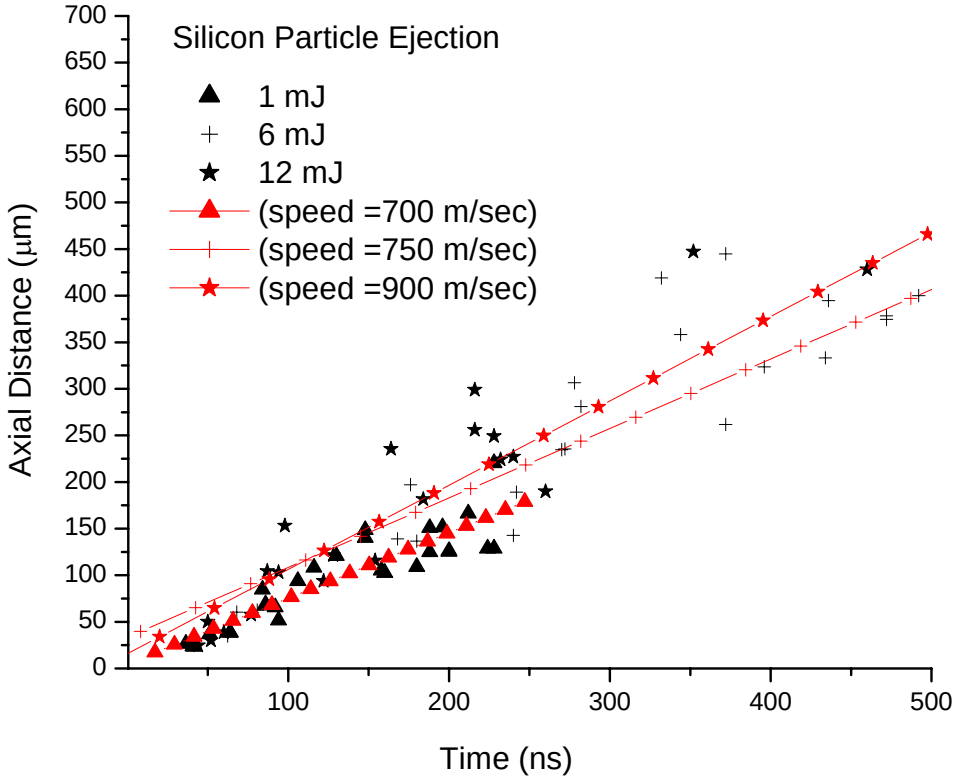

Figure 4.7 Trajectory of front-end position of silicon particles at different laser energy

4.2.3 External Shockwave propagation speed

The shockwave speed is related to the initial plume velocity, which is proportional to the square root of E/M (Equation 4.11). The laser energy E and the amount of vaporized mass M are needed in order to calculate the propagation of the shockwave and contact surface. However, the value of vaporized mass M is difficult to determine; indeed, at high laser energy, the crater volume was primarily caused by the removal of the large particles and not the vaporized mass. The total mass removed by the laser pulse can be obtained by measuring the crater volume which is due to both the vaporized mass and the ejected particle mass. Therefore, at

higher laser energy, which is accompanied by significant particle ejection, the evaporated mass, M, cannot be directly measured from the crater volume. For the particular experiment where laser energy was 0.4mJ, no significant particles were observed and the removed vaporized copper was found to be 20 ng per pulse using the average crater volume removed by 50 laser pulses. The average removal mass 20ng is then used to represent the evaporated mass. For higher laser energy where particle ejections take place, two possible procedures to obtain the evaporated mass are used. Yoo et al [12] employed a one-dimensional model to calculate an evaporated depth. They calculated the evaporated thickness and found it was linearly dependent on laser fluence. Therefore the assumption that the vaporized mass varies linearly with the laser fluence is used in the present numerical simulation as the first approach. The mass 20ng measured at 0.4mJ is extrapolated to obtain the evaporated mass for higher laser fluence, e.g., the mass was 50ng for 1mJ laser energy. In the second approach at higher fluence, the evaporated mass is kept constant at 20ng; the increased crater volume is all attributed to the particle ejection. It is presumed that the "actual" evaporated mass, M, is bounded by the two approaches noted.

The shockwave propagation speed changes with increasing laser energy. From Figure 4.3, the speed of the external shockwave generally increases with the laser energy. However, the speed at laser energy 6mJ is similar to that at 12mJ, which could be because part of the laser energy was lost due to air ionization and plasma shielding and was not incident on the sample.

Figure 4.8 shows the measured external shockwave front position with respect to time at 0.4 and 1mJ for different materials, and the simulated results for copper calculated by Wen [13]. In the case when a secondary shockwave structure was formed at higher laser fluence, the assumed hemispherical shape determines the shockwave front position. The shockwave for copper moves faster than the shockwave for silicon and zinc, which could result from the smaller evaporated mass in copper than the other two materials, and thus more energy available to drive the shockwave, e.g. higher temperature and higher sound speed. The simulation curves of copper match the experimental points well at both 0.4 and 1 mJ from the beginning. The speed gradually slows to the normally observed blast wave relation $R \sim t^{0.4}$ (as shown in Figure 4.8). The expansion model provides a good fit for the experimental data. However, in the case of 1mJ energy, both approaches for determining the evaporated mass (the mass being obtained from either linear extrapolation of the mass in 0.4 mJ to yield 50ng, or the mass is assumed to be constant) produce similar results except very small time. Smaller mass results in faster propagation in the early time. Note that the blast wave model involves only energy but not mass. The effect of the vapor mass primarily influences the initial stage of the shockwave propagation when the blast wave relation is not valid.

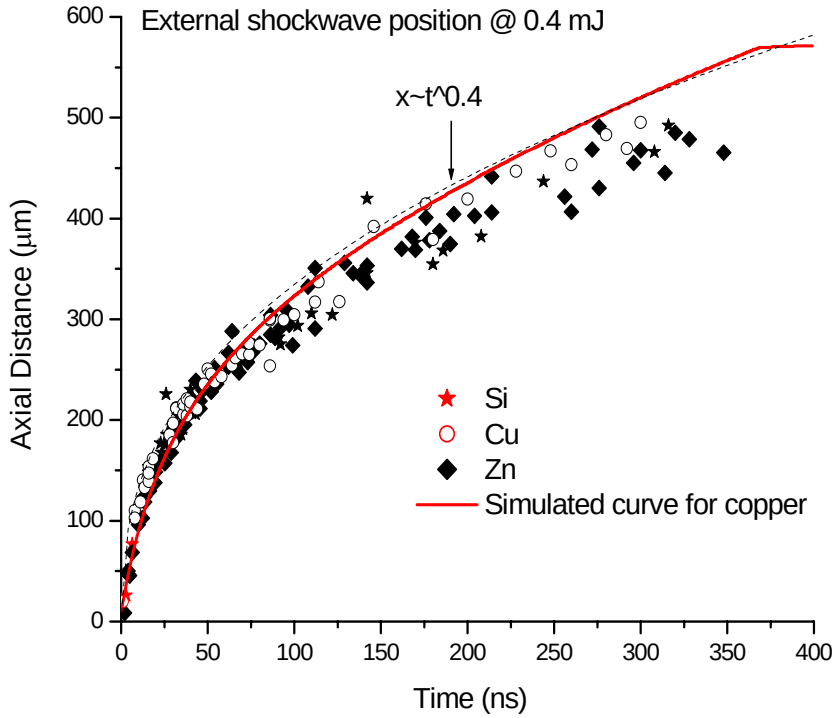

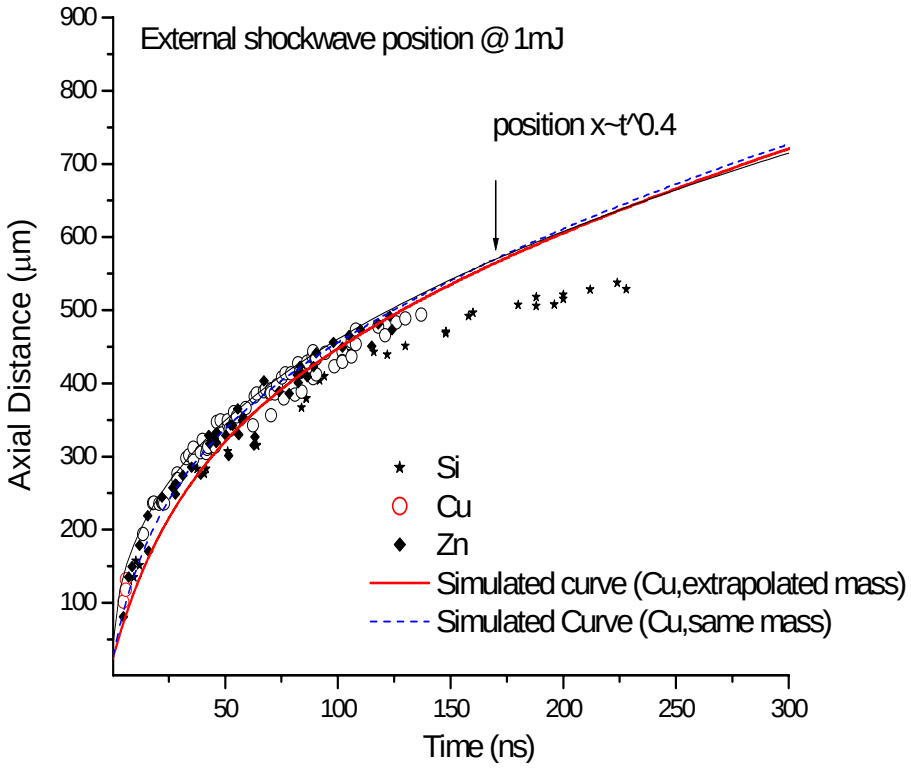

Figure 4.8 External shockwave front positions for different materials

4.3 Internal shockwave and its role in material ejection

4.3.1 Evidence of internal shockwave

Observation of the internal shockwave can be seen in both metals and silicon. As in previous sections, copper is used to represent the case of metals; zinc has the same behavior but at different delay time. Examining Figures 4.5 a, b, c in detail, the internal shockwave appeared to be close to the laser spot. Selected images at laser energy of 1mJ are shown in Figure 4.9. The time resolved images show that the shockwave changed shape with time as it traveled toward the surface and then reflected back from the surface. Unlike the spherical expansion model and prediction, the shape of the internal shockwave is not spherical near the laser spot. As it approaches the surface, it is bent toward the surface (with the central portion closest to the surface, a U-shape at 21, 39.2, 41.6 ns). The central portion of the shockwave strikes the surface first (~51.2 ns) and reflects back while the remaining outer portion still moves toward the surface; therefore the shockwave shape becomes a reversed “M” shape (67 ns). Then the outer portion of the shockwave also reflects from the surface and eventually the reflected shockwave dissipates as it travels back to the contact surface (~75 ns). The reason that the internal shockwave is only visible near the laser spot with a nonspherical shape is not clear. Several possible reasons can cause the deviation from the ideal spherical assumption:

1. The target surface influences the motion of the internal shockwave as it approaches the surface and alters the shape and speed.

2. The shape of the expanding plume is not spherical especially in the early stage when the central portion of the plume is distorted by the incoming laser pulse and forms a secondary structure at high laser fluence.

The combination of the above effects contributes to the observed non spherical shape of the internal shockwave. In the case of silicon, direct observation of the internal shockwave is not as obvious as for metals. Figure 4.10 shows the selected time resolved images at laser energy 12mJ. As shown in Figure 4.10, internal shockwave is observed at a time of 7ns. At this high laser energy, the boundary effects can be clearly observed at 7ns; the outer part of the internal shockwave is still in contact with the plume boundary while the central part is less influenced by the boundary and still moves inward and eventually evolves to a U-shape. However, the shockwave at later time is not readily observed due to the particle ejection pattern of silicon. Ejected particles of silicon form a liquid jet erupting perpendicularly from the surface that differs from particles from other materials. Without external interference the liquid jet should move as a stream. However, the images of the silicon ablation show that the jet branched out from the main jet. The internal shockwave probably interacted with the silicon jet and the interaction caused the lateral movement of the particles (~100 to 200 ns shown in Figure 4.10). The size of the jet stream decreased after the point of lateral movement evidences the removal of mass from the main jet.

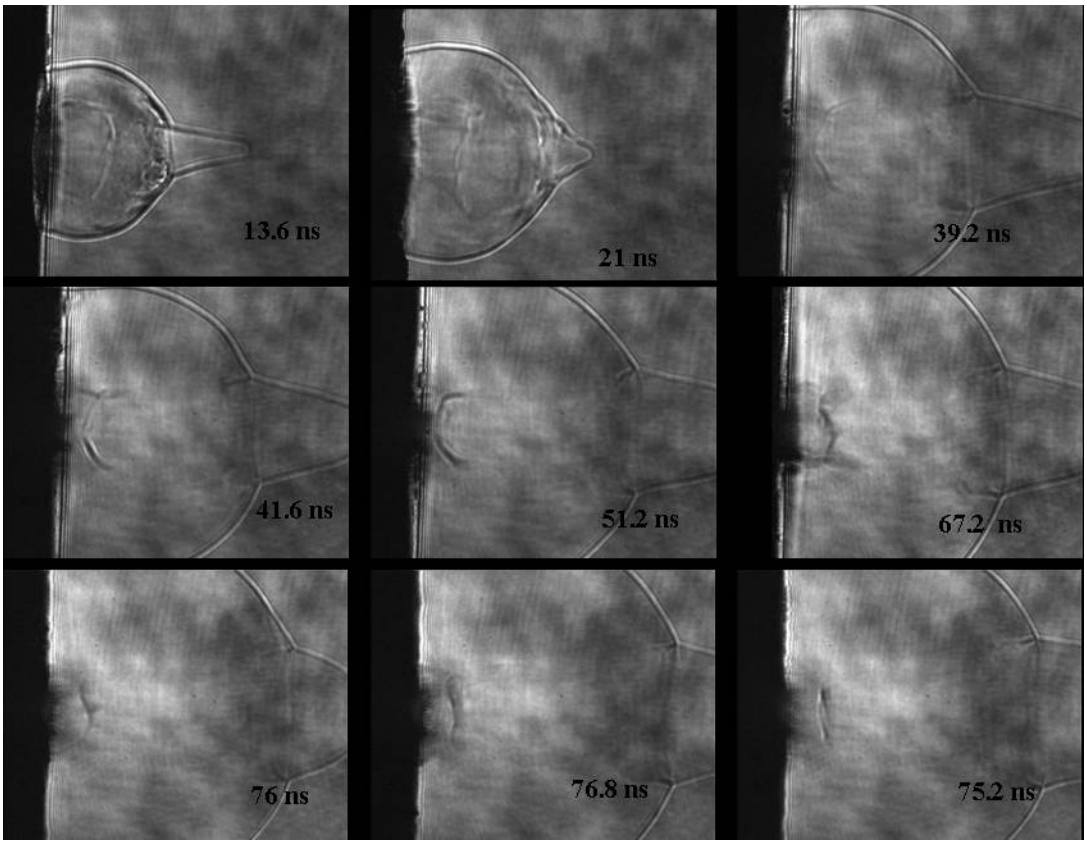

Figure 4.9 Selected shadowgraph images showing internal shockwave from ablation on copper at 6mJ

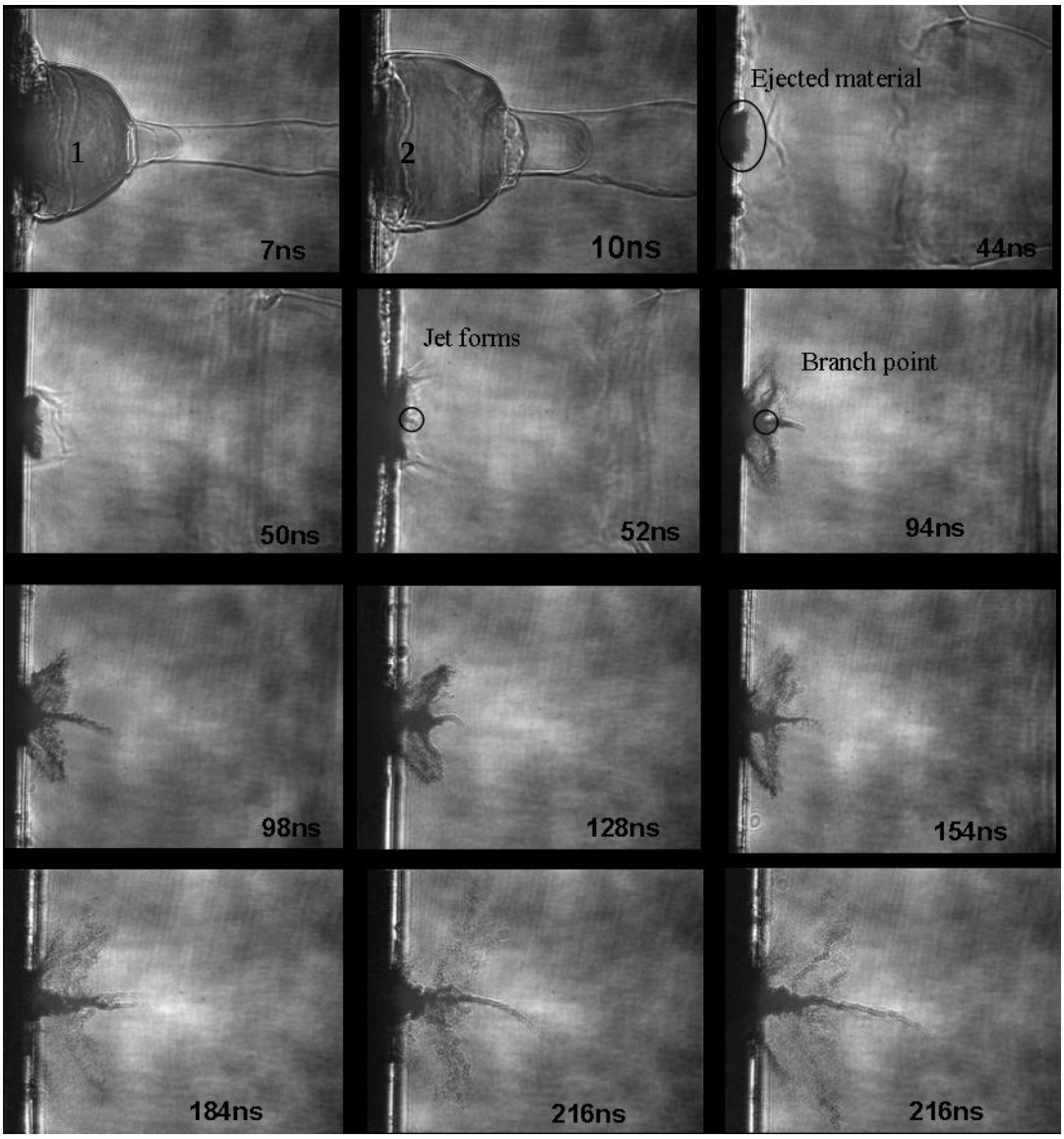

Figure 4.10 Selected shadowgraph images showing internal shockwave from ablation on silicon at 12mJ

4.3.2 Relation of internal shockwave reflection to the generation of particles from shadowgraph images

The images of copper ablation (Figure 4.5) show that the particle ejection happens after the internal shockwave strikes the surface and reflects back. The

exact time the internal shockwave impacts the surface is hard to determine. The shadowgraph image is taken at a fresh surface at each experiment. The energy of the laser varies for each test and the surface condition at each spot is different. Also the shape of the internal shockwave deviates from a spherical shape. For copper at the energy of 1mJ (Figure 4.5 (b)), the internal shockwave possibly reaches the surface between 50~60 ns after the laser pulse, and is followed by ejection of particles ~20 ns later (~70 ns after the laser pulse). At the energy of 6mJ (Figure 4.5 (c)), the internal shockwave possibly reaches the surface between 90~100 ns after the laser pulse and particles start to eject from the surface ~20 ns later (~110 ns after the laser pulse). For zinc at 1mJ, the internal shockwave reaches the surface at ~80 ns and particles moving from the surface are observed ~20 ns later (at ~100 ns after the laser pulse).

The relation of the internal shockwave and particle ejection is less obvious for silicon due to the fact that fewer images with the internal shockwave were obtained. Images at higher laser energy 12mJ (Figure 4.10) provide the best example. The internal shockwave was observed at 7 and 10ns, which should reach the surface in a short time. The ejected material was observed as early as 20ns and should be caused by the first shockwave. However, it is not able to obtain the exact onset time of the material ejection. The internal shockwave was observed again at 44ns and reached the surface at ~52ns. This could be the internal shockwave being reflected again from the contact surface. The jet started to appear at ~52ns and propagated outward. The speed of the silicon jet is ~900 m/sec as shown in Figure

4.7; the shockwave speed is much faster than the particle speed. The estimate of the speed of the shockwave is obtained from the position of 1 and 2 shown in Figure 4.10 to be about 4000 m/sec. As the shockwave moves toward the surface, it interacts with the front of the liquid jet. The impacting shockwave causes lateral movement on part of the liquid jet while another part of the jet still moves forward. This also explains why the thickness of the jet changes from the branching point. As shown in Figure 4.10 at 94 ns, the branches stemming from the main jet show the interaction with the again reflected shockwave.

Although the position of the internal shockwave for silicon is easily observed, the positions for copper and zinc are not easy to record. The trajectory of the shockwave is plotted in Figures 4.11 and 4.12 for copper and zinc at 0.4 and 1mJ, respectively. The position of the internal shockwave is determined from the location of its central part. The position of the internal shockwave for higher energies scatters with time and is not included. As shown in Figure 4.5, no reflected shockwave from the surface was observed for copper at lower energy. The weak internal shockwave generated at lower energy may not reflect from the surface and dissipate. At higher energy which generates stronger shockwaves, the internal shockwave reflected from the surface and possibly even reflected back from the contact surface again. Therefore it is more difficult to determine the trajectory. The time for the internal shockwave generated in the zinc sample to strike the surface is later than that for copper. For the same amount of energy, the mass of vaporized zinc is much higher (high volatility) than for copper. Higher mass results in a

slower shockwave speed as discussed previously and therefore it strikes the surface later than copper

Also shown in the Figures 4.11 and 4.12 are the predicted curve obtained by Wen's model [13]. The analysis considers the internal shockwave and includes the internal shockwave striking the sample surface and reflecting back. As shown in Figures 4.11 and 4.12, the predicted trajectory of the internal shockwave partially agrees with the experimental results. In Figure 4.11, which is the lowest energy case of 0.4mJ, the predicted internal shockwave strikes the surface is about 60 ns whereas the measured time from the experiment was about 50 ns. The internal shockwave position predicted by the model provides a slower moving speed and a later time for the internal shockwave to begin to move toward the surface. Several factors can cause difference between the predicted and measured results. The calculation is based on a spherical shape and shadowgraphs show the internal shockwaves have more complicated shapes. Significant errors in the predicted results can be caused by the deviation from the ideal shape. Another reason the simulation predicted a slower internal shockwave and turning back time could be due to the actual evaporated mass. The evaporated mass was obtained from the crater volume measurement by assuming no melt ejection. Though the melt ejection was not significant at lower laser fluence, scarce existence of small droplets result in less vaporized mass and slower internal shockwave. This postulation is better illustrated in Figure 4.12. As discussed in 4.3.4, evaporated

mass was assumed to increase linearly with laser energy, which may overestimate the mass since melt ejection became dominant at higher laser energy.

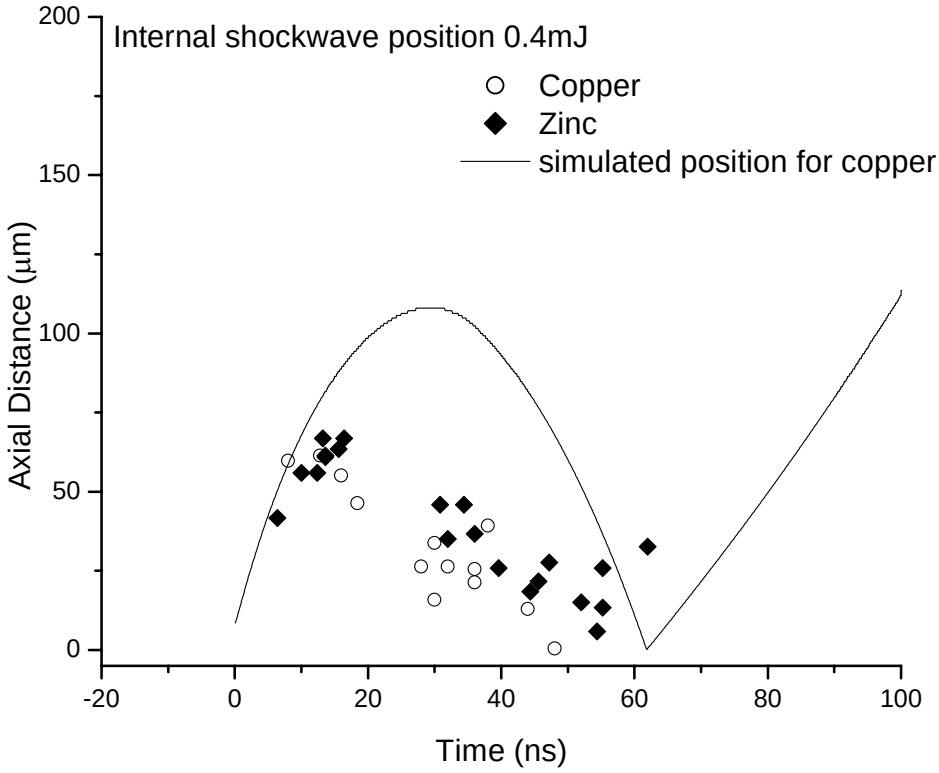

Figure 4.11 Measured temporal internal shockwave positions for copper and zinc, and predicted result for copper at 0.4mJ energy.

To evaluate the effects of the evaporated mass on the prediction of the internal shockwave, calculations were made for different mass at the energy of 1mJ. A higher mass (50ng) resulted in a shockwave striking the surface time at ~80 ns and a lower mass (20ng) predicted the time at ~45 ns. Note the time for the internal shockwave to strike the surface is ~60 ns from shadowgraph images. Based on the

data, a presumed band (bounding the internal shockwave positions) is drawn in Figure 4.12 as a visual guide.

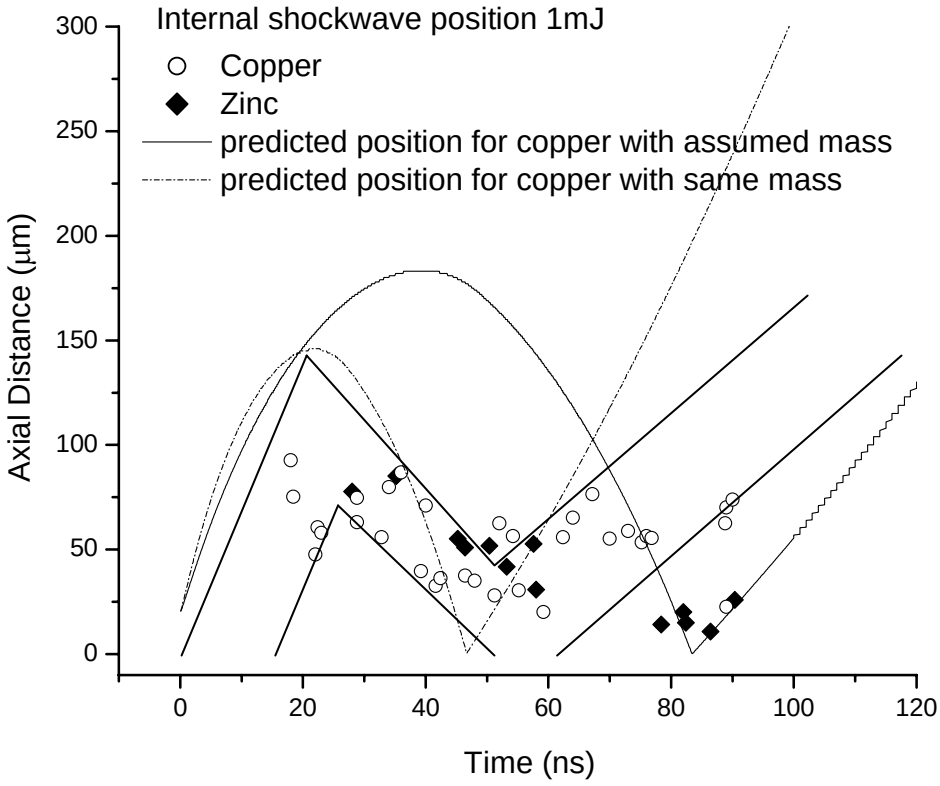

Figure 4.12 Measured temporal internal shockwave positions for copper and zinc, and predicted result for copper at 1mJ energy.

4.3.3 Difference in particle ejection for different material

From the shadowgraph images taken for different materials, it is observed that the ejection behavior of the liquid layer have significant difference when high laser fluence is applied. As previously mentioned, metal ejection forms a reversed cone shape while silicon ejection resembles a liquid jet. Possible reasons for the

different behavior include the different in change in density when the solid melts into a liquid and the thickness of melting layer.

Silicon possesses a rare property when it melts from solid to liquid. For most materials (especially pure metals and alloys) the volume increases when the phase changes from solid to liquid. The density of liquid silicon is larger than solid silicon. Thus, the volume of silicon decreases when it melts into liquid. The properties of the material are listed in Table 4.1.

Table 4.1

Property / Metal	Melt Temp (K)	Boiling Temp (K)	Heat of fusion (KJ/mole)	Heat of vaporization (KJ/mole)	Specific Heat (KJ/Kg-K)	Liquid density (Kg/m3)	Solid Density (Kg/m3)	Thermal conductivity (W/m-K)	Heat Diffusion coefficient
Zinc (Zn)	693	1180	6.67	114.2	0.388	6900	7140	116	0.000042
Copper (Cu)	1358	2836	13	306.7	0.385	8600	8933	401	0.000117
Silicon (Si)	1685	3538	30.66	824	0.705	2520	2330	148	0.000089

For the metals, the volume of the liquid is larger than that of the solid, thus the metal expands from the flat surface and the convex shape of the liquid metal is caused by surface tension. When the internal shockwave strikes the convex shaped surface, it pushes the molten liquid away and forms a concave liquid surface (Figure 4.13 a). For a strong approaching shockwave; particles are ejected from the liquid surface in the lateral direction along the crater boundary, which is why the outline of the ejected material forms a reversed cone shape as observed in the shadowgraph images (Figure 4.5 b, c and d).

As noted above, when silicon melts from solid to liquid, the volume decreases which causes the surface of the molten silicon to recede and forms a concave shape (Figure 4.13b). When the internal shockwave strikes the surface, it forces the molten silicon downward and outward and, as noted for metals, particles are ejected along the crater boundary. However, unlike materials with a convex surface, the molten silicon also forms a liquid jet in the center of the molten pool.

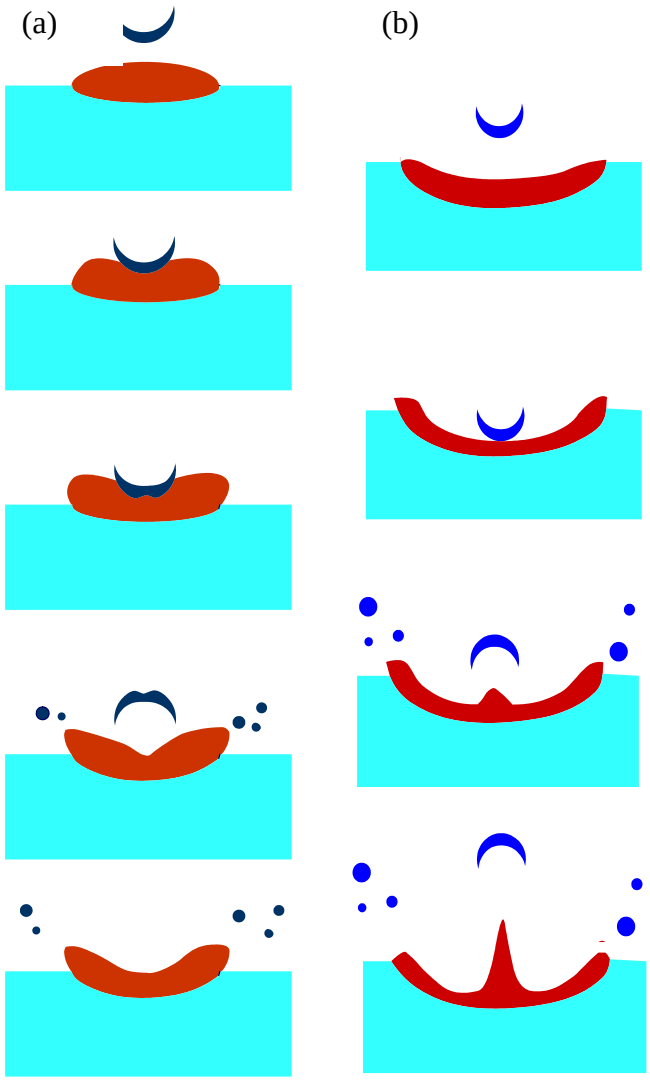

Figure 4.13 Assumed response of different material to shockwave (a) metal (volume increase of liquid) (b) silicon (volume decrease of liquid)

Another consideration in particle ejection is the molten layer thickness. The continuing jet observed in silicon ablation required a liquid layer thick enough to exist for at least ~2 microseconds. The absence of a jet in copper suggests that the molten layer is either thinner or it cools faster.

A numerical simulation is made to estimate the molten layer thickness for different materials. The conservation of energy for laser heating a solid is given by:

$$\rho\, C\, \frac{\partial T}{\partial t} = \rho\, C\, u \frac{\partial T}{\partial x} + \frac{\partial}{\partial x}\left(k \frac{\partial T}{\partial x} \right) + I_0(t)\, \alpha\, \exp(-\alpha x) \qquad (4.12)$$

where T is temperature, t is time, ρ is density, C is specific heat, u is the receding velocity of the sample during evaporation, k is thermal conductivity, I_0 is the temporal laser irradiance, and α is the optical absorption coefficient of the sample material.

The energy equation may also be written in terms of the enthalpy which is convenient for satisfying the phase change that occurs at the liquid-solid interface. A discussion of the enthalpy formulation is found in [12,14]. The energy equation is subject to boundary conditions at the surface, x=0, and at the material thickness, x=L. At the surface, x=0, the energy transfer was calculated as the latent heat of the evaporated mass, where the mass flux of vapor evaporated from the liquid surface is given by the Hertz-Knudsen relation [15] At x=L, the temperature is unaffected by the laser irradiance, i.e. T(L, t) = T_i, where T_i is the initial temperature. For specified laser irradiance I_0, the temperature distribution can be solved and the thickness of the molten layer can be obtained.

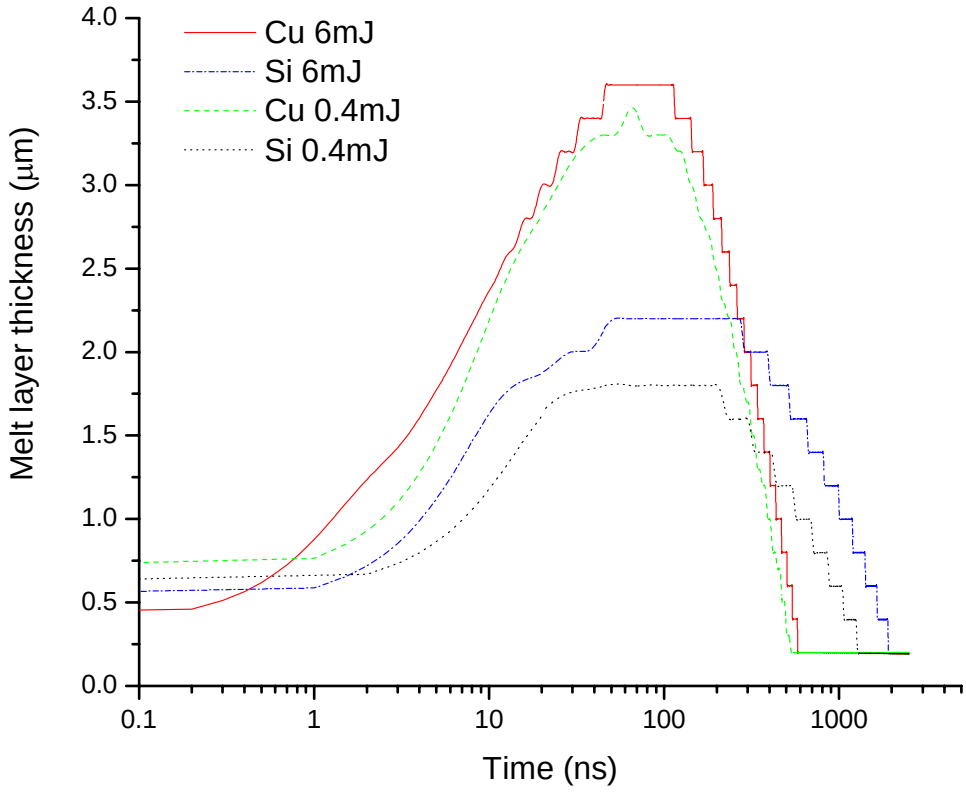

Figure 4.14 Estimate of melt thickness for copper and silicon with different laser energy

As shown in Figure 4.14, though the melt thickness was greater for copper than for silicon, the copper melt cooled faster than for silicon. The duration and thickness of the melt layer increased with increasing laser energy. For copper the melt layer fast diminished 100ns after the laser pulse, while for silicon the melt layer could last much longer (more than 1000 ns after the laser pulse at 6mJ).

Figure 4.15 shows the measured crater depth for copper and silicon with respect to laser fluence. For copper, the maximum melt thickness predicted (3.7 micron)for laser energy 6mJ is close to the measured depth at the same energy (~5

micron). The maximum melt layer occurred at 50~100 ns after the laser pulse which was about the time the internal shockwave strikes the surface. It was assumed that the whole melt layer was pushed away by the impact of the internal shockwave for copper. For the case of silicon, however, the calculated melt layer can not explain the much larger depth obtained for the ablation crater for high laser fluence. Another material removal mechanism is considered to be responsible for the large ablation rate and is discussed in the next section. However, the longer lasting melt layer for silicon supported the liquid jet formation which can be observed until ~1 microsecond after the laser pulse.

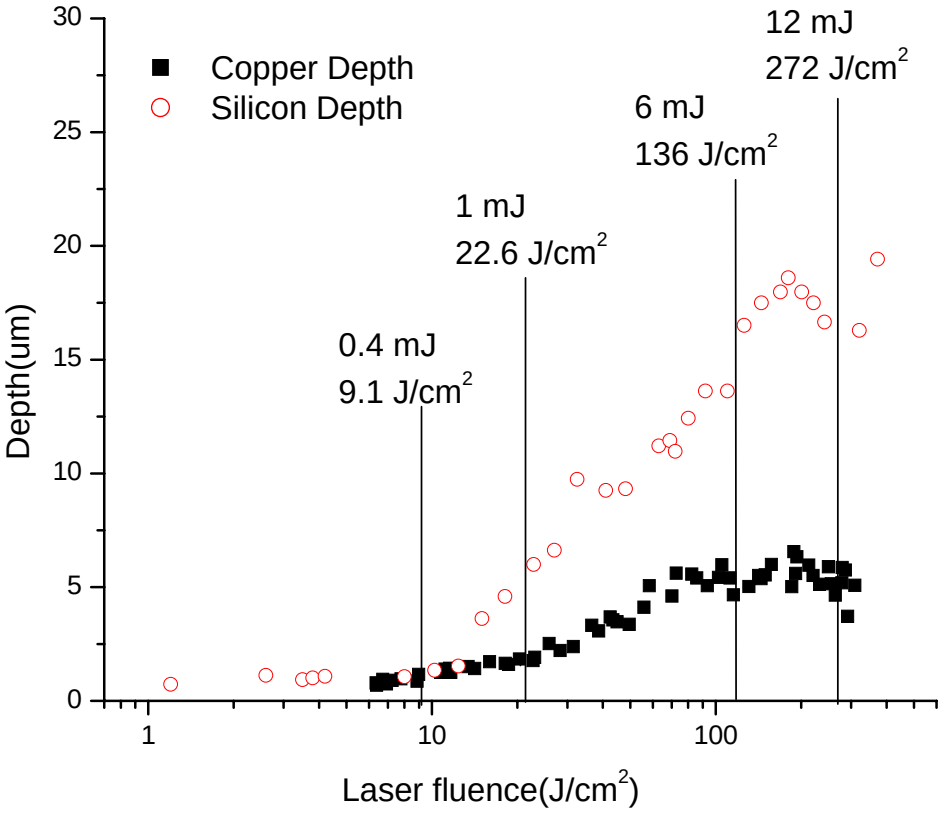

Figure 4.15 Ablation rate for copper and silicon at different laser fluence

4.3.4 Change in ablation mechanism with laser energy and a new explanation for the previously postulated phase explosion

The vapor expansion model considers only the total energy in the vapor plume. But the ablation rate is critically dependent on the laser fluence, or laser irradiance, i.e. the value of the laser energy is deposited on the sample surface. The distribution of the energy between the vaporized and molten material vary with the laser fluence. Figure 4.15 shows the measured crater depth for copper and silicon with respect to laser fluence. Shadowgraph images were taken at the four energies and their corresponding laser fluencies which are labeled on the figure. The crater depth is less than 1 micron for laser fluence smaller than the corresponding laser energy 0.4mJ. For copper, significant increase in ablation rate starts at about 1mJ and reaches a maximum at about 6mJ (the depth at 12mJ is approximately the same as that at 6mJ). For silicon, the crater depth increases sharply starting at ~0.5mJ, and flattens out at roughly 8mJ. The results for the crater depth agree quite well with the shadowgraph images. At low laser energy (0.4mJ), vaporization is the dominant ablation mechanism and no particles were observed in the shadowgraph images. A reversed cone shape of particle ejection from copper and the jet from silicon were recorded for energy >1mJ. The significant particle ejection coincided with the increase of crater depth at higher laser energy, the change of ablation rate can therefore be concluded to result from the occurrence of the particle ejection.

Observation of the shadowgraph images in silicon may provide important information concerning the abrupt change in ablation rate reported previously [12].

Yoo [12] has reported, that the bottom of the crater was smooth at low laser irradiance and became rough at higher irradiance. The change in crater roughness combined with the abrupt change in crater volume when the laser irradiance is higher than a “threshold” value was attributed to the phase explosion phenomenon. From the shadowgraph images taken at higher laser energies (6 and 12mJ as shown in Figure 4.6), it was obvious that big solid particles were ejected following about 2 microsecond of the appearance of the jet stream. These big solid particles, though small in number, contribute to most of the material removal and the volume of the crater. The rough bottom found at high laser irradiance provided support that the material removed was in the solid phase; otherwise effects from surface tension would result in a curved and smoother bottom profile. It is suspected that, at high laser fluence, stresses resulting from the large thermal energy deposition surpassed the mechanical strength and caused the exfoliation phenomenon. As previously observed, the images of the solid particles appeared intermittently rather than continuously. Another possible mechanism is the surface was weakened by thermal stress and was struck by the reflected internal shockwaves which can only be sustained at high laser energy. The striking of the surface by the internal shockwaves results in the solid ejection.

4.4 Summary

Images of the internal shockwaves induced by laser ablation were recorded in shadowgraph experiments. Particle ejection from the surface was observed after the internal shockwave strikes the surface. The previous concept of melt ejection caused by the recoil pressure caused the may be explained by the effects of the internal shockwave. Different material has different particle ejection characteristics; metal ejection forms a reversed cone shape while silicon ejection resembles a liquid jet. The difference may be due to the density change between solid and liquid and the melting thickness. Preliminary calculations of Wen [13] predict the shockwave positions, which partially agree with the surface striking time by the internal shockwave.

References

1. L. I. Sedov, similarity and dimensional methods in mechanics, (CRC Press, 1993).

2. N. Arnold, J. Gruber, and J. Heitz, "Spherical expansion of the vapor plume into ambient gas: an analytical model," Applied Physics A-Materials Science & Processing 69, S87-S93 (1999)

3. A. V. Bulgakov and N. M. Bulgakova, "Dynamics of Laser-Induced Plume Expansion Into An Ambient Gas During Film Deposition," Journal of Physics D-Applied Physics 28, 1710-1718 (1995)

4. M. R. Predtechensky and A. P. Mayorov, "Expansion of Laser-Plasma in Oxygen at Laser Deposition of Htsc Films - Theoretical-Model," Applied Superconductivity 1, 2011-2017 (1993)

5. S. I. Anisimov, D. Bauerle, and B. S. Lukyanchuk, "Gas-Dynamics and Film Profiles in Pulsed-Laser Deposition of Materials," Physical Review B 48, 12076-12081 (1993)

6. Y. B. Zeldovich and Yu. P. Raizer, Physics of SHock wavs and high-temperature hydrodynamic phenomena, W. D. Hayes and R. F. Probstein, eds., (Academic Press, London, 1966).

7. S. I. Anisimov and Y. B. Zel'dovich, Sov Tech Phys Lett **3**, 445 (1977)

8. S. S. Mao, X. L. Mao, R. Greif, and R. E. Russo, "Dynamics of an air breakdown plasma on a solid surface during picosecond laser ablation," Applied Physics Letters 76, 31-33 (2000)

9. B. Angleraud, F. Garrelie, F. Tetard, and A. Catherinot, "Study of particles ejected after pulsed laser ablation of a graphite target," Applied Surface Science 139, 507-511 (1999)

10. B. Hopp, N. Kresz, C. Vass, Z. Toth, T. Smausz, and F. Ignacz, "Spatial separation of fast and slow components of pulsed laser plumes," Applied Surface Science 186, 298-302 (2002)

11. K. T. Voisey, S. S. Kudesia, W. S. O. Rodden, D. P. Hand, J. D. C. Jones, and T. W. Clyne, "Melt ejection during laser drilling of metals," Materials Science and Engineering A-Structural Materials Properties Microstructure and Processing 356, 414-424 (2003)

12. J. H. Yoo, S. H. Jeong, R. Greif, and R. E. Russo, "Explosive change in crater properties during high power nanosecond laser ablation of silicon," Journal of Applied Physics 88, 1638-1649 (2000)

13. Wen, Sybor. 2005.

14. S. H. Jeong, R. Greif, and R. E. Russo, "Numerical modeling of pulsed laser evaporation of aluminum targets," Applied Surface Science 129, 177-183 (1998)

15. E. N. Sobol, Phase Transformations and Ablation in *Laser-Treated Solids*, (John Wiley &Sons, 1994).

Chapter Five

Particle- size dependent chemistry from laser ablation of brass

5.1 Influence of particle chemistry on modern chemical analysis

Laser ablation has significant benefits for chemical anaysis [1,2]. However, the problem “fractionation” continue to be addressed [3-12] as a main concern for laser ablation of multi-element samples. Complex problems arise when laser ablation is performed on multi-component material. On top of the different particle formation mechanisms involved during laser ablation, which were discussed in chapter 3 and 4, formation of non-stoichiometric aerosol particles starts from the ablation process that is the cause of fractionation. Recent results show that particle chemical composition varies with particle size [12-16], and thus differences in particle size can influence fractionation. Thermal, physical and optical properties of samples lead to preferential vaporization of elements during laser ablation. Droplets ejected from a molten surface can contain a composition different than that from the bulk, depending on the heating rate and physical properties. Aerosol particles can form from nucleation and condensation of vapor. The chemical composition of these aerosols is likely to be different than ejected molten particles. Different size aerosols will have different entrainment and transport efficiency. Using inductively coupled plasma mass spectrometry (ICP-MS) for chemical analysis, the size of the aerosol particles influences decomposition in the ICP, differences in ionization potential for different elements can cause plasma induced fractionation[[12,17,18]]. The

above factors influence the measurement of chemical composition. Some of other effects of particles on chemical detection will be discussed in chapter 6. Studies of particle size on chemical composition from brass alloy have been reported. Jaworski [15] used a cascade impactor to collect particles; the results showed that zinc, lead and copper concentrations varied with particle size. Gunther et al reported that particles smaller than 100 nm were mostly zinc while the larger particles were mostly copper.

The purpose of this chapter is to study the relation of particle chemical composition versus particle size and purpose a model that supports mechanisms for elemental enhancement based on the results from ablation of brass alloys. Ablated particles were collected and individually analyzed using Energy Dispersive X-Ray analysis (EDAX). The gradual decrease in Zn/Cu ratio as particle size increased was measured and related to a particle formation mechanism. The purposed mechanism involves vapor and nanoparticles deposition onto larger ejected droplets.

5.2 Experimental section

The experimental system includes a Nd: YAG laser (New Wave Research, Minilase II, 5 ns pulse duration) operated at 266 nm wavelength. The pulse energy was 0.4 mJ with the beam focused to a spot size of ~200 μm, producing a fluence ~1.3 J / cm^2.

The brass sample had a zinc/copper ratio of 0.533 (Zn 35%, Cu 65%). During ablation, the aerosol particles were collected on clean silicon placed perpendicular to the sample. Particles were collected during 1~2 minutes of ablation time. Images

of these particles were recorded by scanning electron microscopy (SEM) and the chemical composition for individual particles was analyzed using Energy Dispersive X-Ray analysis (EDAX).

5.3 Result and discussion of the measured particles

SEM images of the collected particles are shown in the insert of Fig 5.1. Most particles produced by nanosecond pulsed laser ablation were spherical shaped.

Figure 5.1 shows the Zn/Cu ratio versus particle size measured using EDAX. The smallest particles are higher in zinc concentration while particles larger than 100 nm contained more than 95% copper. These data are consistent with Gunther et al, although they claimed that larger particles were pure copper.

As discussed in chapter 3 and 4, there are different mechanisms responsible for generating particles during laser ablation. Small particles can be formed by nucleation and condensation from the vapor, while larger particles may be ejected from the melted liquid due to hydrodynamic instability or recoil pressure from the expanding vapor plume. The heat of vaporization and the vaporization temperature of copper are much higher than for zinc, which makes copper more difficult to vaporize. Laser heating causes elements of higher volatility (zinc) [19] to vaporize readily, leaving a melted residue that is rich in low volatility elements (copper). Particles ejected from the melt would be expected to have a different chemical composition than the bulk, as they might be devoid of high vapor pressure elements. In contrast, particles that form by nucleation of vapor should contain the higher vapor-pressure elements. Particles formed by melt ejection or from vapor processes

occurring after they leave the surface would result in different chemical composition.

As discussed in Chapter 3.2.3, hydrodynamic sputtering is caused by cyclic heating and cooling of a surface, and is frequently observed in laser processes [20,21]. Kelly proposed that liquid droplets could be ejected from a melted sample as the acceleration of a liquid asperity (related to thermal expansion) exceeds the force holding the liquid to the surface (related to surface energy). The approximate size of ejected droplets can be derived from the following equation :

$$r_{\min} \approx \left\{ \left[\frac{6\gamma}{\rho_l} \frac{1}{\Delta L} \right] (\Delta t)^2 \right\}^{1/2} \tag{5.1}$$

$$\Delta L = 2r\alpha\Delta T + 2r(\rho_s - \rho_l)/3\rho_s \tag{5.2}$$

where $r_{\min}$ is the most probable droplet size that can be expelled, γ is the liquid surface tension, ρ_l and ρ_s are densities for liquid and solid phase respectively, α is the linear thermal expansion coefficient, ΔT is the temperature difference between surface and melting point, and Δt is the laser pulse duration τ_p minus the time at which the surface temperature reaches the melting point t_m. To estimate this time difference, the equation of temperature distribution under constant irradiance is applied [22] :

$$T(z,t) = (2A\, I_0 / k_T)\, \sqrt{\kappa t}\; ierfc\,[z/(2\sqrt{\kappa t})] \tag{5.3}$$

where z is the position from surface, A is absorption coefficient, I_0 is the laser power density, k_T is thermal conductivity and κ is the thermal diffusivity. The time

when the surface temperature (z=0) equals the melting temperature can be calculated:

$$(2A\, I_0 / k_T)\sqrt{\kappa t} = T_m \qquad (5.4)$$

From the phase diagram of Zn-Cu alloy, with a Zn/Cu ratio of 0.533 (Zn wt% =35%), the melting temperature is ~1300K. Using the laser fluence of 1.3 J / cm^2, the time required for the surface to reach the melting point was calculated to be 0.2 ns, which is small compared to the laser pulse duration of 5 ns.

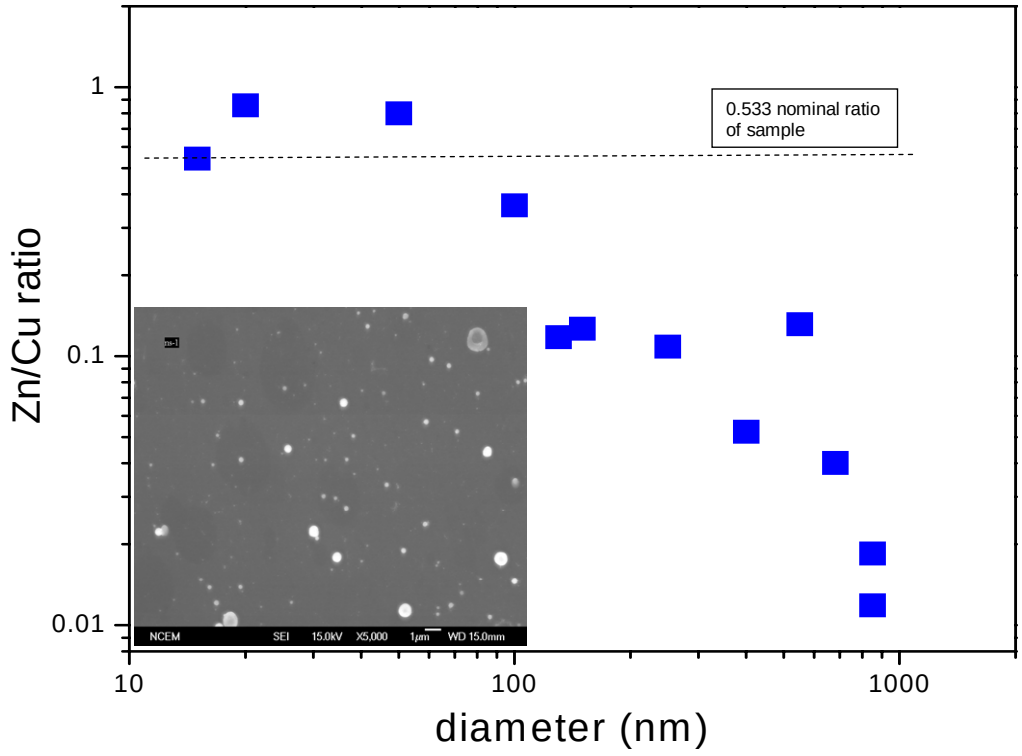

Figure 5.1 The Zn/Cu ratios of different sizes of brass particles from EDax measurement for both nanosecond and femtosecond laser ablation. Insert of Figure 5-1, different sizes of particles collected in laser ablation processes.

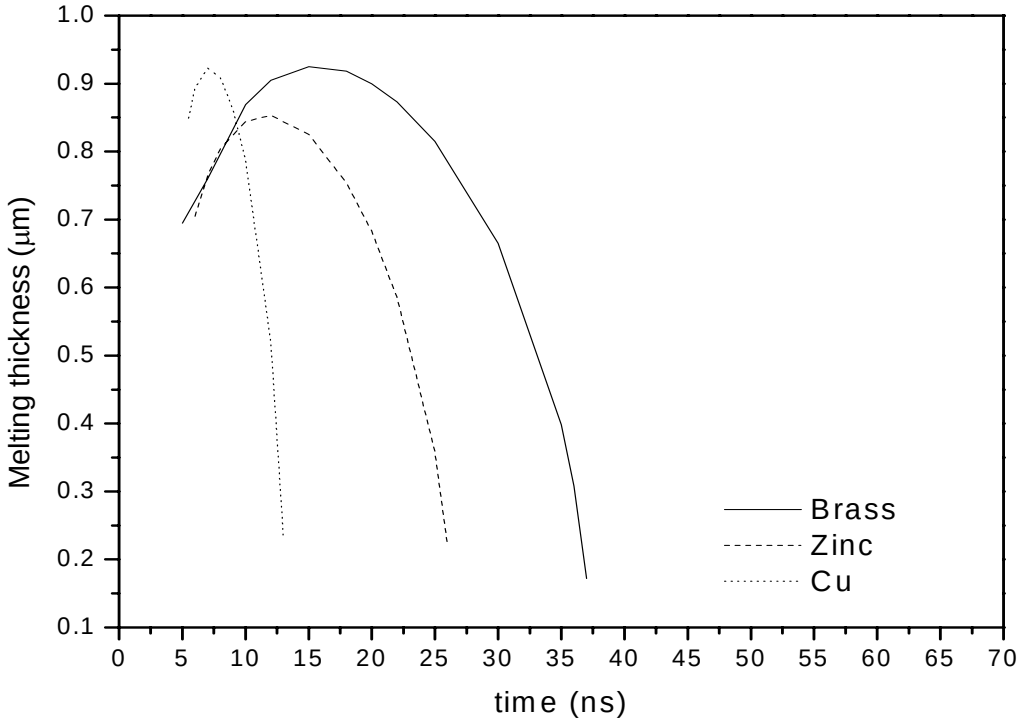

Figure 5.2 Melting thickness and temperature distribution with respect to time

The droplet size resulting from "hydrodynamic sputtering" varies with the properties of the sample material (γ , ρ_l , ρ_s , α), which are determined by the temperature and chemical composition. The composition of a melted volume may deviate from the bulk solid; thermal properties would cause preferential vaporization and a residual melt with a different composition. The disparity in surface composition may result in different sizes of ejected particles. For a 5 ns laser pulse duration with various chemical compositions (from pure copper to pure zinc) and surface temperatures, the particle sizes calculated using equation (1) were only 100~200 nm. However, larger size particles of 200~900 nm (cf. Figure 5.1) were measured. The probability of forming micron-sized particles from condensation of the vapor is small. Larger particles (~microns in size) originate from the melted liquid layer (evidenced by their spherical shape), formed by cavitations of the melt from the surface by recoil pressure (spallation) . The size of these particles is limited by the thickness of the melted volume. Assuming that the laser intensity is constant with time, the temperature distribution after the laser pulse is [22]:

$$T(z,t>\tau_p)=\frac{2A\,I_o\,\kappa^{1/2}}{k_T}\left[t^{1/2}\;ierfc\left(\frac{z}{2(\kappa\,t)^{1/2}}\right)-(t-\tau_p)^{1/2}\;ierfc\left(\frac{z}{2[\kappa\,(t-\tau_p)]^{1/2}}\right)\right] \qquad (5.5)$$

The melted thickness z_m can be determined by setting the temperature from equation (5) equal to the melting temperature at a given time t. The relation of melt thickness z_m for copper, zinc and brass with time is plotted in Figure 5.2. The maximum melt depths were ~900 nm at about 10- 20 ns after the laser irradiates the

surface. The estimated thickness of the melted region coincided with the largest particles we measured in the SEM images. The temporal temperature variation at different z location is also plotted at Figure 5.3.

The variation in chemical composition versus size indicates that there may be an interaction between particles produced by the two different mechanisms. We propose that deposition of smaller condensate particles or vapor on the surface of ejected droplets is the reason for this trend. Figure 5.4 illustrates this concept: vaporized atoms and ions condense as tiny particles on the ejected larger droplets, forming an outer layer. Recent results provide support for this basis. Bleiner et al [23] used a focused ion beam (FIB) to cut ablated silicon particles. Two different regions were observed from the cross section; a corona was found around the core. The loose and irregular structure of the corona indicated that it was formed by deposition of vapor or nano particles on the surface of the core, while the core originated from the molten state.

For this model, the thickness of the outer layer was assumed to be the same for all particles. Therefore, the volume change in percentage of the original volume would be smaller for a large droplet than a small one (Fig 5.4 d). The densities and chemical composition were different for the core of a particle (radius R and Zn/Cu mass ratio $\gamma_{core,zn/cu}$) than for the outer layer of the particle (thickness dR and Zn/Cu mass ratio $\gamma_{outer,zn/cu}$). The subscript *core, outer* and *tot* represent the core droplet, condensation outer layer and total particles, respectively. Adding the

copper and zinc mass separately for the two regions yields an "overall" Zn/Cu molar ratio according to

$$\gamma_{tot,zn/cu} = \frac{m_{tot,zn}}{m_{tot,cu}} \frac{\overline{M}_{cu}}{\overline{M}_{zn}} \tag{5.6}$$

where m denotes the mass, $\overline{M}$ is the atomic weight and γ is the molar ratio of the two elements.

For binary liquid metal alloys, the volume is approximately the sum of the two original metal volumes [24]; thus we can use the volume occupied by the individual element for calculations to obtain total volume according to

$$V_{cu} + V_{zn} = V_{tot} \tag{5.7}$$

For a given Zn/Cu mass ratio $\gamma_{zn/cu}$, the ratio of copper and zinc in the total volume is calculated as

$$\frac{V_{cu}}{V_{tot}} = \frac{1}{1+\gamma_{zn/cu}\dfrac{\rho_{cu}}{\rho_{zn}}} \quad \text{and} \quad \frac{V_{zn}}{V_{tot}} = \frac{\gamma_{zn/cu}\dfrac{\rho_{cu}}{\rho_{zn}}}{1+\gamma_{zn/cu}\dfrac{\rho_{cu}}{\rho_{zn}}} \tag{5.8}$$

where ρ is the density of the metal.

The volume of the droplet and the change of volume can be represented as

$$V_{tot} = \frac{4}{3}\pi R^3, dV_{tot} = \frac{4}{3}\pi(R+dR)^3 - \frac{4}{3}\pi R^3 \tag{5.9}$$

For a given outer layer thickness dR, the mass of Zn and Cu was added separately from the core and the outer layer using the following equation

$$m_{tot,cu} = m_{outer,cu} + m_{core,cu}; m_{tot,zn} = m_{outer,zn} + m_{core,zn} \tag{5.10}$$

The molar Zn/Cu ratio, cf. equation (5.6), can be solved giving the Zn/Cu ratio in the core particles and the vapor.

The evaporation rate per unit area for the two elements (Zn or Cu) can be written as:

$$J_x = P_x \sqrt{\frac{M_x}{2\,\pi\, k_B\, T}} \tag{5.11}$$

where M_x is the mass of the atom, k_B is the Boltzmann constant, P_x is the vapor pressure and the temperature distribution T is a function of time, which can be calculated through equation (5.5) with a given laser irradiance I_0. Thus the ratio of vaporized Zn to Cu is calculated as

$$R_{Zn/Cu} = \frac{C_{zn}\ J_{zn}}{C_{cu}\ J_{cu}} \tag{5.12}$$

where C is the mole fraction of the brass sample and the subscripts Zn and Cu indicate the components (0.35 for Zn and 0.65 for Cu). The detailed equations are reported elsewhere [19]. The nanosecond pulsed laser was operated at a power density ~ $0.3\,GW/cm^2$. The sample surface temperature during laser ablation can reach several thousand degrees. If we assume that the mole ratio of the melted liquid remains constant during evaporization process, then the calculated Zn/Cu ratio in vaporized atoms based on equation (5.12) will be more than 10^3 and the vapor will be almost pure zinc. However, the vaporization rate of Zn is much higher than Cu initially, thus the mole fraction of zinc decreases and the mole fraction of copper increases. Therefore the net result is that zinc in the melt layer is quickly depleted whereas copper evaporates more slowly. The total vaporized

Zn/Cu ratio will be much lower then calculated directly from equation (5.12). Previous results from our group found that the zinc to copper ratio was proportional to the inverse of the laser power density in the low power density regime. At a power density of $0.3\,GW/cm^2$, the Zn to Cu ratio in the vapor was measured to be approximately 1. Thus, the Zn/Cu vapor ratio in the model $\gamma_{outer,zn/cu}$ was chosen as 1. The Zn/Cu ratio of the melted layer is assumed to be constant after the initial depletion of zinc, i.e. the ejected droplets have the same composition regardless of their size. The Zn/Cu ratio for the ejected particles $\gamma_{core,zn/cu}$ was set as 0.01, which corresponds to the ratio we measured from micron-size particles.

Figure 6.4 shows the calculated data for Zn/Cu ratio with particle sizes from 50 nm to $1\,\mu m$. The thermal properties were taken to be the values at 300K. A constant thickness for the deposited layer on different sized core droplets was assumed to be 10 nm. Nano particles were observed frequently and reported to be the size of several nanometers, these particles were believed to be formed from vapor condensation. The model agrees well with the data and provides a basis for the explanation that vapor deposition on the surface of larger particles influences the Zn/Cu ratio change versus particle size.

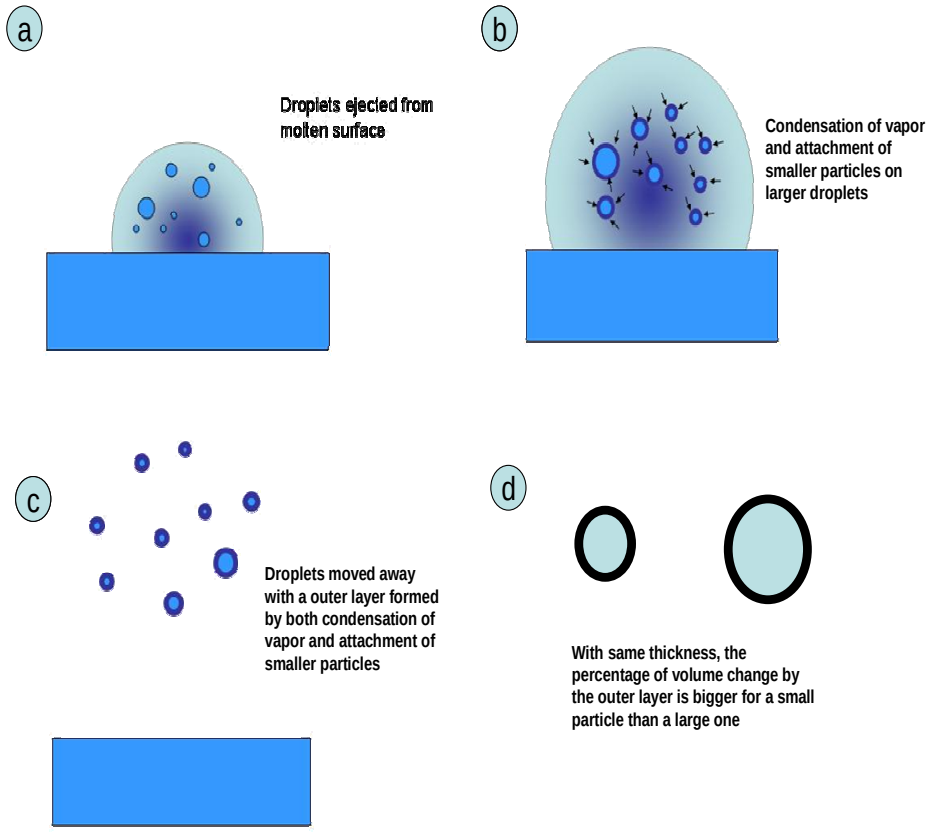

Figure 5.3 Conceptual illustration of the deposition of smaller entities on larger droplet particles during laser ablation

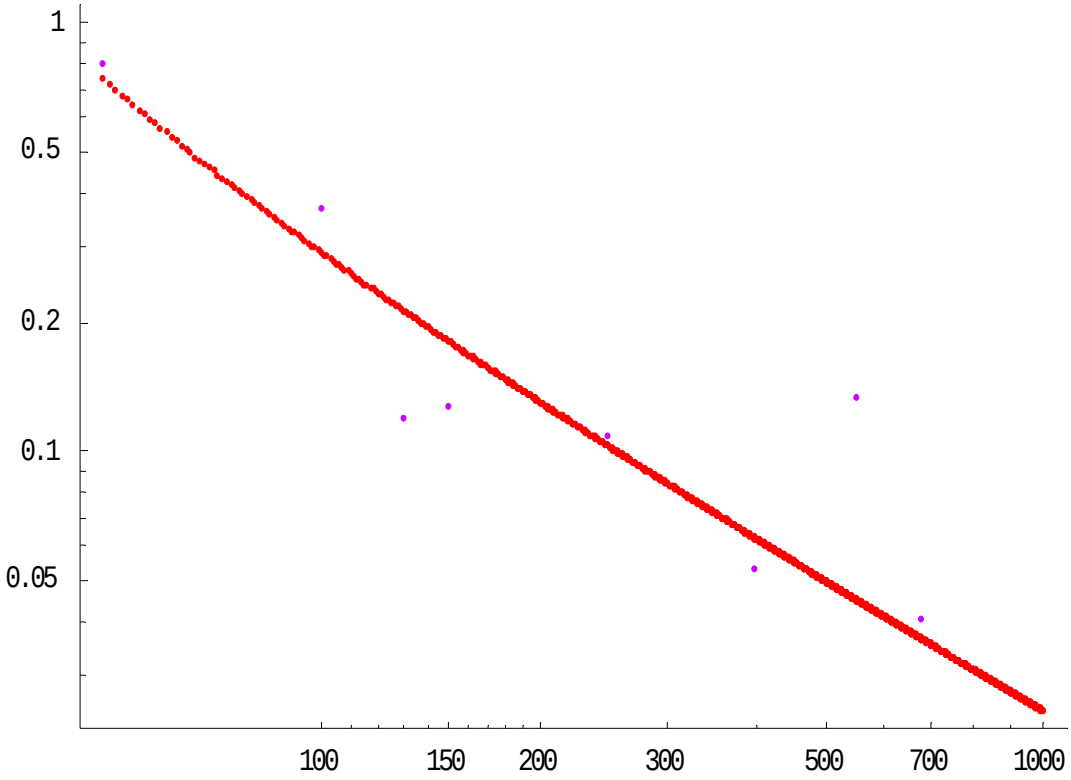

Figure 5.4 Calculated results of the Zn/Cu ratio versus particle size based on the attachment model

The model does not consider temperature and plasma effects. The laser-induced plasma can interact with the surface and cause thermal heating after the laser pulse. Also, the ejection of particles into the high temperature plasma would cause further vaporization of Zn and favor the condensation of Cu. Hence the resulting droplet would be more Cu enriched compared to the case of ejection without subsequent deposition.

The assumption of a constant thickness of outer layer needs to be examined further. When an aerosol undergoes condensation in the vapor, the growth rate of the volume can be estimated from [25]:

$$I(v,t) = \frac{\partial V}{\partial t} = B\,(S-1)V^{1/3} \qquad (5.13)$$

where V is aerosol volume, B is a coefficient and S= p_v / p_s which is the ratio of actual and saturation vapor pressure. Rewriting equation (5.13) in terms of radius r:

$$\frac{\partial r}{\partial t} \propto r \qquad (5.14)$$

Integrating of equation (5.14) and assuming that the radius change is not large, i.e. the thickness of the deposition layer is smaller than the droplet radius, and we get the relation $\Delta r \propto \Delta t / r$. The increase in particle radius is inversely proportional to the original radius. Radius increase will be larger for small aerosols than a large aerosol particle. Hence a small particle should be more zinc enhanced while large particles will be more copper dominant, and the trend that copper concentration increased with particle size is explained by the two layer model.

5.4 Summary

Investigation of laser ablated particles from brass alloy yielded the relation between particle size and chemical distribution. Larger particles contained more copper and smaller particles contained more zinc and concentration of copper increased as the particle size increased. A two-region particle model can explain this that zinc enriched vapor condensation on copper enriched ejected droplets. Except the fractionations originated from the particle generation mechanisms, the interactions between larger particles and smaller particles may further complicate the relations of particle size and chemistry composition.

References

1. R. E. Russo, Applied Spectroscopy 49, A14-A28 (1995)
2. P. Arrowsmith and S. K. Hughes, Applied Spectroscopy **42**, 1231-1239 (1988)
3. M. L. Alexander, M. R. Smith, J. S. Hartman, A. Mendoza, and D. W. Koppenaal, Applied Surface Science **129**, 255-261 (1998)
4. O. V. Borisov, X. L. Mao, and R. E. Russo, Spectrochim. Acta Pt. B-At. Spec. **55**, 1693-1704 (2000)
5. Eggins S.M, L. P. J. Kinsley, and Shelley J.M.G, Appl. Surf. Sci. **127-129**, 278-286 (1998)
6. J. Gonzalez, X. L. Mao, J. Roy, S. S. Mao, and R. E. Russo, Journal of Analytical Atomic Spectrometry **17**, 1108-1113 (2002)
7. M. Guillong, Kuhn H-R, and D. Gunther, Spectrochim. Acta Pt. B-At. Spec. **58**, 211-220 (2003)
8. Kosler J., H. P. Longerich, and Tubret M.N., Anal Bional Chem **374**, 251-254 (2002)
9. H. C. Liu, O. V. Borisov, X. L. Mao, S. Shuttleworth, and R. E. Russo, Applied Spectroscopy **54**, 1435-1442 (2000)
10. R. E. Russo, X. L. Mao, O. V. Borisov, and H. C. Liu, Journal of Analytical Atomic Spectrometry **15**, 1115-1120 (2000)
11. M. E. Taylor, D. L. Blaney, and G. Cardell, Appl. Surf. Sci. **V165**, 166-177 (2000)

12. M. Guillong and D. Gunther, Journal of Analytical Atomic Spectrometry **17**, 831-837 (2002)
13. D. J. Figg, J. B. Cross, and C. Brink, Appl. Surf. Sci. **127-129**, 287-291 (1998)
14. H. R. Kuhn and D. Gunther, Analytical Chemistry **75**, 747-753 (2003)
15. R. Jaworski, E. Hoffmann, and H. Stephanowitz, International Journal of Mass Spectrometry **219**, 373-379 (2002)
16. P. M. Outridge, W. Doherty, and D. C. Gregoire, Spectrochimica Acta Part B-Atomic Spectroscopy **52**, 2093-2102 (1997)
17. B. Kozlov, A. Saint, and A. Skroce, Journal of Analytical Atomic Spectrometry **18**, 1069-1075 (2003)
18. S. H. Jeong, O. V. Borisov, J. H. Yoo, X. L. Mao, and R. E. Russo, Analytical Chemistry **71**, 5123-5130 (1999)
19. X. L. Mao, A. C. Ciocan, and R. E. Russo, Applied Spectroscopy **52**, 913-918 (1998)
20. R. L. Webb, J. T. Dickinson, and G. J. Exarhos, Appl. Spectrosc. **51**, 707-717 (1997)
21. R. Kelly and J. E. Rothenberg, Nuclear Instruments & Methods in Physics Research Section B-Beam Interactions with Materials and Atoms **7-8**, 755-763 (1985)
22. A. M. prokhorov, V. I. Konov, I. Ursu, and I. N. Mihailescu, *laser heating of metals*, 1990).

23. D. Bleiner and P. Gasser, Applied Physics A-Materials Science & Processing **79**, 1019-1022 (2004)
24. T. Iida and R. I. L. Guthrie, *The Physical Properties of Liquid Metals,* (Clarendon press, Oxford, 1988).
25. M. M. R. Williams and S. K. Loyalka, *Aerosol science - theory &practice,* (Pergamon Press, 1991).

Chapter Six

Applications: Effects of particle size in ICP-MS detection

6.1 Introduction

Using laser ablation as a tool for real time chemical detection in multi-element materials is an important application. While chemical detection can be achieved by both AES (atomic emission spectroscopy) and MS (mass spectroscopy) methods, observations of emission spectrum usually cannot provide repeatable and accurate results. Although MS can provide improved data, however the accuracy and precision are largely influenced by the particle size distribution. As discussed in chapters 5, chemical composition results depend on the size of the particle and errors (spikes) increase when large particles are generated. This chapter discusses the effects of particle size on the performance of ICP-MS. Three approaches will be discussed in the following sections. Femtosecond (fs) laser ablation generated smaller particles compared to nanosecond (ns) laser ablation. So the study of fs vs. ns laser ablation results to the generation of different particle size distributions. After a particle aerosol is generated by laser ablation, we can either select certain sizes or break down large particles using another laser. These two methods enable us to observe the effects of particle size within already generated particles by either filtering the particle size or altering the size distribution.

6.2 Different particle size distribution by using ns or fs lasers

Experimental section

The experimental configuration and conditions were discussed in chapter 2.4. Here the ablated mass was transported by argon gas out of the sample chamber with a 0.8 LPM (Liter per minute) flow rate. The particles were delivered into the ICP-MS (Thermoelemental, PQ3) for chemical analysis. Ablation was continuous for three minutes during ICP-MS measurements.

Results and Discussion

Bulk brass with zinc to copper ratio of 0.18 was ablated using both ns and fs lasers for 180 seconds while recording the elemental signal intensity in the ICP-MS. The temporal intensity variation for copper and zinc are shown in Fig 6.1 (a) and (b). Ablation by fs laser pulses produced Zn and Cu elemental signals that were more than 10 times greater than ns laser ablation at the same fluence. Large instantaneous spikes were measured for ns ablation along with greater intensity fluctuations (relative standard deviation). Since the ICP-MS intensity is proportional to the amount of mass, higher intensity means more mass was delivered into the ICP torch using femtosecond pulses. Part of the increase in intensity can be explained by the increased quantity of mass ablated. From crater measurements (Fig 6.2), the volume removed for femtosecond ablation was approximately 10 times larger than for the nanosecond case. However, the differences in intensity and spikes are also related to the aerosol particle size distribution. As previously discussed in chapter 3, particle size and shape are different from ns and fs laser ablation. The sizes of particles from nanosecond ablation ranged widely from several tens to thousands of nanometers. The ‘large’

particles from femtosecond ablation were agglomerates of smaller particles. The primary particles were the size of 100-200 nanometers, which were connected to each other by chains having dimension of about several nanometers in diameter. There were no single large droplets like those observed with nanosecond ablation, suggesting that melting and ejection of molten mass is less prominent with femtosecond ablation. Though large agglomerates were formed during femtosecond ablation, they likely will be easier to break up into smaller primary particles, and digested completely in the ICP compared with the large primary particles formed with nanosecond ablation. ICP-MS intensities and crater volume measurements were greater for femtosecond ablation versus nanosecond ablation.

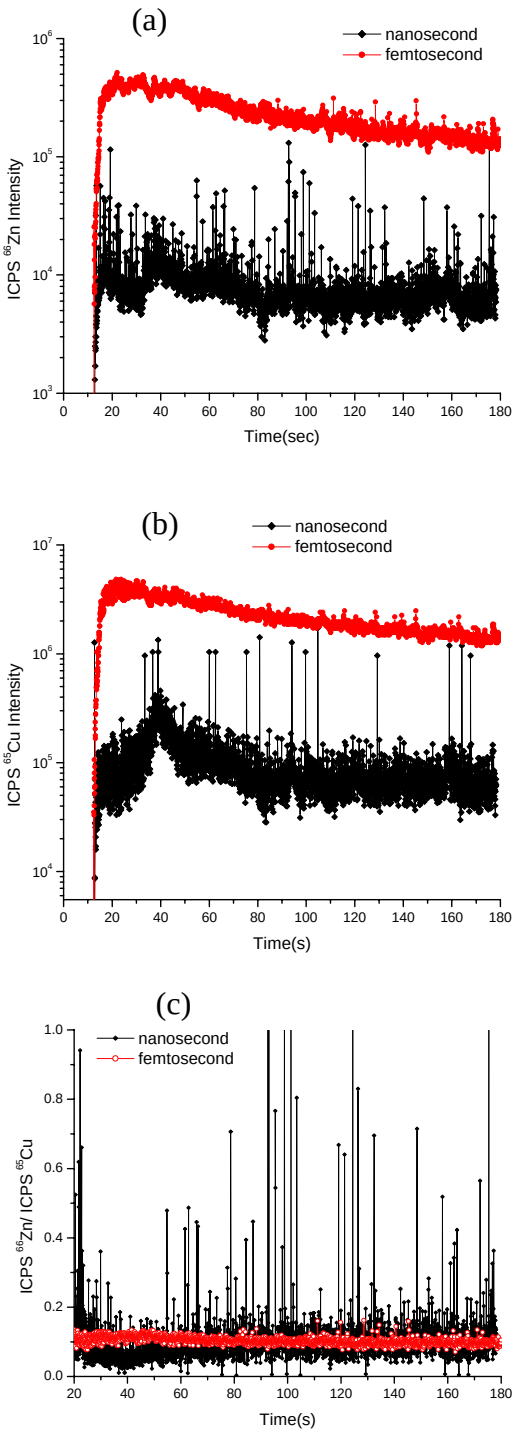

Figure 6.1 ICP-MS intensity of ^{66}Zn and ^{65}Cu and ratio of $^{66}Zn/^{65}Cu$ with different pulse widths. Square represents nanosecond results, open circle represents femtosecond results

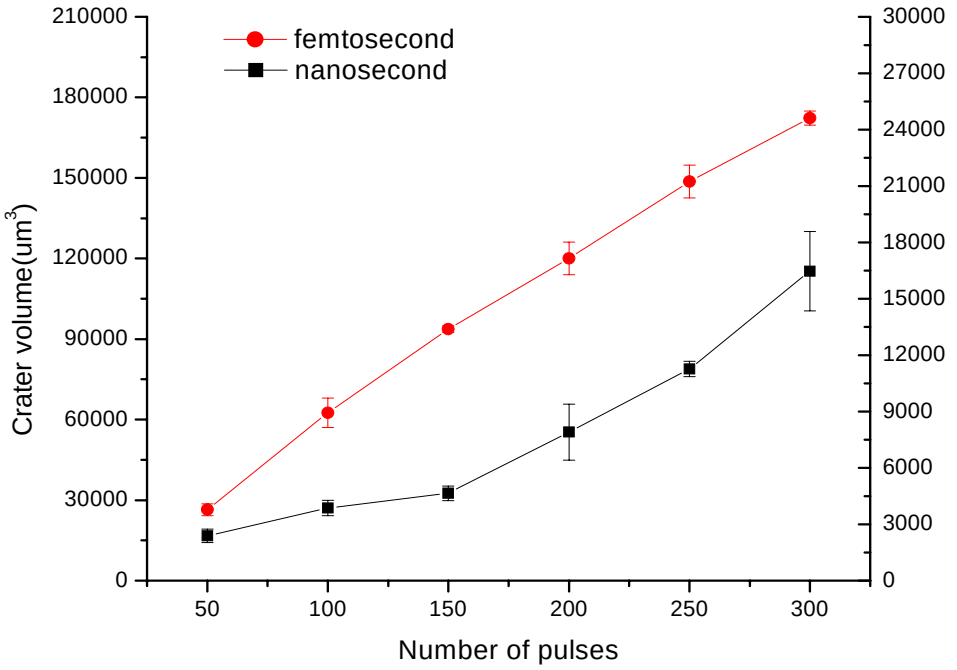

Figure 6.2 Crater volume of brass sample for two different pulse-widths. Square represents nanosecond results, solid circle represents femtosecond results

Observing the temporal intensities of copper and zinc, it is found that there are more spikes in the zinc signal than copper. Spikes were reported previously for zinc but not for copper [1]. In recent studies, zinc was found to be enriched with smaller particles while for copper large particles were primarily present [1-6]. As large particles enter the ICP, the thermal characteristic of zinc makes it easier to evaporate than copper. The vaporized zinc can form a high concentration cloud and generate more spikes even if the zinc concentration is lower in the larger particles. Copper, compared with zinc, is difficult to evaporate and thus a lower amount of mass can be vaporized and detected by the ICP-MS for large particles. The signal level for zinc was much lower than copper, making larger particle effects and spikes more prevalent for low zinc concentration. Even though the energy stability (relative standard deviation, RSD) of the femtosecond laser (5%) was worse than the nanosecond laser (2%), improved analytical performance was obtained by using fs laser ablation. The spikes were effectively eliminated, the intensity showed less time-dependence, the signal was more than 10 times greater, and the precision was better for fs ablation.

The advantage of fs ablation for chemical analysis is further demonstrated by observing the $^{66}Zn/^{65}Cu$ ratio in Fig 6.1(c). The zinc to copper ratio of the bulk brass was 0.18. Considering the actual isotope abundance of each element (^{65}Cu with 30.83% and ^{66}Zn with 27.9%), the $^{66}Zn/^{65}Cu$ ratio was corrected to be 0.16. The ratio for ns ablation ranged from 0.05 to 0.2, excluding the extraordinary data points (spikes on the data). The ratio was significantly improved for fs ablation

($^{66}Zn/^{65}Cu$=0.11±0.01) and was constant during the entire sampling period. This improved precision, accuracy and elimination of spikes makes fs ablation very encouraging for chemical analysis applications.

Similar trends were observed for other brass alloys. Five brass samples with Zn/Cu ratios varying from 0.06 to 0.65 were ablated using both ns and fs lasers. The calculated RSDs from the integrated temporal (120 pulses for each sampling period) signal response are shown in Fig 6.3. For ns experiments, the RSD was as large as 120% while the fs results showed smaller RSD values, about 10% independent of zinc/copper ratio. The ablation threshold, reflectivity, aerosol particle size distribution, and melting all contribute to this matrix dependence. The RSD for nanosecond ablation is particularly influenced by changes in the ablation behavior versus sample matrix. For example, low zinc concentration brass is less volatile and more difficult to ablate using ns pulses. A large portion of the aerosol mass may be in the form of larger droplets. Femtosecond laser ablation is significantly less influenced by the sample properties.

ICP-MS detection also contributes to this error. The quadrupole MS uses the scanning method to measure one element at one time. Dwell time for each scan time was 10 ms. Therefore, the quadrupole detected ^{63}Cu, ^{64}Zn, ^{65}Cu and ^{66}Zn sequentially. For a similar experiment [7] where the flow rate was 1.0 Lt/min (which is equivalent to a flow velocity of 27m/s), it was observed that the ion cloud in ICP was about 100 microns in diameter. The time duration for this cloud to pass was about 3×10^{-6} s, which is much smaller than the 10 ms dwell. When a large

particle enters the ICP and fractionates during its resident time, all the elements are not detected simultaneously and the ratio of elements would be erroneous. Femtosecond ablation demonstrated an error independent of matrix effects where the RSD remained at 10%. The narrower particle size distribution and smaller particles produced by fs ablation reduce the error associated with particle fractionation in the ICP.

Lower zinc intensity from nanosecond ablation of low zinc concentration samples is not the cause of increased error. The RSD in zinc intensity increased from 28% to 77% as intensity counts dropped only one third from 20000 to 14000. When the RSD increased from 77% to 90%, the intensity dropped from 14000 to 7000. Also, the zinc intensity for nanosecond ablation was well above the background intensity. When the zinc intensities were of similar value (28000 for femtosecond from 0.06 Zn/Cu ratio brass, 22000 for femtosecond from 0.533 Zn/Cu brass), the RSD of the zinc intensity for the femtosecond laser was much smaller (18%) than from the nanosecond laser (90%). The variation with matrix dependence is due to the difference in pulse-width, with the fs laser providing smaller particles and a narrower particle size distribution than the ns laser.

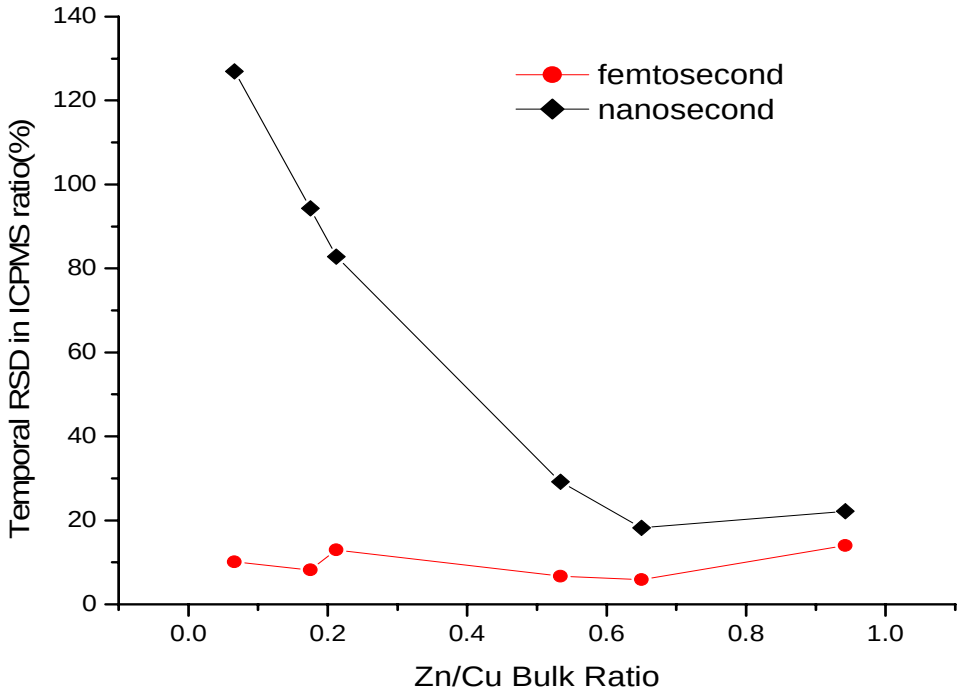

Figure 6.3 RSD for two different pulse-widths with respect to change of bulk Zn/Cu ratio. Square represents nanosecond results, solid circle represents femtosecond results

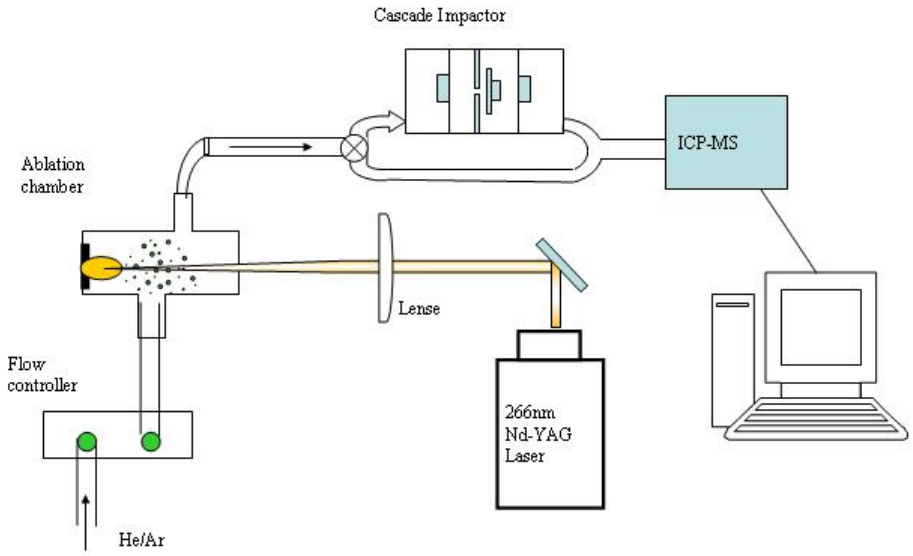

Figure 6.4 Experiment setup for laser ablation using a cascade impactor

6.3 Filtering particles using a cascade impactor

Experimental system

The experimental system is presented in Fig 6.4. A frequency quadrupled UV (266 nm wavelength) Nd: YAG laser was operated at a 10Hz pulse repetition rate. Brass alloy with nominal zinc/copper mass ratio of 0.533 was used as the sample. Three to four locations on the sample were ablated repetitively for two minutes each to generate the temporal response in the ICP-MS. Four isotopes (^{63}Cu, ^{64}Zn, ^{65}Cu and ^{66}Zn) intensities were recorded sequentially using a quadrupole mass spectrometer,

but only the main isotopes of each element (^{65}Cu and ^{66}Zn) were used in the discussion. Argon was used as the carrier gas.

A Cascade impactor (PIXE International Corp) was used as a selective low-pass filter; particles with diameters smaller than the selected cutoff size pass through to the ICP. The cascade impactor was connected in-line between the ablation chamber and the ICP-MS. The impactor collected particles on different stages via different orifice sizes. The effective 50% cutoff diameter of the impactor was a function of flow rate, gas viscosity and aerosol density. The cutoff diameter was established using eight stages to be from 25 nm to 3360 nm. However, the two smaller diameters (25nm, 52nm) were not used due to pressure build-up in the ablation chamber. ICP-MS data with and without the impactor were compared by using a bypass switch.

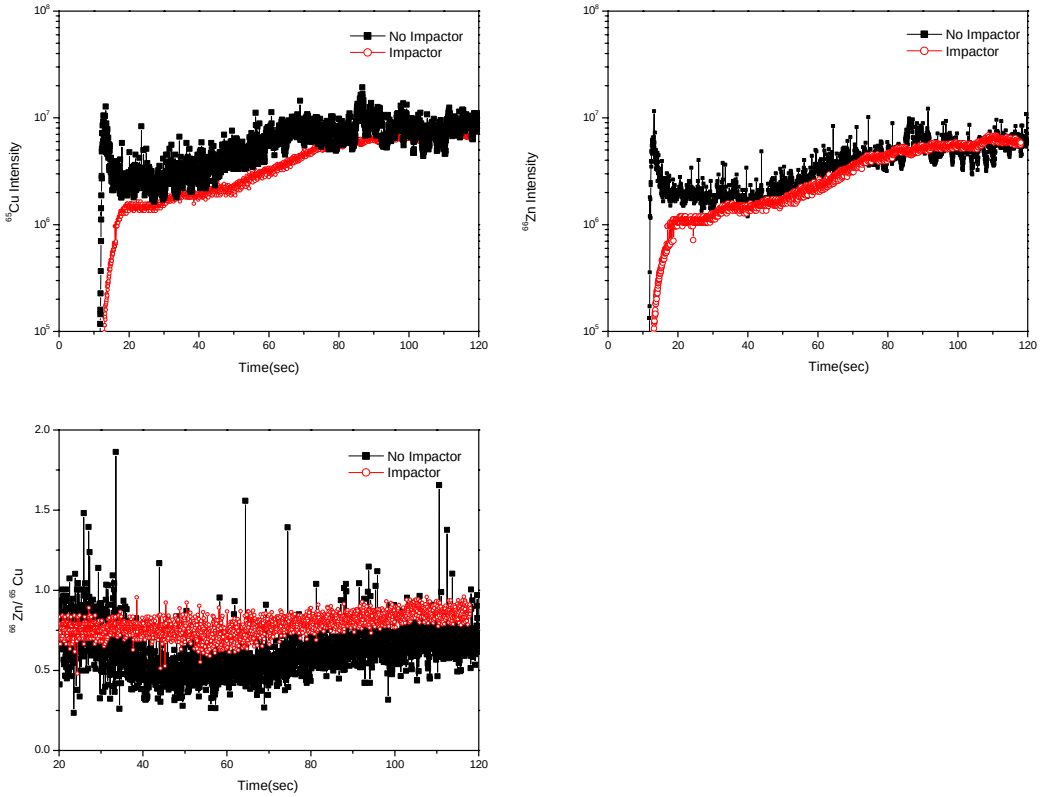

Figure 6.5 ICP-MS temporal signal with and without impactor (100nm low pass cutoff diameter): a) ^{65}Cu; b) ^{66}Zn c) ^{66}Zn/^{65}Cu Ratio

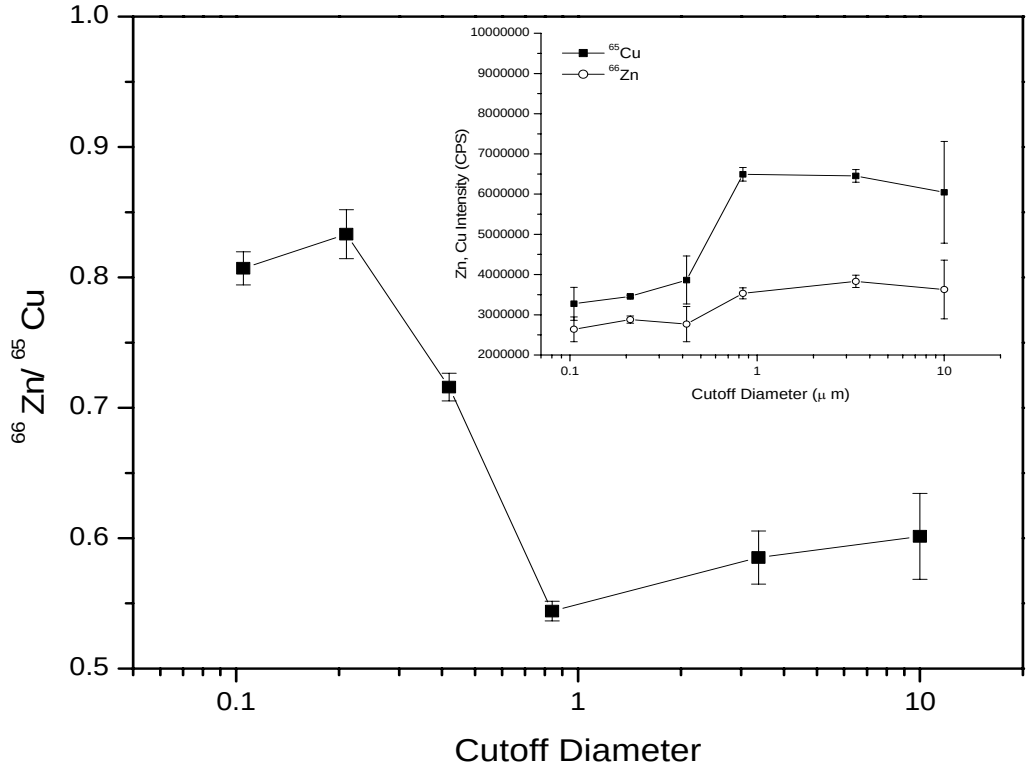

Figure 6.6 Integrated Cu 65, Zn 66 intensity and Zn/Cu ratio versus low pass cutoff diameter

Results and discussions

Fig 6.5 shows the temporal signal intensity for ^{65}Cu, ^{66}Zn and the $^{66}Zn/^{65}Cu$ ratio obtained with and without the impactor. The long-term Cu and Zn responses represent the change in mass ablation rate as the crater develops. The short-term intensity fluctuations and spikes on the temporal response are due to the particle size distribution reaching the ICP-MS. These short-term fluctuations and spikes were eliminated using the impactor with a cutoff size of 105 nm. Also, using the impactor eliminated the large intensity observed at the beginning of 266 nm laser ablation. With the impactor, the elemental temporal ratio ($^{66}Zn/^{65}Cu$) was uniform

and at a higher value than the ratio without the impactor. Using the impactor with a cutoff size larger than 3.36 microns, no differences were found in either the temporal intensities or temporal ratio compared to the data measured without the impactor.

A drop in signal intensity was measured with decreasing cutoff sizes of the impactor (Fig 6.6). Copper and zinc intensities decreased as the impactor cutoff diameter was decreased. From 1 to 0.2 micron cutoff diameter, copper intensities dropped by more than 50% while zinc intensities dropped by about 30%. The $^{66}Zn/^{65}Cu$ ratio changed from ~0.6 to ~0.8. These data support previous studies that smaller particles have higher Zn/Cu ratios [8]. This is also an indirect proof that particle chemistry change with its size as discussed in chapter 4. The correct Zn/Cu ratio was not established for this work. An in-depth calibration procedure would be required to ensure that the ICP-MS was optimized for each particle size. The measured changes in ratios represent contributions from changes in the ICP-MS performance as well as differences in the particle chemistry versus size.

The external precision (reproducibility of analysis for spot to spot ablation on the brass sample) for the $66Zn/^{65}Cu$ ratio improved to approximately 2% by using the smallest (105 nm) cutoff diameter of the impactor (Figure 6.7). This improvement in external precision is due to the improved stability of the temporal response. In this work, internal precision is defined as the temporal relative standard deviation (TRSD) measured during repetitive pulsed sampling. Calculation of the temporal relative standard deviation shows the improvement in performance. The temporal

ICP-MS signals were averaged using 15 adjacent points to produce a smoothed signal. The difference between the smoothed and original signals is related to the noise due to the wide particle size distribution. The calculation of TRSD is:

$$S_i = \frac{1}{15}\sum_{j=1}^{15} X_{i-8+j} \tag{6.1}$$

$$E_i = X_i - S_i \tag{6.2}$$

$$\overline{E}_o = \frac{1}{n}\sum_{i=1}^{n} E_i \tag{6.3}$$

$$\%TRSD = \left(\frac{\frac{1}{\sqrt{n-1}}\left(\sum_{i=1}^{n} \sqrt{\left(E_i - \overline{E}_0\right)^2} \right)}{\frac{1}{n}\sum_{i=1}^{n} X_i} \right) * 100 \tag{6.4}$$

The smoothed signal S_i is calculated using equation (6.1), and then the error E_i is calculated as the difference between the original temporal signal X_i and the smooth signal S_i using equation (6.2). The average of the error $\overline{E}_o$ is calculated in equation (6.3). Finally, the temporal relative standard deviation is calculated using equation (6.4), where $\frac{1}{n}\sum_{i=1}^{n} X_i$ is the integrated temporal signal. n is the number of points used in the smoothing process from 20 seconds to 120 seconds.

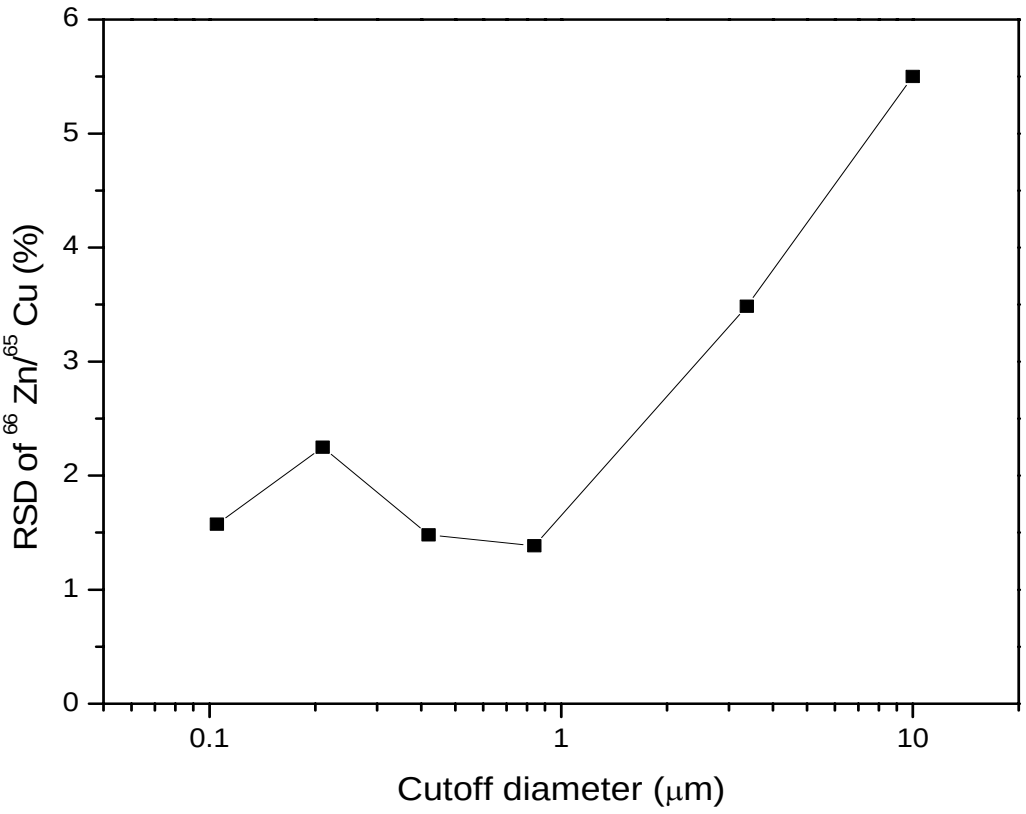

Figure 6.7 Relative standard deviation (%RSD) for ^{66}Zn/^{65}Cu Ratio versus cutoff diameter

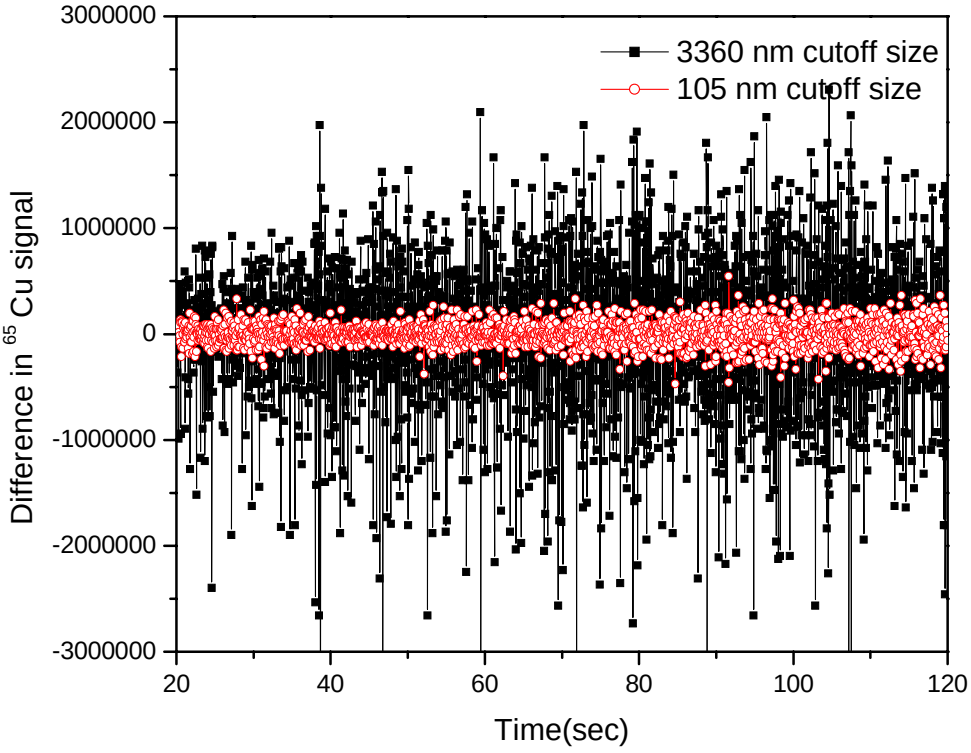

Figure 6.8 Temporal Cu signal difference between original and smoothed ICP-MS intensity

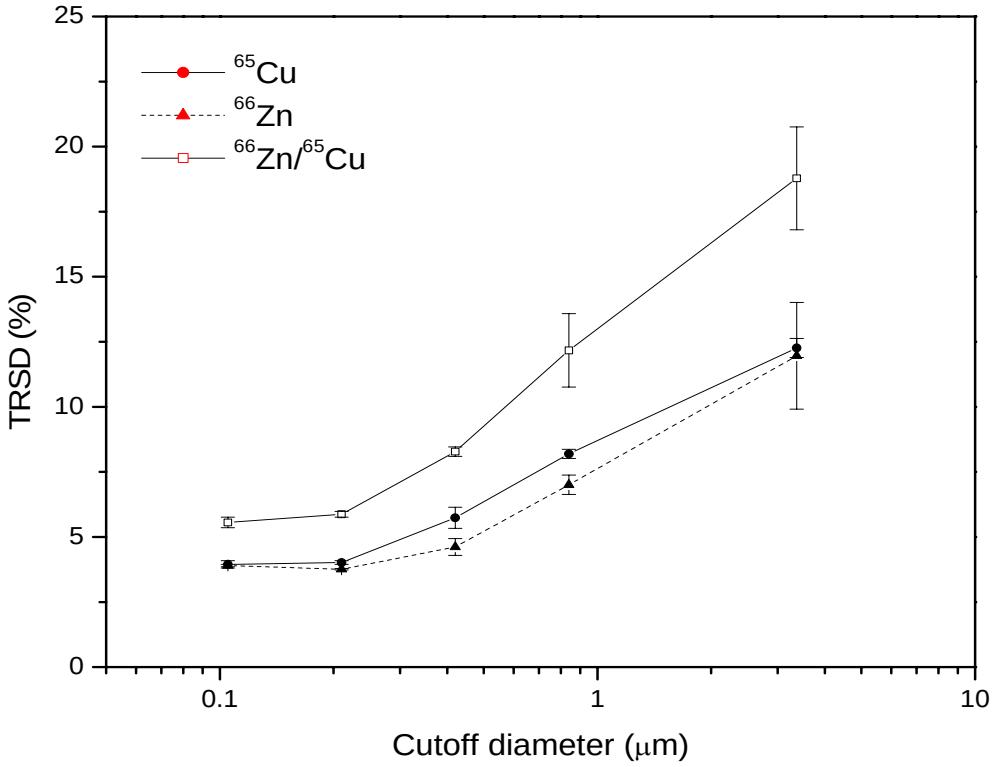

Figure 6.9 Temporal RSD (TRSD) for ^{65}Cu and ^{66}Zn intensity and their ratio versus cutoff diameter

Temporal signal differences for ^{65}Cu intensity and ^{66}Zn/^{65}Cu ratio using two impactor cutoff diameters (105 nm, 3360 nm) are shown in Fig 6.8. The effect of larger particles is demonstrated in these data. The temporal relative standard deviation (Figure 6.9) decreased from approximately 20% to 4% as the particle size distribution was narrowed using the impactor with the 105 nm cutoff. Randomly appearing larger particles were difficult to vaporize completely in the ICP while produce the unwanted spikes in the signals. Filtering out these big particles using the in-line impactor prevents the spikes and is effective in improving both the external and internal precision of laser ablation sampling. As shown in Figure 6.6, this improvement in precision is accompanied by a change in elemental ratio.

Further studies are needed to calibrate the ICP-MS and determine the conditions for optimum precision and accuracy.

An in-line cascade impactor was successful in eliminating fluctuations in ICP-MS intensities caused by large particles, improving the precision. The fluctuations (spikes) on the temporal signals were attributed to particles larger than about 0.2 micron. Signal precision was improved by filtering out large particles; however the chemical characteristics of the filtered products changed with respect to particle sizes. Chemical composition can be altered by choosing different particle size output, which should be taken into account using laser ablation for sampling into an ICP-MS.

6.4 Altering size distribution using a second laser to fracture particles

Experimental

The research was performed using a dual pulsed Nd:YAG laser (Solo-PIV laser, New Wave Research) for ablation with sample introduction to an ICP-MS (VG PQ3). The solo PIV laser has two collinear 266nm beams from two laser heads mounted on a single base plate. The beams share the same light path to a fourth harmonic generator. Each beam has the same diameter, energy, and pulse duration. The separation time between pulses from the two laser heads was controlled using a delay generator (Stanford Research System Inc. Model DG535); the delay could be changed from nanoseconds to several seconds.

The brass sample comprised 51.48% copper (Cu) and 48.52% zinc (Zn). The polished sample was placed in a chamber where both laser beams were focused to a spot size of ~ 40μm with a fluence of 150 J/cm^2. The ablation was performed in an argon environment. Three positions on the sample were ablated for each delay time between the two lasers pulses. The ICP-MS signal intensity and temporal relative standard deviation were measured for each sample position and delay time. Crater volumes were measured using a white light interferometer microscope (Zygo 200) to relate changes in ICP-MS performance to the ablated mass quantity.

The ejection of particles from the sample surface was imaged using a time-resolved shadowgraph system as shown in Fig 6.10 which was discussed in previous chapters.

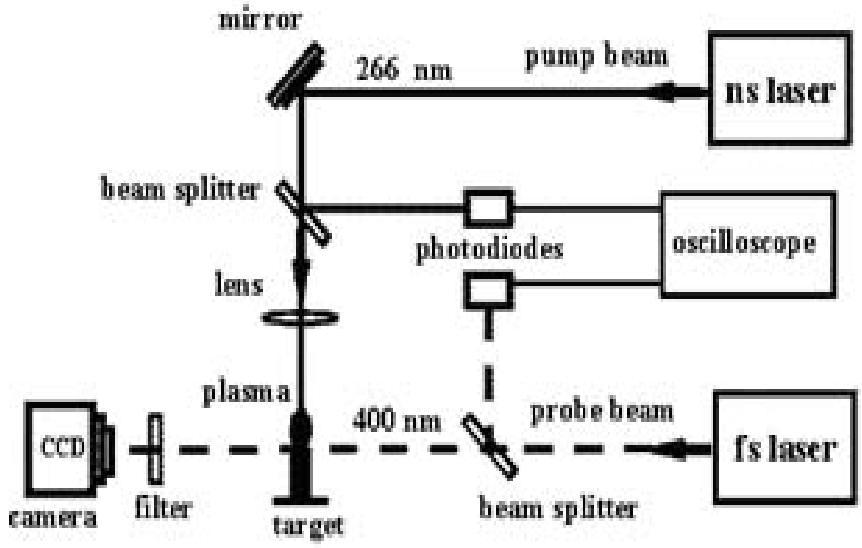

Figure 6.10 Time-resolved shadowgraph imaging system

Results and Discussion

A second laser beam was delayed in time to fracture large particles produced by the primary laser ablation pulse, thereby providing a smaller particle size distribution. Fig 6.11 shows the temporal signal response of ^{65}Cu (*a*,*c*) and ^{66}Zn (*b*,*d*) from the brass sample at two different delay times (2 μs and 1 s) between laser pulses. Two characteristics of the ICP-MS temporal signal show the effects of the second pulse at a delay time of 2 μs compared to the 1 second time delay, increased intensity and fewer spikes. Similar to previous work reported by Liu et al [9], the ^{66}Zn signal had fewer spikes than ^{65}Cu. The improvement in analytical performance can be quantified by calculating the temporal relative standard deviation (TRSD), the short term change in the temporal signal, according to the equations mentioned (6.1) to (6.4) based on a five data point average. The data obtained for ^{65}Cu using the above formulas are shown in Fig 6.12. The error bars represent the reproducibility between three experiments (external precision; RSD). The TRSD and RSD are optimum for microsecond delay times, which corresponds to the minimum number of spikes on the temporal signal. The TRSD was improved from approximately 4% to less than 2%; RSD was improved from approximately 20% to 4%.

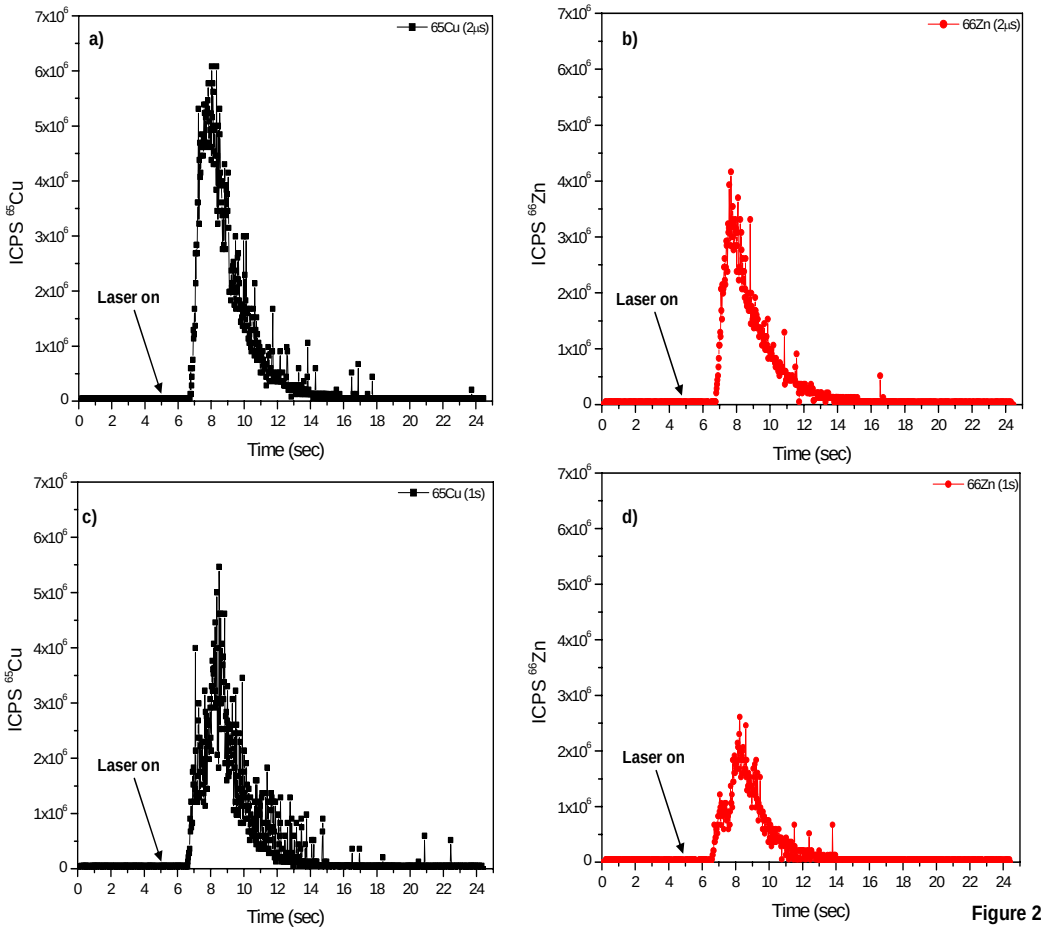

Figure 6.11 Temporal signal intensity of ^{65}Cu (*a*,*c*) and ^{66}Zn (*b*,*d*) from the brass sample with a second laser pulse at 2μsec and 1sec delay times.

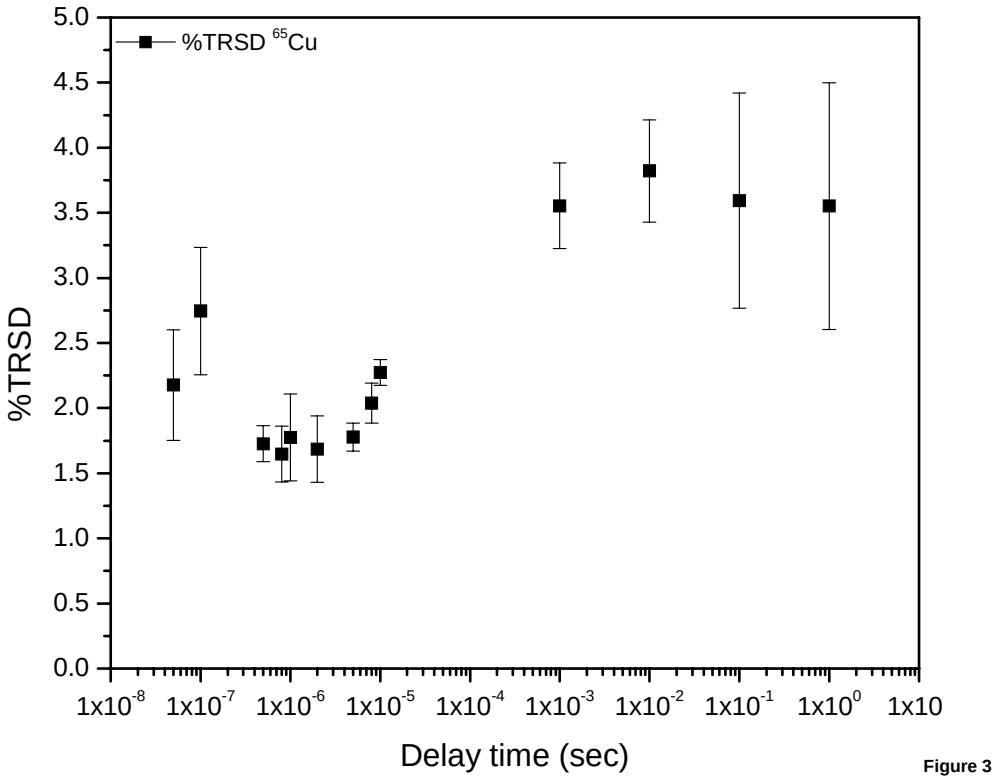

Figure 6.12 Temporal relative standard deviation for ^{65}Cu versus delay time between laser pulses

The ICP-MS integrated response for ^{65}Cu versus delay time between dual laser pulses shows an increase in the total signal intensity was measured for delay times between 100 ns - 5μs compared to a 1 second delay time. The use of a 1 second delay time represents the case when two separate pulses are used for ablation; the interaction between the second pulse and the mass ablated by the first pulse is negligible at 1 second delay. The signal enhancement for the delay between 100 ns to 5μs was between 1.5 - 2.0 times greater than the 1 second delay time. Crater volume measurements were performed to determine if the increase in the signal intensity was due to an increase in the ablated mass. The crater volume increased by 20% using microsecond delays, which can not account for the increase

in signal intensity of 50-100%. The improvement in the signal intensity and the decreased appearance of spikes in the temporal signal is believed to be due to the breaking up of particles by the second laser pulse.

Shadowgraph images after single and double pulse measurements are shown in Fig 6.13. Fig 6.13 (a) shows the ablated mass to be ejected from the sample in a conical shape 400 nanoseconds after the first laser pulse, Fig 6.13 (b) shows an image 50 nanoseconds after the second pulse (total time after the first pulse 450 nanoseconds). Fig 6.13 (c) shows an image 396 nanoseconds after the second pulse (total time after the first pulse 796 nanoseconds). Comparison of 6.13 (a) and (b) shows that the aerosol is made up of a denser cloud of smaller particles after interacting with the second laser pulse. The ability to break up large particles will be related to the efficiency of coupling the second laser pulse energy to the ablated aerosol. Because all ablated particles are not ejected simultaneously nor perpendicular to the sample surface, even at the optimum delay in this work, the interaction between the second pulse with the ablated mass is still believed to be minimal. More effective break-up of ablated particles may be achieved by optimizing the second pulse parameters such as pulse width (to obtain longer interaction with the ablated mass), spot size (i.e. larger spot size allows interaction with particles that are ejected at larger cone angles); laser energy, etc. These parameters were not adjusted with the laser used in this work.

Double pulse laser ablation sampling with ICP-MS was used to improve the internal (temporal stability) and external precision of analysis. This initial study

demonstrated the ability of a second laser pulse to produce a finer aerosol by interacting with an ablated mass plume. An enhancement in ICP-MS intensity and precision did not originate from the additional ablated mass, but from the break up particles of the original aerosol. A significant improvement of five times was achieved in the %RSD with a nominal factor of two improvements in %TRSD. The improvement in intensity and precision warrants further work to optimize the second pulse parameters, such as pulse width, energy, spot size and beam overlap.

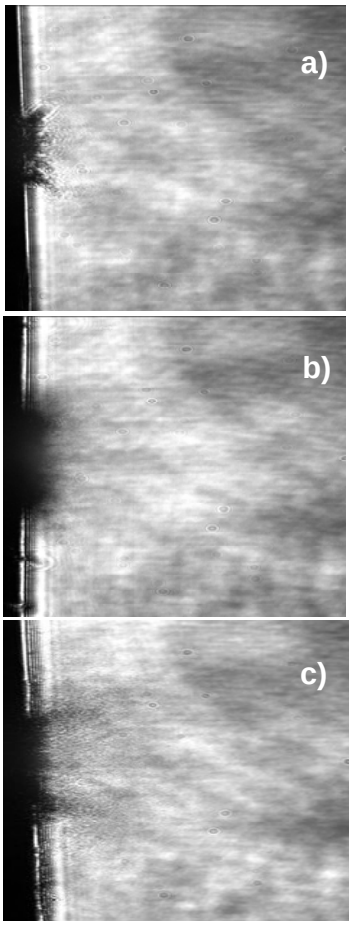

a) 400 ns after first pulse.

b) 50 ns after the second pulse (450 ns after the first pulse)

c) 396 ns after the s

Figure 6.13 **a)** Mass ablated from the sample 400 ns after the first pulse. **b)** Image of mass 50ns after the second pulse (total time 450 ns). **c)** Image taking 396 ns after the second pulse (total time 796 ns)

References

1. W. T. Chan and R. E. Russo, Spectrochim. Acta Pt. B-At. Spec. 46B, 1471-1486 (1991)

2. H. R. Kuhn and D. Gunther, Analytical Chemistry 75, 747-753 (2003)

3. R. Jaworski, E. Hoffmann, and H. Stephanowitz, International Journal of Mass Spectrometry 219, 373-379 (2002)

4. V. Margetic, A. Pakulev, A. Stockhaus, M. Bolshov, K. Niemax, and R. Hergenroder, Spectrochimica Acta Part B-Atomic Spectroscopy 55, 1771-1785 (2000)

5. X. L. Mao, A. C. Ciocan, and R. E. Russo, Applied Spectroscopy 52, 913-918 (1998)

6. M. Gagean and J. M. Mermet, Spectrochim. Acta Pt. B-At. Spec. V53, 581-591 (1998)

7. D. Aeschliman and D. Baldwin, Private communication (2003)

8. M. Guillong, Kuhn H-R, and D. Gunther, Spectrochim. Acta Pt. B-At. Spec. 58, 211-220 (2003)

9. H. C. Liu, X. L. Mao, and R. E. Russo, J. Anal. Atom. Spectrom. 16, 1115-1120 (2001)

Chapter Seven

Conclusions and recommendations for future study

7.1 Particles in laser ablation

7.1.1 Control of particle size from pure element material

Laser parameters and ambient environment affect the size of particles generated during laser ablation processes. While the size of the particles can also be different in ablation of multi-element material, control of the particle size is easier to achieve for pure element material. In chapter 3, the influence of several parameters was examined with respect to particle generation in laser ablation. Particle size measurement methods were also reviewed. It is demonstrated that the magnitude of the laser energy is important in particle size. At low energy, vaporization is dominant and most particles are condensed nano particles. As energy increases, more particles are obtained from the molten layer with size as large as several micrometers. Small particles are preferred in PLD applications but larger spherical particles are also desired in other applications. The width of the pulse influences the thermal transport in the material. A shorter pulse width has a smaller thermally affected area and less melt ejection, the mass removal is mostly in the form of vapor. Laser scanning speed and gas flowrate also affect the particle size.

Among other parameters not discussed, gas ambient is often mentioned to have a strong influence on particle generation and size. Ablation performed in fast expanding gas like helium generating lower density and favor small particles.

Ablation in heavy, slow expanding gas like argon confined the vapor plume in a smaller region, the high-density plume results in higher collision probabilities and thus larger particles. Also high pressure confined in the smaller vapor plume cause more molten material to be removed as larger droplets.

7.1.2 Generation of liquid droplet from molten pool

The generation of liquid droplets is usually observed at higher laser fluence. While the ejection of molten material can lead to a higher ablation rate than from a pure vaporization process, it is not desired for applications like pulsed laser deposition and chemical analysis. It is therefore important to understand the formation mechanisms for the droplets to either enhance or suppress their formation depending on the application. The idea of a higher-pressure plume above the laser spot (recoil pressure) has been attributed as the cause of molten material ejection. In Chapter 4 it is found that the ejection of particles is related to the internal shockwave, which travels back and strike the surface. Particles are ejected from the surface soon after the internal shockwave strike the surface. The internal shockwave pushes molten liquid out of the surface around the crater. The internal shockwave can be predicted by ongoing simulation studies and preliminary results provide satisfactory agreement with the experimental data.

Different sample properties strongly influence the ejection behavior of the particles. As shown in most studies, metal ejects around the crater and forms a hollow conical shape. However, for silicon the particles form a jet emerging from the center which sustains for 1~2 microseconds before the jet stops and breaks up. The

nature of this different behavior is presented also in chapter 4 and is related to the density variation during solid-liquid transition and also to the melting layer thickness. In silicon ejection, the aftermath of the multiple internal shockwaves can be observed by the breaking up of small particles from the main jet.

7.1.3 Particle chemistry and size dependency in multi-element material

Despite the advantages of laser ablation over traditional chemical sampling methods, fractionation still remains the biggest challenge before laser ablation reaches its full potential. In Chapter 5, the change of particle chemistry with respect to particle size was demonstrated. The proposed model explains the variation of the particle size and its chemical composition by considering a layer of vapor condensate material to be deposited on the ejected droplet core. The smaller particles were primarily zinc (low melting point element) and larger particles were primarily copper (high melting point material). Often during the experiments, the largest or smallest particles are absent due to lower transport efficiency. With this in mind, it is recognized that only a faction of particles cannot accurately determine the chemistry of a sample because the particle chemistry varies with the particle size. Besides causing the fractionation, larger particles from laser ablation create big signal spikes during the spectroscopy experiments, which cause errors in precision. Three approaches were discussed in Chapter 6 that are dedicated to solving these problems and each procedure provides distinct improvement. For chemical analysis using methods like the ICP-MS, smaller particles are desired to eliminate errors from sudden signal jump; however those small particles need to be

representative of the original material. Combination of the methods discussed in chapter 6 may yield satisfactory results and is recommended for future *respond*.

7.2 Future study

7.2.1 Theoretical modeling and simulation

It is known that low pressure, short wavelength, and short pulse duration facilitates the generation of smaller size particles and the reverse is also true. There are multiple mechanisms involved in the generation of the particles and other than empirical results obtained for common samples, there are no reliable methods to predict the size of particles generated in laser ablation for materials, which is not studied. Particles can be produced from vapor condensation, liquid ejection, and solid exfoliation. After a particle is produced, it may interact with other particles or even fractured by strong shockwaves. A systematic and thorough study, though formidable, is necessary to understand and ultimately to predict the products of laser ablation. Theoretical modeling and simulation including the laser pulse, shockwave, plume propagation, heat transfer in the solid material, etc. would be a very useful study. Simulation work to predict the occurrence of the external shockwave, vapor plume and internal shockwave is being performed by Wen and achieved successful albeit preliminary results that agree with the experimental results discussed in this dissertation. Further work is needed to understand the processes occurring in laser ablation.

7.2.2 Liquid droplet production

Generation of liquid droplets is usually associated with the formation of a raised crater rim and is undesirable for micromachining applications. And as discussed in Chapter 6, larger droplets degrade the performance of chemical detection apparatus. On the other hand, the generation of droplets significantly enhances the ablation efficiency and is useful when large removal volume is desired. Finding the controlling parameters (threshold energy, pulse width and etc) of droplet formation enables the removal of material mostly in vapor form and thereby induces a clean crater profile without the unwanted crater rim and large particles. In Chapter 6, we refer to the use of two UV laser beams to generate smaller particles from droplets that were originally larger. In an on going work, not discussed in the dissertation, one UV and one IR laser beams were applied with different delay times to generate craters up to 6 times the original removal volume (removed volume of silicon increased from ~60000 μm^3 to ~360000 μm^3 in a single laser pulse). This was achieved by increasing the molten layer depth and which represents greater liquid droplet ejection. Both eliminating and enhancing the liquid droplet removal have their own preferred applications and should be further studied.

7.2.3 Nanometer size material fabrication

It has been shown that nanometer sized features can be fabricated using laser ablation. In the SEM images of Chapter 4, a nano filament was demonstrated using femtosecond laser pulses. Also in Chapter 3, changing laser parameters was shown to be able to control the particle sizes. As applications of nanomaterials are

continue to proceed, it is of great interest that works involving nano material generation during laser ablation to be extended.

7.2.4 Nano alloy

Extending the concepts of Chapter 5, which illustrate the variation of particle size with respect to particle chemistry, it is possible to fabricate very small particles with desired chemical composition, e.g. nano alloy. Material properties can be further manipulated with desired characteristics under specific operating conditions. Currently work is being performed to extract particles of only a certain size (within an upper and lower size range) from the laser ablation aerosol to produce nano materials with a particular chemical composition. Preliminary results showed that particle chemistry varied with particle size, which is already demonstrated in Chapter 5. However, this technique provides the ability to generate particles with only the desired composition instead of having a chemical distribution, which occurs in most ablation techniques. This work is currently being studied.

7.2.5 Solid exfoliation: thermal stress

For brittle materials like glass or silicon, large chunks of material may erupt from the surface not only in the liquid form but also directly from solid fractures. This can be observed at later times in the laser ablation process (e.g. 5 microseconds after the laser pulse in silicon). Although liquid ejection is currently emphasized, it is the solid ejection that is little understood. Solid exfoliation is caused by the thermal stress generated inside the material; once the stress surpasses the mechanical strength of the material, a large fracture may break from the bulk

material. This type of material removal is undesired in almost all applications. How to predict and further reduce the occurrence of this phenomenon is needed especially when ablating brittle materials.